

UNIVERSITÀ DEGLI STUDI DI NAPOLI
FEDERICO II

DOTTORATO DI RICERCA IN FISICA

Ciclo XXXIII

Coordinatore: Prof. Salvatore Capozziello

**The connection between star-formation
and supermassive Black Hole
accretion in the local Universe**

Settore Scientifico Disciplinare FIS/05

Dottorando:

Olena Torbaniuk

Tutori:

Prof. Maurizio Paolillo

Prof. Giuseppe Longo

Anni 2018/2021

Acknowledgements

“We are an impossibility in an impossible universe.”

— Ray Bradbury

The following few words I want to devote to the important people, without whom this work would be impossible, and I would not be the person I am now.

First of all, I want to express my deepest gratitude to my PhD supervisors, *Prof. Maurizio Paolillo* and *Prof. Giuseppe Longo* for guiding me during these three years, for their valuable support and enthusiastic encouragement throughout my study.

Maurizio, I have been extremely lucky to have a supervisor who cared so much about my work. I am wholeheartedly grateful for your extensive knowledge, perceptiveness and enthusiasm, which allowed me to enjoy my work so much. I appreciate very much all your patience, understanding, support and valuable advice in different work and life issues. Our numerous discussions and debates on various scientific topics will always remain in my mind. Your positive outlook and confidence in my research always inspired me and gave me the strength and courage to complete this thesis. Special thanks for your amazing (and sometimes crazy) ideas, your special sense of humor and, of course, for the huge amount of coffee you shared with me.

Giuseppe, I am deeply grateful to you for giving me the opportunity to work with you and many other great scientists here in Naples. Thank you for your valuable support and helpful advice, and most of all for always respecting my

own opinions and decisions, and for allowing me to grow as an independent and confident researcher.

I would also like to thank the reviewers of my PhD thesis, *Prof. Antonis Georgakakis* from the National Observatory of Athens and *Prof. Angela Bongiorno* from the INAF–Astronomical Observatory of Rome, for their insightful comments and invaluable suggestions that allowed me to improve my work.

I am also grateful to all members of the astrophysics group of the Department of Physics for their assistance and helpful contributions to my research. I enjoyed working with such fascinating scientists who have helped me feel part of their Italian family. Special warm words for my colleagues *Oleksandra Razim* and *Demetra De Cicco* for their friendly attitude, support and many smiles.

I would like to offer my special thanks to the secretary *Mr. Guido Celentano* for his support and kind words during all years. Without his help, I would not have been able to handle all the necessary bureaucracy and documentation.

I would like to extend my sincere thanks to my very first supervisor *Dr. Ganna Ivashchenko*, who introduced me to the field of extragalactic astronomy and cosmology, and contributed to my development as a scientist at the beginning of my career. I am grateful to you for remaining my close and sincere friend even after my graduation from the University.

A very special word of thanks goes for my best friend, *Dr. Olena Shubina*. No matter how far apart we are now, I always feel your support and understanding. I will always remember our laughter, crazy trips and long-lasting and warm conversations on various topic. I am really obliged to you.

And finally, I would like to thank the most important person in my life, my *Mom*, for her unconditional love and unwavering belief in me. Words cannot describe my thankfulness for her constant support and help. I owe her a lot today.

Olena Torbaniuk

May 2021

Naples

Contents

List of Figures	vii
List of Tables	viii
Introduction	ix
The co-evolution of Active Galactic Nuclei and their host galaxies	2
1 Overview of Active Galactic Nuclei	2
1.1 AGN Taxonomy	2
1.2 AGN structure and the unified model	7
2 Galaxy properties and evolution	14
2.1 Galaxy classification	14
2.2 Elements of galaxy formation and evolution	17
3 AGN and host galaxy co-evolution	22
3.1 The evidence for co-evolution	22
3.2 The SFR-BHAR connection	26
3.3 AGN feeding processes	28

3.4	Accretion onto the supermassive Black Hole	32
3.5	AGN and stellar feedback	35
The host galaxies of AGN in the local Universe		39
4	The optical and X-ray galaxy samples	39
4.1	SDSS brief overview	39
4.2	galSpec SDSS galaxy samples	41
4.3	The galaxy distribution on the SFR- \mathcal{M}_* diagram	43
4.4	The XMM-Newton Space Telescope and its source catalogues . .	46
4.5	The crossmatch between SDSS galaxy sample and XMM-Newton catalogue	48
5	Multiwavelength identification of AGN	51
5.1	Optical selection: BPT-diagrams	51
5.2	X-ray AGN selection criteria	56
5.3	The combination of the optical and X-ray AGN selection criteria	61
6	The X-ray emission from host galaxies and low-luminosity AGN	63
6.1	The K-correction	64
6.2	Correction for star formation	64
6.3	AGN host galaxies in the local Universe	67
The Black Hole accretion rate in the local Universe		71
7	The specific Black Hole accretion rate	71
7.1	The sBHAR definition	72
7.2	The sBHAR distribution as a function of stellar mass	74
7.3	The sBHAR and L_X correlation with stellar mass and SFR	76
8	Sources of uncertainty in the BHAR determination	85
8.1	The reliability of SFR and \mathcal{M}_*	85

8.2	The relation between bulge, total stellar and supermassive BH masses	89
8.3	The extended X-ray sources and their effect on the sBHAR-SFR connection	93
8.4	AGN-dominated sources in the local Universe and their effect on the sBHAR distribution	94
9	Discussion	99
9.1	sBHAR distribution in the local Universe	99
9.2	The star-formation and Black Hole accretion connection	101
	The AGN and host galaxy co-evolution in the local Universe as probed by Chandra data	106
10	The X-ray galaxy properties from Chandra Source Catalogue	106
10.1	Chandra overview	106
10.2	The SDSS-CSC crossmatch	108
10.3	The identification of ‘classical’ AGN	111
11	The BHAR correlation with host galaxy properties	116
11.1	The BHAR distribution for <i>Chandra</i> data	116
11.2	The BHAR correlation with stellar mass and star-formation rate	118
	Conclusions	124
	Bibliography	126

List of Figures

1.1	Typical optical spectra of AGN	6
1.2	An active galactic nucleus structure (an artist's perspective) . . .	8
1.3	A schematic representation of an AGN SED	9
1.4	A schematic view of the unified model of Active Galactic Nuclei	12
2.1	Galaxy morphological classification proposed by Edwin Hubble	15
2.2	The galaxy bimodality	21
3.1	The correlation SMBH mass – galaxy bulge mass and stellar velocity dispersion for pseudobulges, classical bulges and ellipticals	23
3.2	The space density of AGNs as a function of redshift in different luminosity ranges. The stellar mass function for the sample of galaxies	24
3.3	The cosmic evolution of mean SFR and BHAR densities obtained by the cosmological hydrodynamic simulations	25
3.4	A schematic representation of the shape, redshift evolution and stellar mass dependence of the probability distribution of specific Black Hole accretion rates within galaxies of given redshift and stellar mass	28
3.5	The quest for SMBH feeding	31
3.6	A schematic representation of the main components of radiative and jet-mode AGN	33

3.7	Schematic diagrams to illustrate the two main modes of AGN feedback	36
4.1	The redshift distribution for our final SDSS galaxy samples . . .	44
4.2	The distribution of star-formation rate vs. stellar mass for our final SDSS galaxy sample	45
4.3	The distribution on the sky of all galaxies from our SDSS galaxy sample and the 3XMM footprint area	49
4.4	The distribution of star-formation rate vs. stellar mass for our SDSS galaxy sample and X-ray sources from 3XMM-DR8	50
5.1	The BPT-diagrams for the 3XMM-SDSS sample.	53
5.2	The distribution of star-formation rate vs. stellar mass for X-ray sample in hard band	55
5.3	The X-ray luminosity vs. redshift for the objects in X-ray sample	58
5.4	The X-ray flux in hard band vs. optical SDSS r -band and i -band magnitude and the X-ray flux in hard band vs. 2MASS infrared K_S -band magnitude for sources in our X-ray sample	59
5.5	The distribution of star-formation rate vs. stellar mass for AGN selected by the X-ray criteria	60
5.6	The BPT-diagrams for the AGN selected by X-ray criteria	62
6.1	The X-ray luminosity vs redshift distribution of the 1628 objects from our 3XMM sample	66
7.1	The cumulative histogram of flux upper-limit in hard band for XMM cameras from XMM FLIX service	75
7.2	The distribution of the specific Black Hole accretion rate for AGN in <i>star-forming galaxies</i>	77
7.3	The distribution of the specific Black Hole accretion rate for AGN in <i>quiescent galaxies</i>	77
7.4	The distribution of X-ray luminosity and the specific BH accretion rate on SFR- M_* plane	79

7.5	The number of points in each SFR and \mathcal{M}_* bin for both diagram presented in Figure 7.4	80
7.6	The jackknife mean value of sBHAR vs SFR for star-forming and quiescent galaxies for six stellar masses ranges	81
7.7	The least-square linear best-fit of sBHAR vs SFR correlation with 95% confidence interval in six stellar masses ranges for 3XMM sample	82
7.8	The normalised SFR as a function of the mean L_X obtained by the jackknife resampling for SFGs in 3XMM AGN sample	84
8.1	The comparison of SFR for our 3XMM AGN sample calculated by Brinchmann et al. (2004) and SFR corrected according to the criteria proposed by Oemler et al. (2017)	87
8.2	The comparison of stellar mass for our 3XMM AGN sample calculated by Brinchmann et al. (2004) vs. the stellar mass computed by Mendel et al. (2014)	88
8.3	The distribution of star-formation rate vs. stellar mass from Mendel catalogue for 1362 X-ray objects	89
8.4	The BH-to-stellar mass diagram for star-forming and quiescent galaxies in our 3XMM AGN sample	92
8.5	The distribution of star-formation rate vs. stellar mass for extended X-ray sources	95
8.6	The distribution of the specific BH accretion rate for the combined sample of extended and non-extended X-ray sources	95
8.7	The X-ray luminosity vs. redshift for the quasars and AGN from our X-ray sample	97
8.8	The sBHAR distribution for SDSS quasars and AGN studied in this work	97
10.1	An example of spiral galaxy J130056.06+274727.0 from our SDSS galaxy sample with its X-ray images obtained by <i>XMM-Newton</i> and <i>Chandra</i> space telescopes	107

10.2	The sky distribution of all galaxies from our SDSS galaxy sample and <i>Chandra</i> footprint area	109
10.3	The distribution of star-formation rate vs. stellar mass for our SDSS galaxy sample and X-ray sources from CSC 2.0	110
10.4	The X-ray luminosity vs. redshift for the objects in <i>Chandra</i> X-ray sample	112
10.5	The X-ray flux in hard band vs. optical SDSS <i>r</i> -band and <i>i</i> -band magnitude and the X-ray flux in hard band vs. 2MASS infrared K_S -band magnitude for sources in <i>Chandra</i> X-ray sample	113
10.6	The distribution of star-formation rate vs. stellar mass for the <i>Chandra</i> AGN selected by the X-ray criteria	114
10.7	The X-ray luminosity vs redshift distribution of the 750 objects from our <i>Chandra</i> sample	115
11.1	The distribution of the specific Black Hole accretion rate for AGN in <i>star-forming</i> and <i>quiescent galaxies</i>	117
11.2	The distribution of sBHAR for ‘classical’ and low-luminosity AGN from 3XMM and CSC samples	118
11.3	The distribution of X-ray luminosity and the specific BH accretion rate on SFR– M_* plane for <i>Chandra</i> AGN sample	120
11.4	Number of points in each SFR and M_* bin for both diagrams presented in Figure 11.3	121
11.5	The jackknife mean value of sBHAR vs SFR for star-forming and quiescent galaxies for six stellar masses ranges	122
11.6	The least-square linear best-fit of sBHAR vs SFR correlation with 95% confidence interval in six stellar masses ranges for 3XMM and CSC samples	123

List of Tables

4.1	The number of sources obtained by the crossmatch of our SDSS galaxy sample and 3XMM-DR8 catalogue at each step of data reduction	50
5.1	The number of galaxies classified as star-forming, composite and AGN according to the BPT diagrams	56
5.2	The number of AGN selected by different X-ray criteria	60
5.3	The number of X-ray selected AGN classified as star-forming, composite and AGN according to the BPT diagrams	62
6.1	Composition of the 3XMM-SDSS X-ray sample	69
7.1	The best-fit parameters obtained from a linear relation between $\langle \log \lambda_{\text{sBHAR}} \rangle$ and $\log \text{SFR}$ for six stellar mass range for the 3XMM-SDSS sample	84
11.1	The best-fit parameters obtained from a linear relation between $\langle \log \lambda_{\text{sBHAR}} \rangle$ and $\log \text{SFR}$ for six stellar mass range for the CSC-SDSS sample	121

Introduction

An important problem in extragalactic astronomy concerns the influence of the presence of Active Galactic Nuclei (AGN) on large-scale processes in the host galaxy and the correlation between the evolution of the host galaxy and the supermassive black hole (SMBH) in its centre. A connection between the SMBH and the galaxy growth has been suggested by a number of studies, based on empirical correlations between BH mass and integrated galaxy properties such as galaxy bulge mass, total stellar mass, central velocity dispersion and the rate of star formation (SFR). The current studies show that the SFR and the AGN accretion rate appear to follow similar patterns with cosmic time (i.e. redshift), indicating that the evolution of galaxies and their central SMBH proceeds in a coherent way.

At the same time, most previous studies have focused on investigating the AGN-host galaxy connection at intermediate/high redshift from $z \sim 0.25$ up to $z \approx 4.0$, while in the local Universe our knowledge is limited by the absence of wide-area surveys, especially in the X-ray band. However, studies of the local BHAR–SFR relation are valuable as local galaxies predominantly contain low-to-moderate luminosity AGN (i.e. with low-efficient SMBH accretion) which are difficult to trace at high redshifts. Additionally, the quiescent galaxy population in the local Universe allows us to study in detail the possible mechanism of star-formation suppression and explore the alternative AGN fuelling processes in environments with the small cold-gas reservoir.

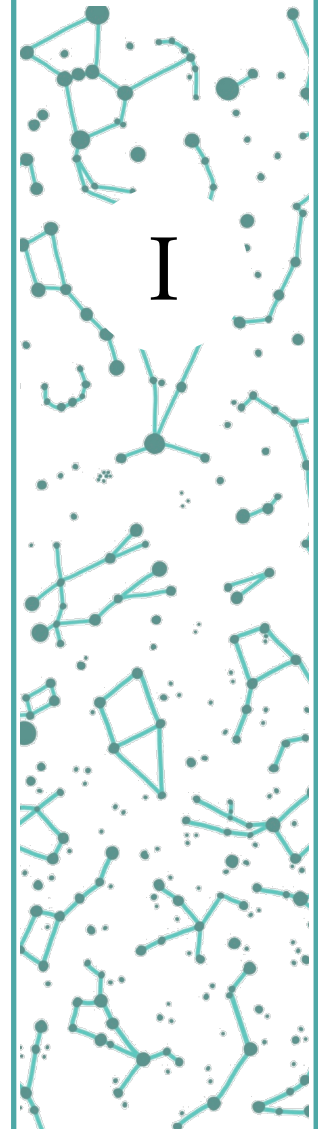
In this thesis we present a study of the correlation between star-formation

and AGN activity in the local Universe using a homogeneous Sloan Digital Sky Survey (SDSS-DR8) optical galaxy sample with robust SFR (in the range 10^{-3} to $10^2 \mathcal{M}_{\odot} \text{ year}^{-1}$) and \mathcal{M}_{\star} estimates (from 10^6 to $10^{12} \mathcal{M}_{\odot}$), in combination with X-ray data from the XMM-Newton Serendipitous Source Catalogue (3XMM-DR8) and the Chandra Source Catalogue (CSC 2.0), in order to identify AGNs and estimate their accretion rate.

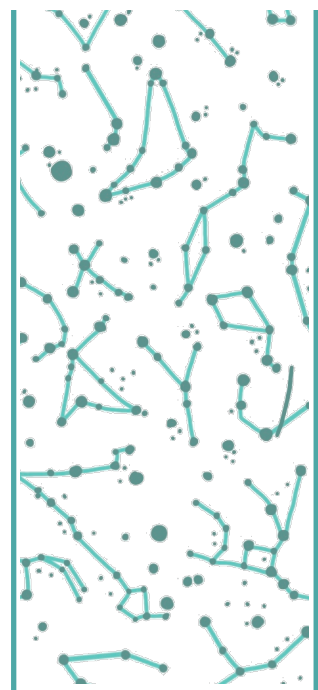
The first part of this work contains an overview of our present understanding of AGN and galaxy populations, their formation and co-evolution. The second part is dedicated to the study of AGN populations in the local Universe, their properties and those of their host galaxies. After the description of the optical galaxy catalogue and their X-ray counterparts, we describe the AGN identification process, the approach used to estimate the intrinsic X-ray AGNs luminosity and the corrections needed to account for the contribution of the host galaxy.

The third part presents our measurement of the specific BH accretion rate (sBHAR) and its correlation with the different galaxy properties such as the stellar mass, the SFR and the galaxy type (star-forming or quiescent galaxies). The intrinsic sBHAR distribution in the local Universe was obtained as a function of stellar mass and galaxy properties taking into account the variable XMM-Newton sensitivity across the sky. In addition, we studied the correlation between SFR and BHAR in the local Universe and compared it with the literature results for high-redshift samples. A separate chapter is dedicated to the description and analysis of the various effects, which can affect the reliability of our results.

In the fourth part we performed the same analysis as in the previous part using the X-ray data from the *Chandra* Source Catalogue to confirm results obtained from XMM data.



The co-evolution of Active Galactic Nuclei and their host galaxies



Overview of Active Galactic Nuclei

1

An Active Galactic Nucleus (AGN) is a compact object/region at the center of a galaxy that has higher luminosity than the entire host galaxy over at least some portion of the electromagnetic spectrum and is characterised by non-thermal emission (i.e not produced by stars). Such non-stellar emission has been observed over a wide range of wavelengths (from radio up to X-ray and gamma-ray wavebands) and according to our current understanding of astronomical observations, it is a result of accretion of matter onto a Supermassive Black Hole (SMBH) at the center of the host galaxy.

1.1 AGN Taxonomy

Nowadays, the term 'AGN' is a common name used for a vast class of objects with similar properties which historically were labeled by different names due to their discovery in different wavelength bands, and therefore they are referred to specific feature of one physical class. Below we present a summary of the main AGN classes with their properties.

Seyfert galaxies are mostly spirals galaxies with active star-formation processes, whose nucleus is characterised by a high surface brightness and non-thermal emission with an excess in the UV band. UV/optical spectra of these

objects show the presence of strong high-ionisation and coronal emission¹ lines (both permitted and forbidden). Based on the width of these emission lines Seyfert galaxies are divided into two general classes: Seyfert 1 with broad permitted emission lines (H I, He I, He II etc) and narrow forbidden lines from high-ionised element (such as [O II], [O III], [N II], [S II]), while Seyfert 2 are characterised by the presence of just narrow permitted and forbidden emission lines (see Figure 1.1). Later, Seyfert types intermediate between type 1 and 2 were introduced, and they were labelled Seyfert 1.2, 1.4 etc. The physical origin of such spectral differences and the existence of intermediate subclasses can be explained by differences in the source orientation relative to the observer, as suggested by the current AGN unification paradigm (see more details in Section 1.2). In addition, Seyfert galaxies are typically radio-quiet AGN.

Quasi-stellar objects, ‘quasars’ or QSO are the brightest class of AGN firstly discovered as bright radio sources with point-like (star-like) optical counterparts without evidence of the presence of a host galaxy (hence the origin of their name). However, the optical/UV spectra of the first quasars (3C 273 and 3C 48) revealed the presence of unusual broad emission lines, which appear to be Hydrogen lines redshifted to longer wavelengths due to the expansion of the Universe. This discovery helped to expose the extragalactic nature of these objects and their large distances from us (e.g. 3C 273 has $z = 0.158$, which corresponds to a distance of 749 Mpc). Moreover, the spectra of quasar are generally similar to Seyfert ones, but characterised by broader emission lines and a power-law continuum without stellar spectral features (see Figure 1.1). Further observations also revealed the presence of weaker absorption lines in some quasar spectra (the so-called, broad absorption line quasars, BAL QSO), which can be produced by a strong wind/outflows generated by the powerful

¹The coronal lines are highly-ionised optical forbidden lines (e.g. [Fe VII] $\lambda 5721, 6087 \text{ \AA}$, [Fe X] $\lambda 6374 \text{ \AA}$, [Fe XI] $\lambda 7892 \text{ \AA}$ and [Fe XIV] $\lambda 5303 \text{ \AA}$), which were formed in gas with densities of $10^2 - 10^{8.5} \text{ cm}^{-3}$ and with electron temperatures $\sim 12\,000 - 150\,000 \text{ K}$. They were firstly discovered in the hot Solar corona (i.e. thus the origin of their name ‘coronal lines’)

nucleus. At the same time, numerous observations showed that only 10-15% of the quasars population has strong radio emission (radio-loud quasars) and is extremely variable sources (see also the discussion on FSRQ below).

Blazars are radio-loud AGN characterised by a broad emission range (from radio up to gamma-ray) which is often significantly polarised. Based on their spectral energy distribution (SED; see Figure 1.3) and spectral index in the radio band, blazars are divided into flat-spectrum radio-loud quasars (FSRQs) and BL Lac objects. Both FSRQs and BL Lac are characterised by a strong non-thermal broad band continuum. However, FSRQs as well as quasars have both broad and narrow lines, while BL Lac objects show a featureless continuum with no lines (see Figure 1.1). Also, FSRQs are usually referred to as optically violent variable quasar (OVV quasar) due to their strong and extremely fast variability (with timescales is \sim day). Such properties can be explained by their face-on orientation and the presence of a strong relativistically beamed jet along the line-of-sight (see detail in Section 1.2).

Radio galaxies are AGN characterised by both nuclear and extended radio emission. Their other properties are really heterogeneous and therefore radio galaxies are overlapping with almost all other AGN classes making their classification complicated and sometime confusing. Multiple radio frequency observations allow us to separate the radio galaxies in two groups of sources with *steep* ($\alpha \geq 0.5$) and *flat* ($\alpha < 0.5$) radio spectrum. Using the spectral properties, radio galaxies can instead be divided into low-excitation (LEGs) and high-excitation classes (HEGs) based on the presence or absence of emission lines in their optical spectra. For instance, LEGs show no strong narrow and broad emission lines and they are good candidates for AGN with radiatively inefficient accretion (see Section 3.4), while HEGs are characterised by emission-line spectra similar to Seyfert 2 galaxies. Also, there is a difference in the host galaxy characteristics: LEGs usually show the presence of absorption lines typical for the spectra of giant ellipticals, while HEGs seem to be hosted by bluer galax-

ies. Based on the optical spectra, all radio galaxies can be also divided into narrow-line (NLRG) and broad-line (BLRG) by analogy to the Seyfert galaxies (see Figure 1.1). [Fanaroff & Riley \(1974\)](#) proposed one more classification of radio galaxies according to the radio morphology, which is measured by the ratio of the separation between the two brightest spots on opposite sides of the host galaxy, and the overall size of the radio image. The radio galaxies with a ratio < 0.5 , called FR I, usually have lower luminosities with a bright center and a weakening toward the edges (core-brightened radio galaxies), while radio galaxies with a ratio > 0.5 , called FR II, are higher luminosity with bright radio lobes at the edges (edge-brightened). Later, this classification was extended by one more subclass FR 0 ([Baldi et al., 2016](#)), i.e. radio galaxies with similar core properties to FR I, but without extended radio emission (lobes or jets).

Low-ionisation nuclear emission-line region galaxies or LINERs are the weak/low-luminosity AGN, which characterised by low-ionised, narrow emission lines (typical $[\text{N II}]$, $[\text{S II}]$ and Balmer lines, see Figure 1.1). The nature of these narrow lines and the energy budget of LINERs are controversial issues since such spectra can be produced by various mechanisms not associated with SMBH accretion, e.g. cosmic ray heating, diffuse thermal plasma and/or extra ionisation from evolved post-asymptotic giant branch (AGB) stars ([Cid Fernandes et al. 2011](#), [Yan & Blanton 2012](#)). However the most powerful LINERs are most likely the low-luminosity/low-accretion rate extension of Seyfert galaxies ([Ho, 2008](#), [Netzer, 2015](#)), which can be also divided into LINER 1s (broad) and LINER 2s (narrow) based on the width of their emission lines. Numerous observations showed that nearly one third of galaxies in the local Universe are LINERs.

In general, all AGN can be classified only by their radio luminosity, emission features in optical spectra and radio emission. For instance, the comparison of the nuclear luminosity with the luminosity of the host galaxy allows us to divide AGN into three groups: quasars, whose nuclear luminosity ex-

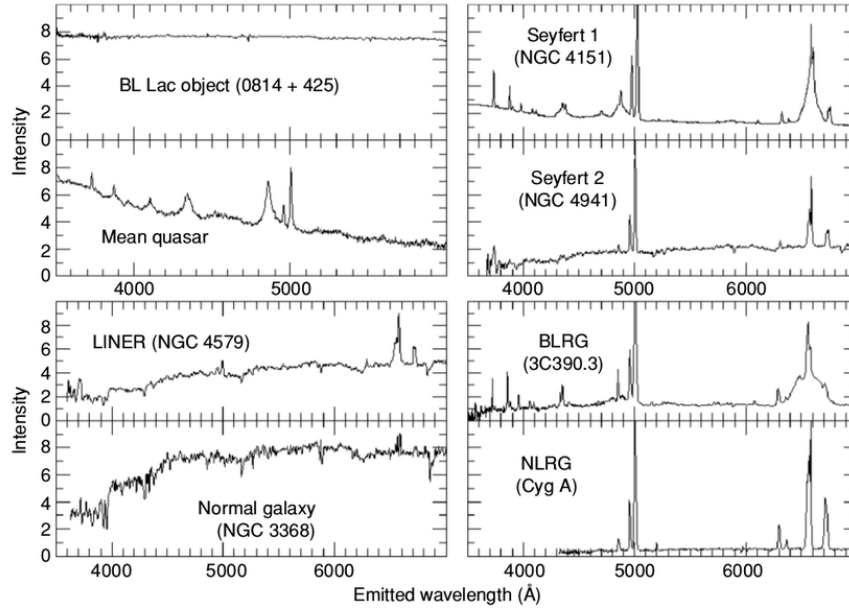


Figure 1.1: Typical optical spectra of AGN. For easy comparison all spectra were shifted to the rest-frame. Credit: <https://pages.astronomy.ua.edu/keel/agn/>

ceeds the galaxy luminosity by a few magnitudes (the typical luminosity is $L_{\text{bol}} \gtrsim 10^{46} \text{ erg s}^{-1}$), strong AGN with similar luminosity of the nucleus and the host galaxy ($L_{\text{bol}} \approx 10^{44} \text{ erg s}^{-1}$) and weak AGN, which nuclear luminosity is smaller than host galaxy ($L_{\text{bol}} \lesssim 10^{42} \text{ erg s}^{-1}$). Such difference in luminosity can be explained by the different SMBH mass and/or accretion rate for each class of AGN. One of the most used classification of AGN divides them into radio-loud (RL) and radio-quiet (RQ) AGN based on the radio emission, where RL are characterised by non-thermal emission associated with powerful relativistic jets, while RQ have dominant thermal emission from accretion disk and no sign of jets (Padovani et al., 2017). Moreover, we can classify AGN using the spectral index from the power-law radio spectrum, the radio morphology (FR I/FR II etc) or the width of the emission lines in the optical spectra (broad lines in quasar, Seyfert 1; narrow in Seyfert 2 and weak or no lines in Blazars).

Thus one object can be classified differently according to the different properties, because the source properties in some energy band highlight only some specific features and not reveal the entire nature of each source. As a result, AGN classification is not unequivocal and all AGN subclasses can overlap.

1.2 AGN structure and the unified model

The similar properties of the various AGN classes described in Section 1.1 (e.g. the presence of the broad emission lines in BLRGs, quasars and Seyfert, the blue continuum emission of quasars and Seyfert, the fast variability etc) prompted the astronomer to develop the model which can be capable to combine all these observational classes into a single type of physical object. Antonucci (1993), Urry & Padovani (1995) proposed a unified model which is based on the idea that the apparent differences between AGN classes can be explained by their different orientations with respect to the observer's line-of-sight. Moreover, some AGN properties at separate wavelengths can be explained by the presence/absence of a specific component in the AGN structure. The main AGN components are described below and shown in Figure 1.2 using as an example the typical radio-loud AGN (the relativistic jet is absent in the case of radio-quiet AGN).

The orientation-based unified model suggests that the main source of energy in AGN is due to the accretion of the matter onto the central supermassive Black Hole. The gas in such *accretion disk* loses its angular momentum through turbulence and viscosity friction converting the gravitational potential energy into radiation. A 'typical' AGN has an optically thick accretion disk (Shakura & Sunyaev, 1973), which emits from UV to optical wavelengths as a superposition of Black Bodies with decreasing temperatures as a function of distance from the central SMBH. The peak of emission is located in the far-ultraviolet (FUV; 1200 Å) and is referred as the Big Blue Bump (see blue line in Figure 1.3). A more detail description of optically thick accretion disk model is presented in Section 3.4 together with an alternative model for accretion disks of low-luminosity AGN.

Almost all AGN show the presence of strong nuclear X-ray emission, which is believed to be produced by a *hot corona* located is close to the SMBH. The hot

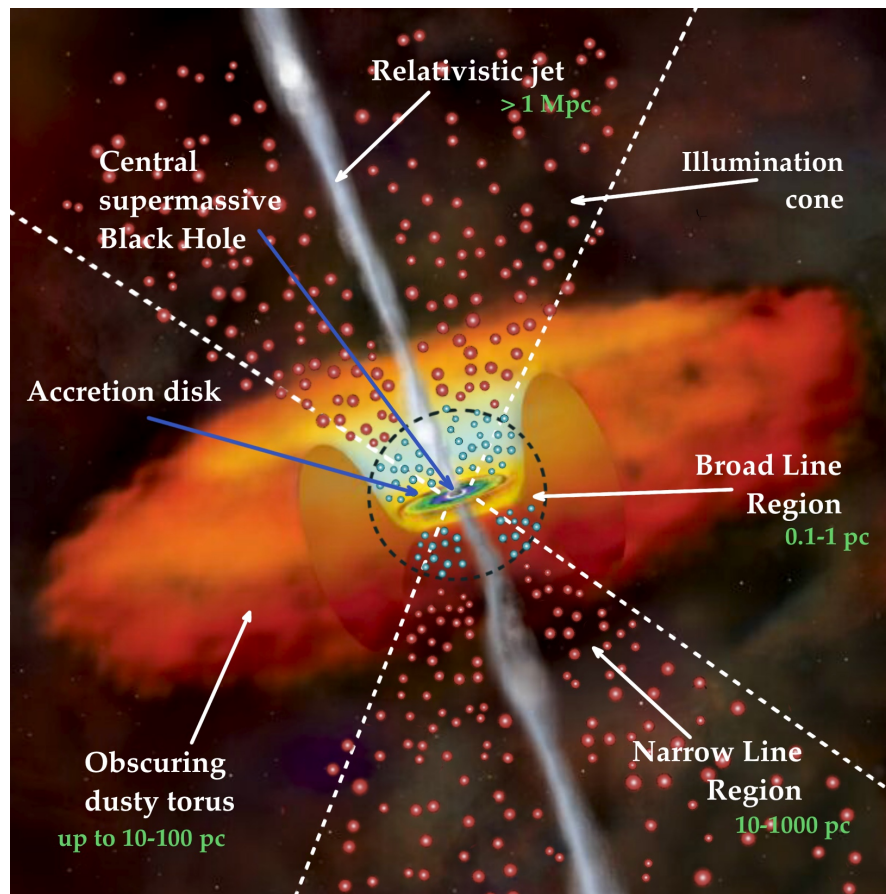


Figure 1.2: An active galactic nucleus structure (an artist's perspective). Credit: NASA/CXC/M.Weiss (adapted)

corona scatters the UV/optical photons up to X-ray energies through inverse Compton scattering and creates the power-law continuum with an exponential cut-off at higher energies (see Figure 1.3). In addition to the primary X-ray emission, there is an additional X-ray component reflected by the torus, BLR (they are discussed below) and/or disk, which produce a Compton hump with the peak at ~ 30 keV and fluorescent iron line Fe $K\alpha$ line at 6.4–6.7 keV. A large fraction of AGN also show an excess of X-ray emission below ~ 2 keV, which has an unclear origin and can be produced by a warm emitting gas in the accretion disk and the BLR; or be the extension of the far-UV accretion disk emission (hard tail of Big Blue Bump).

At a distance of 0.1–1 pc the SMBH is surrounded by a region consisting of large column density ($\sim 10^{23} \text{ cm}^{-2}$)/high-density ($n_e \gtrsim 10^9 \text{ cm}^{-3}$) gas clouds.

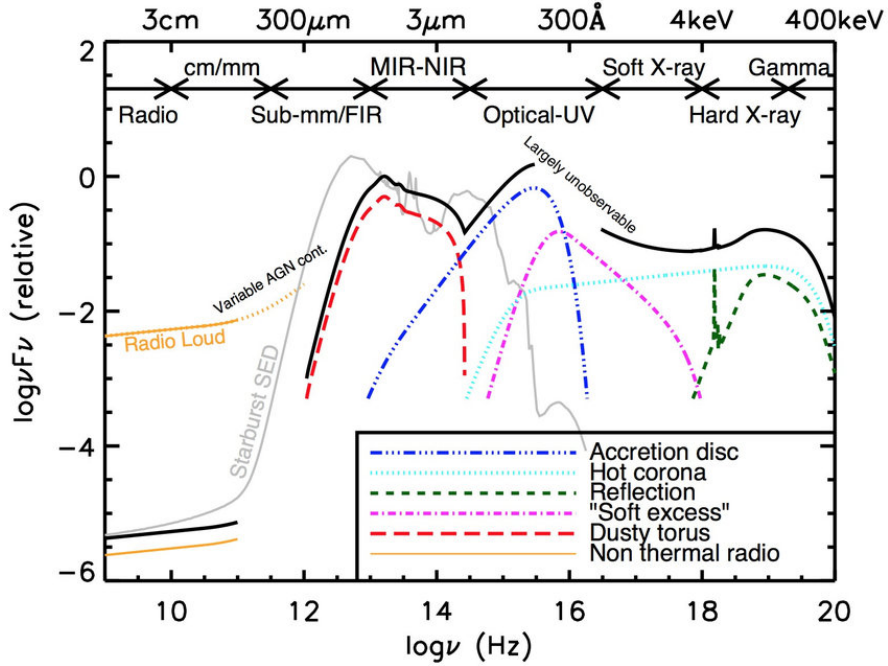


Figure 1.3: A schematic representation of an AGN SED, loosely based on the observed SEDs of radio-quiet quasars (Elvis et al., 1994, Richards et al., 2006). The black solid curve represents the total SED and the various coloured curves represent the individual components. Credit: Harrison C. M. PhD Thesis, 2014

For clouds with such large densities the gravitation force exerted by the SMBH dominates over the radiation pressure allowing the clouds to move around the SMBH on typical Keplerian orbits with velocities up to 10^4 km s^{-1} . This region was named *broad-line-region* (BLR) due to the fact that the UV photons from the accretion disk ionises the clouds (i.e. by photoionisation) and generate the broad highly-ionised permitted emission lines in the UV/optical range of AGN spectra (e.g. He II $\lambda 4686$, He III $\lambda 3869$, O IV] $\lambda 1402$, O VI $\lambda 1035$ with typical full width at half maximum, FWHM $\approx 10^3\text{--}10^4 \text{ km s}^{-1}$). At the same time, forbidden emission lines are suppressed by collisional de-excitation in the high density region.

Beyond the inner BLR we assume the presence of a region consisting of gas with smaller column density ($\sim 10^{20}\text{--}10^{21} \text{ cm}^{-2}$) and lower density $n_e \approx 10^3\text{--}10^6 \text{ cm}^{-3}$. The gas clouds in this region are located far from the central SMBH and probably reach distances up to $10^3\text{--}10^4 \text{ pc}$, and hence have lower velocities $\sim 100\text{--}2000 \text{ km s}^{-1}$ than those one in the BLR. This region was named *narrow-*

line region (NLR) by analogy with the BLR. However, the physical conditions in the NLR is slightly different from the BLR and lower densities allow to produce both permitted and forbidden narrow lines with higher ionisation levels (e.g. [O III] $\lambda 4959, 5007$, [O II] $\lambda 3727$). Moreover, the low-density NLR can contain a dust component due to its larger distance from the central energy source (i.e. the influence of nuclear radiation is weak and does not allow the dust sublimation).

The absorption lines in the BLR and NLR are usually weak in AGN due to the small covering factor, but some quasars possess blue-shifted broad absorption lines in the rest-frame UV spectrum the so-called BAL quasar (broad absorption lines quasar with strong resonance lines of C IV $\lambda 1549$, Si IV $\lambda 1397$, N V $\lambda 1240$, O VI $\lambda 1035$, and Ly α). According to the AGN feedback theory, these lines are produced by strong AGN outflows with velocities close to $\sim 10^4$ km s $^{-1}$ (see details in Section 3.5).

In Section 1.1 we see that the presence or absence of broad permitted emission lines in the optical spectra of AGN are used as a classification criterion to separate type 1 and type 2 AGN. The unified model states that BLR can be obscured partially or completely by the thick structure with a toroidal shape composed of molecular gas and dust; however the geometry of this ‘torus’ is still debated and it is widely believed to be clumpy (Elitzur & Shlosman, 2006, Hönig, 2019, Impellizzeri et al., 2019). The *dusty molecular torus* is located at scales ~ 1 –10 pc (for the most massive BH the outer region of torus can spread up to 100 pc) around the accretion disk and BLR, and has typical densities of about 10^4 – 10^7 cm $^{-3}$. The dust in the torus is heated by UV/optical emission from central engine, and therefore re-emits in the infrared waveband (IR) with a peak near $\lambda \approx 20$ – 50 μ m. The properties of this absorbing torus may explain the observed effect of complete or partial absence of optical/UV emission lines in the spectra of some AGN (i.e. the intrinsic emission of the BLR and the accretion disk are obscured by the dust in the torus). However, we will see in

Section 3.4 that several observations point to the complete absence of the BLR and torus in some low-luminosity AGN and LINERs (Ho, 2008).

In addition, the rotation of the SMBH in radio-loud AGN may generate collimated *jets* of relativistic particles, which are powered by the gravitational energy released by the accretion disk. This relativistic jets emit synchrotron radiation from radio to gamma wavelengths and expand over long distance up to 1 Mpc away from the central engine and outside the host galaxy itself. On the contrary, the radio emission in radio-quiet AGN is usually more compact, and probably caused by weak compact radio jets, supernovae etc.

As we saw above the orientation of the torus (and its geometry as a whole) plays a key role in the interpretation of the various classes of AGN and can successfully connect Seyfert type 1 and type 2, BLRG/NLRG etc. According to this orientation-dependent model if we observe the AGN in a direction perpendicular to the torus axis (i.e. zero inclination angle or edge-on view) the central accretion disk and BLR will be partially or completely obscured by the torus and few or no broad emission lines will appear in the spectra. An increase in the inclination between the torus axis and the line-of-sight leads to less torus obscuration and reveals more broad lines in the spectra (e.g. transition classes such as Seyfert 1.9, 1.8 and up to face-on Seyfert 1). The schematic representation of the unified model is shown in Figure 1.4, where the *bottom* part applied to the radio-quiet AGN (Seyfert 1 and 2) and the *top* part to the radio-loud AGN population characterised by powerful radio emission and jets. Beside the similar separation into subclasses by the presence of broad/narrow emission lines (BLRG/NLRG, quasars), radio-loud AGN contain one more group of objects, blazars, with weak or no emission lines in the spectra. As it was mentioned in Section 1.1 such appearance is caused by the fact that its relativistic jet is pointed along the line-of-sight and hence it is relativistically boosted, thus dominating over the emission of other AGN components.

Nowadays the observational evidence supports the orientation-dependent

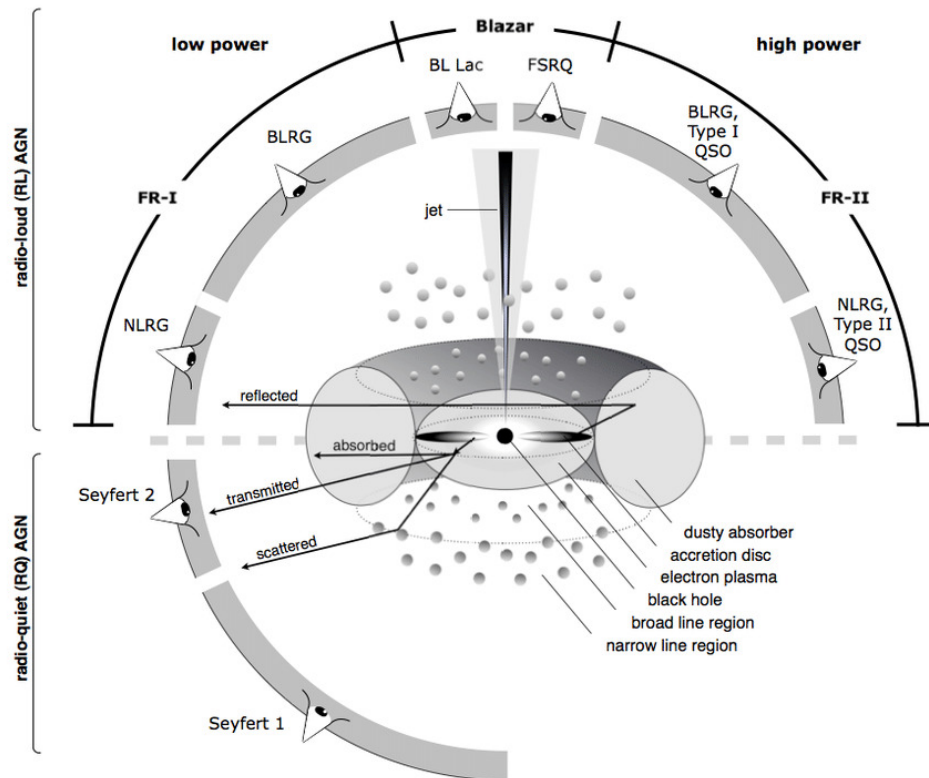


Figure 1.4: A schematic view of the unified model of Active Galactic Nuclei (AGN). Credit: [Beckmann & Shrader \(2012\)](#)

unified model and the presence of dusty-obscuring structure. First of all, the interferometric observations in the mid-IR and sub-mm bands revealed various dusty obscuring structures, which possess a cylindrical symmetry and different molecular and megamaser disk-like structures ([Tristram et al. 2014](#), [García-Burillo et al. 2016](#), [Impellizzeri et al. 2019](#)). At the same time, the spectropolarimetric analysis of some nearby Seyfert 2 galaxies revealed hidden broad emission lines in the polarised light, which are hidden from direct observation by some structure in the galaxy nucleus ([Antonucci & Miller 1985](#), [Capetti et al. 1996](#), [Alexander et al. 1999](#), [Marin & Schartmann 2017](#)). One more evidence of the obscuring torus existence is the detection of ionisation cones (i.e. bipolar outflows). These cones are produced by the photoionisation of the gas in the host galaxy by radiation from the central source and the BLR which escapes along the torus axis ([Wilson et al. 1993](#), [Durré & Mould 2018, 2019](#)).

Recent and more detailed observations of AGN showed that the unification model based only on orientation and obscuring material is incomplete and not able to explain all AGN properties (Tadhunter 2008, Netzer 2015). For instance, this model does not take into account the difference in luminosity and accretion rate (e.g. low-luminosity AGN like LINER are not included). In general, a change in accretion mode may indicate not only a difference in the properties of the central power engine, but also the fact that some AGN may not be able to sustain some their components (e.g. BLR or torus; see Section 3.4). The latest scenario is supported by the presence of ‘real’ type 2 AGN, which show no sign of hidden BLR in polarised light (Tran, 2003). Even the geometry of the obscuring structure requires major modifications, since an homogeneous dusty torus cannot explain some observation features such as the variability in obscuration observed in many type 2 AGN (Risaliti et al. 2005, Bianchi et al. 2009). In addition, hydrodynamical simulations showed that a reliable reconstruction of the AGN feeding mechanism requires the presence of turbulent motions, winds and star-formation processes, which are likely associated to a clumpy medium rather than a homogeneous torus structure (Elitzur & Shlosman, 2006, Hönig, 2019).

Additionally, an important role is played by the host galaxies and their evolution (see details in Section 3.1). The properties of observed AGN can simply vary with time and hence some subclass of AGN may represent a specific evolutionary stage of the entire AGN life cycle. This scenario is able to explain the large fraction of low-luminosity AGN and the almost complete absence of high-luminosity quasar in the local Universe (Ho, 2008, Kormendy & Ho, 2013). Furthermore, the basic unified model does not include the ability of AGN to change their luminosity and spectra (so-called changing-look AGN Frederick et al. 2019).

Galaxy properties and evolution 2

Studying of the co-evolution of AGN and their host galaxies requires the understanding of the formation of galaxies and their evolution through the cosmic time. It is believed that each galaxy contains a SMBH inside, which grew and evolved together with its host galaxy from the early Universe up to the present time. Such coherent evolution of SMBH and host galaxy requires that they can affect each other, e.g. the growth of SMBH can influence the gas in the host galaxy by strong radiation pressure and winds (AGN feedback), while the host galaxy can enhance or suppress the AGN activity regulating the amount of gas available for SMBH accretion by some internal (e.g. starburst) or external processes (e.g. galaxy merger and interaction).

2.1 Galaxy classification

In 1926 Edwin Hubble proposed the first galaxy classification ([Hubble, 1926](#)), which can divide all galaxies into four different classes based on their visual appearance: elliptical, lenticular, spiral and irregular galaxies (see Figure 2.1).

Spiral galaxies consist of a flattened disk, whose stellar population forms a spiral structure (usually two-armed). Some of spirals show the presence of a central concentration of stars known as the bulge, which shows the properties

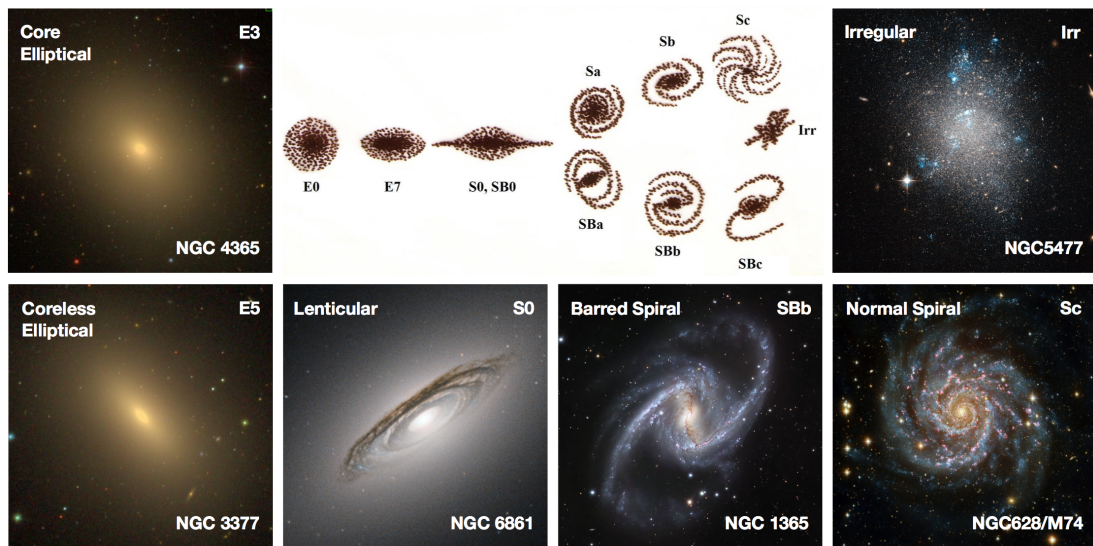


Figure 2.1: Galaxy morphological classification proposed by [Hubble \(1926\)](#) with example of galaxies of different galaxy classes. Credits: NGC 4365, NGC 3377, NGC 628/M74: SDSS DR14; NGC 6861, NGC 5477: ESA/Hubble & NASA; NGC 1365: ESO, IDA, R. Gendler, J-E. Ovaldsen, C. Thöne and C. Feron.

similar to elliptical galaxies (see discussion below). Roughly half of all spirals are also observed to have a bar-like structure, with the bar extending from the nucleus (or central bulge), while the arms begin at the ends of the bar. Spiral galaxies occupy two separate branches of the Hubble diagram, where the upper branch is devoted to the regular/normal spirals (S) with strong bulge, while the lower one spirals with weak bulges, but strong bar structures. Both classes are characterised by presence of spiral arms star formation and orderly circular motions in disk plane in contrast to the chaotic motion in elliptical galaxies.

Elliptical galaxies are characterised by relatively smooth light distribution with elliptical form generally without presence of any structural feature. As can be seen from Figure 2.1 the population of elliptical galaxies is separated into 8 subclasses according to galaxy ellipticity (from 0 to 7). The physical properties of elliptical galaxies reveals that they have redder color compared to other galaxy types due to the fact that they consist of older stellar populations and do not show the sign of active star-formation processes. Furthermore, elliptical galaxies can be divided into two classes based on their isophotes' shape. First, *core* ellipticals show *boxy* isophotes with lack of nucleus emission. These

ellipticals are also characterised by the presence of classical bulge, and strong X-ray and radio emission (from hot gas and sometimes the active nucleus). On the contrary, *coreless* ellipticals with *disky* isophotes often have a disk structure with extra light in the nuclear region generated from central starbursts (SBs) and do not show too much of X-ray hot gas. This difference in the shape and properties can be caused by different formation mechanisms (see Section 2.2).

Lenticular galaxies represent an intermediate class between elliptical and a spiral galaxies, which contains a large-scale disk, but do not show large-scale spiral arms. The disk of these galaxies used-up or lost most of its interstellar gas and therefore they have very little ongoing star-formation. On the contrary, lenticular galaxies can also show a significant amount of dust and mainly aging/old stars (like elliptical galaxies).

Irregular galaxies show little or complete absence of visual morphological features. In general, irregular galaxies are dwarf galaxies (about one tenth the mass of the Milky Way galaxy) and therefore their shapes can be explained by the deformation by an external gravitational force like interaction with larger galaxies. Irregular galaxies may contain abundant gas and dust and may possess distinct morphological features (weak disks, arms, lanes etc).

Several classes of galaxies are not included into the Hubble morphology classification, so we describe them here shortly:

- *ring galaxies*, have a ring-like structure of massive, young stars and small cores surrounded by interstellar medium without stars. Such ring galaxies are most likely formed when a smaller galaxy passes through the center of a larger spiral galaxy;
- *dwarf galaxies*, relatively small galaxies with typical diameter less than 10 kpc (ultra-compact dwarf galaxies are only 100 pc across) and usually they are satellites of larger galaxies. Dwarf galaxies may also be classified as elliptical, spiral, or irregular;

- *interacting galaxies*, the galaxies in the process of collision or merger. The gravitational fields of each galaxy severely disturb their shapes, the gas and dust interact forming bars, rings and other tail-like structures, sometimes triggering star formation;
- *starburst galaxies* are characterised by an exceptionally high star formation rate, where massive stars ionise the surrounding gas and create large H II regions. These galaxies are also sources of radio emission produced by supernova (SN) explosions. The majority of starburst galaxies are the results of the galaxy interaction (i.e. galaxy merger);
- *luminous* and *ultra-luminous infrared galaxies* (LIRG and ULIRG) are characterised by strong far infrared (FIR) thermal emission with typical luminosities $\gtrsim 10^{11}L_{\odot}$ (and $\gtrsim 10^{12}L_{\odot}$ for ULIRG). This emission is originated by the dust heated by young stars or an obscured AGN. Also they are referred to as *submillimeter galaxies* (SMGs), and are associated with galaxies evolved in the early Universe.

2.2 Elements of galaxy formation and evolution

The current paradigm of galaxy evolution suggests that all galaxies were formed as disk galaxies from small density inhomogeneities created after the Big Bang. According to the Λ CDM (Lambda Cold Dark Matter) model these small density structures grew into halos accumulating more and more mass due to clustering and merging (the ‘bottom-up’ model, [Peebles 1965](#)).

When the temperature of the gas inside DM halo decreased enough, the gas collapses toward the center conserving angular momentum. Then frictional forces drive the gas onto approximately circular orbits in a plane perpendicular to the angular momentum vector and forms a flat disk. The gas in this flat disk is denser and hence its cooling efficiency becomes higher allowing it to form the first stars. The thin stellar disk formed by the first stars

produces dynamical instabilities and perturbations of the gravitational field, which in turn produce perturbation in the circular stellar orbits (i.e. deviation from axi-symmetric gravitational potential) and formed the spiral arms and bar (so-called *pseudobulge* structure; Sanders & Huntley 1976, Romero-Gómez et al. 2007). However, hydrodynamical simulations showed that such scenario would produce the small and highly concentrated disk galaxies, where all available gas was rapidly used for star formation at high redshift, and therefore such disks would not be able to form stars in the local Universe. This problem can be solved by an additional source of gas heating and cooling, which allows to balance or delay the star-formation processes at high redshift (Robertson et al., 2006). This additional cooling/heating mechanism is provided by the supernova and AGN feedback (see Section 3.5).

The current scenario predicts the formation of spiral galaxies with pseudobulge. However, the observed Universe also contains other morphological types of galaxies like elliptical galaxies and spirals with a bulge component. The observed ellipticals and bulges (i.e. ‘mini’ versions of the ellipticals) have spherical shape with old stellar population (population II) and chaotic/random stellar motions, and hence their formation can not be explained through the formation of cold gas disks. Nowadays, there are two main models of elliptical galaxy formation. The first model suggests a monolithic collapse of the gas in a halo and its slow transformation into stars (Larson, 1975). In the end all gas will be converted into stars and the galaxy will not be able to create new populations of stars. However, this model has several problems. First of all, it requires really fast formation of the first stars before the beginning of the disk structure formation. And secondly, it can’t explain the complicated kinematic components (like small disk, dust lanes, shells, ripples etc), which are observed in some elliptical galaxies.

The second model of elliptical formation based on the the observations which revealed that ellipticals are located preferentially in dense environments

(galaxy groups and cluster, Dressler 1980). This points to the formation of ellipticals through interactions, mergers and secular galaxy transformations.

The merger theories predict that typical ellipticals are formed through *major* mergers (Cox et al., 2006). In this case, two disk galaxies with similar masses will be completely destroyed, their stellar populations attain a high velocity dispersion and form spheroidal structure (if a massive galaxy merges with a smaller galaxy with mass ratio less than 3:1, the smaller galaxy-satellite will be simply embedded into the large halo, a so-called *minor* merger). In addition, the morphology of resulting galaxy will depend on the dissipational properties of the gas, which can drive the gas toward the center of the merger remnant (with decrease of the rotational velocity and an higher velocity dispersion) and induce the formation of new stars; in some cases it can trigger extreme starburst (SB). Hence, such ‘wet’ mergers forms the ‘normal’ *coreless* elliptical galaxies, which are characterised by rapid rotation, central SB and small disk structures in some cases. An example of coreless ellipticals is shown in Figure 2.1 (NGC 3377). On contrary, the dissipationless or ‘dry’ merger of gas-poor progenitors form a spherical structure with a relatively slower rotation and the absence of SF processes (Naab et al., 2006). The most massive *core* ellipticals in the centre of galaxy clusters (central dominant ellipticals, cD) were formed exactly in this way though the collision of smaller ellipticals in dense environments (see NGC 4365 in Figure 2.1).

The merger process also plays important role in the formation of the bulge component inside disk galaxies. According to the galaxy formation paradigm, the bulge is a ‘mini’ version of an elliptical galaxy, which is formed through the collision of fairly low-mass progenitors in low density environments. This environment allows this ‘mini’ elliptical to survive for a long time without additional mergers and slowly transform its gas into stars. At some point, this galaxy with its DM halo starts to accrete additional matter from the environment, which begins to cool and form a disk similar to pseudobulge systems

(Baugh et al., 1996). The outcome will be a spiral galaxy with active SF in the disk and central spherical bulge with an old stellar population (i.e. a galaxy with ‘classical’ bulge). However, there are several alternative models which suggest the formation of the bulge structure through the rapid and violent evolution of disk instabilities (Genzel et al., 2008).

An observational evidence of the different galaxy formation mechanisms can be found in the galaxy distribution a color-color diagram (or other characteristic parameters as magnitude, stellar mass or star-formation rate; Strateva et al. 2001, Baldry et al. 2004). In this diagram galaxies are clustered in two main groups: the ‘blue’ sequence with spiral-disk S and SB galaxies (the so-called ‘main-sequence’ – MS – of star-forming galaxies) and the ‘red’ one made of ellipticals (E class) and intermediate S0 class (see Figure 2.2). Hence the natural explanation for such bimodality is that two galaxy population have different average color (or star-formation rate) and were formed by two different mechanism, i.e spiral (or *later-type*) galaxies were produced through gas accretion, while ellipticals (*early-type*) were mainly formed by the galaxy mergers (Cattaneo et al., 2006, 2009, Kormendy & Bender, 2012). Additionally, this formation scenario was confirmed by clustering studies, according to which early-type galaxies forming the red sequence are preferentially located in the dense galaxy clusters. The galaxy bimodality is observed up to $z \sim 1.5$ (Menci et al. 2005, Cameron & Driver 2009) and is characterised by a the strong evolution of the blue sequence with redshift (Faber et al. 2007, Noeske et al. 2007, Blanton & Moustakas 2009, Dekel et al. 2009, Aird et al. 2017), while the red sequence tends to disappear at high redshift (i.e. most massive core elliptical galaxies were formed closer to the present times thought the transformation of the spiral galaxies; Dekel et al. 2009).

In addition, the two galaxy populations have a nontrivial region of overlap, the so-called ‘green valley’. The galaxies in this area passively evolve after having their star-formation mechanism turned off. It may happen when the gas

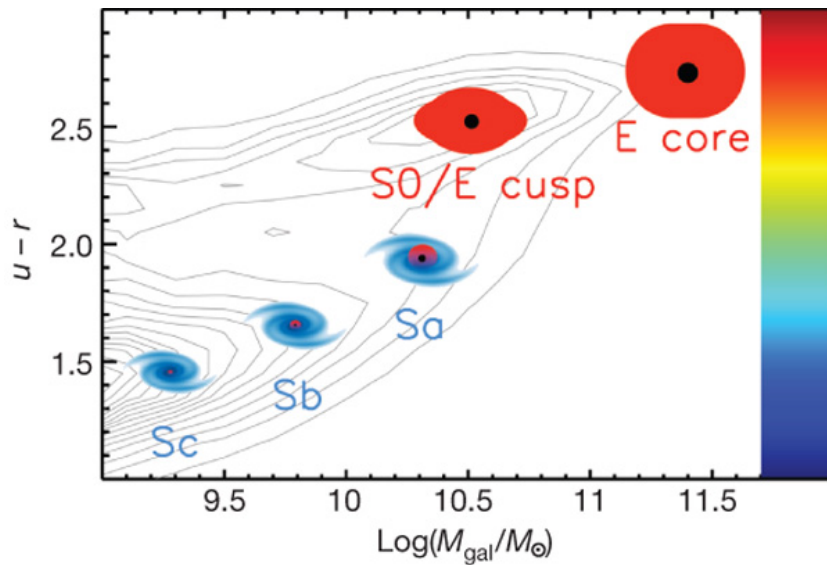


Figure 2.2: The galaxy bimodality: early-type galaxy population (E and SO galaxies) with older (redder) stellar population and weak SF processes is concentrated on the top, while late-type spirals (S) with ongoing SF and younger stellar population are on the bottom. Credits: [Cattaneo et al. 2009](#), [Kormendy & Bender 2012](#)

needed for the formation of new ‘blue’ stars is used up and the light from red giants becomes more dominant with time. Throughout this process, a given galaxy could follow a track from the MS toward the quiescent population passing through the green valley. Moreover, recent studies showed that the distant X-ray selected AGN tend to reside in the green valley ([Nandra et al. 2007](#), [Hickox et al. 2009](#)) pointing to the fact that the central SMBH may also play an important role in the galaxy quenching through the so-called AGN feedback ([Cattaneo et al. 2009](#), [Hickox et al. 2009](#); see Section 3.5).

AGN and host galaxy co-evolution 3

Active galactic nuclei seem to play a significant role in the evolution of their host galaxies and appear to be in close relation with the internal star-formation processes. Such co-evolution between the host galaxy and the supermassive Black Hole (SMBH) at its centre has been suggested by observational studies as well as by simulations, but a definitive proof (the so-called ‘smoking gun’) is still missing.

3.1 The evidence for co-evolution

Several studies in the local Universe showed that the SMBH mass is tightly correlated with some properties of the host galaxy. For instance, the relation between the SMBH mass and the galaxy luminosity (Marconi & Hunt, 2003), bulge mass (Häring & Rix, 2004, Kormendy & Ho, 2013, McConnell & Ma, 2013) and velocity dispersion of stars in the galactic bulge (Ferrarese & Merritt, 2000, Gebhardt et al., 2000, Gültekin et al., 2009, de Nicola et al., 2019) (see Figure 3.1). However, detailed observations of the galaxy classes revealed that these relations are only inherent to elliptical galaxies and spirals with classical bulges, while the pseudobulge galaxies show no correlation and moreover, no sign of correlation with the properties of the disk component. The nature of

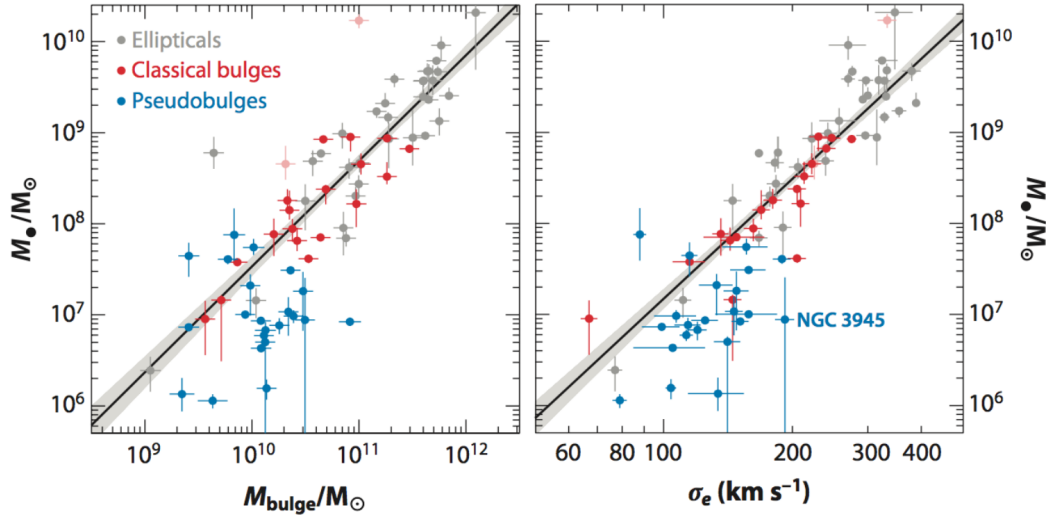


Figure 3.1: The correlation SMBH mass – galaxy bulge mass (left panel) and stellar velocity dispersion (right panel) for pseudobulges (blue points), classical bulges (red points) and ellipticals (grey points). The SMBHs in pseudobulge galaxies show an offset toward smaller M_{BH} from the correlations for classical bulges and ellipticals. Credit: [Kormendy & Ho \(2013\)](#)

such difference can be explained by the different formation mechanism for late and early-type galaxies discussed above. So the formation of ellipticals (and classical bulges) through the dissipative merger allows to deliver matter right to the nuclear region, and hence allows BH to grow up to its present mass (and thus establish the observed correlation). However, pseudobulges were formed by the internal processes and the recent observations confirm that these internal (secular) processes are not efficient to feed AGN. This scenario is also supported by the studies of the relation between SMBH mass and total stellar mass ([Håring & Rix, 2004](#), [Reines & Volonteri, 2015](#)), which found that early-type galaxies have higher SMBH masses than late-type galaxies with the same stellar mass and point out on larger amount of matter available for BH growth in the past for early-type galaxies. In fact, the most massive BH in the local Universe are located exactly in the most massive elliptical galaxies.

The presence of a link between the SMBH and its host galaxy is also supported by the similarities in the evolution of AGN and galaxies. The observational studies of accreting SMBHs over a wide range of redshifts (i.e. cosmic times) show that AGN evolution follows the luminosity-dependent scenario in

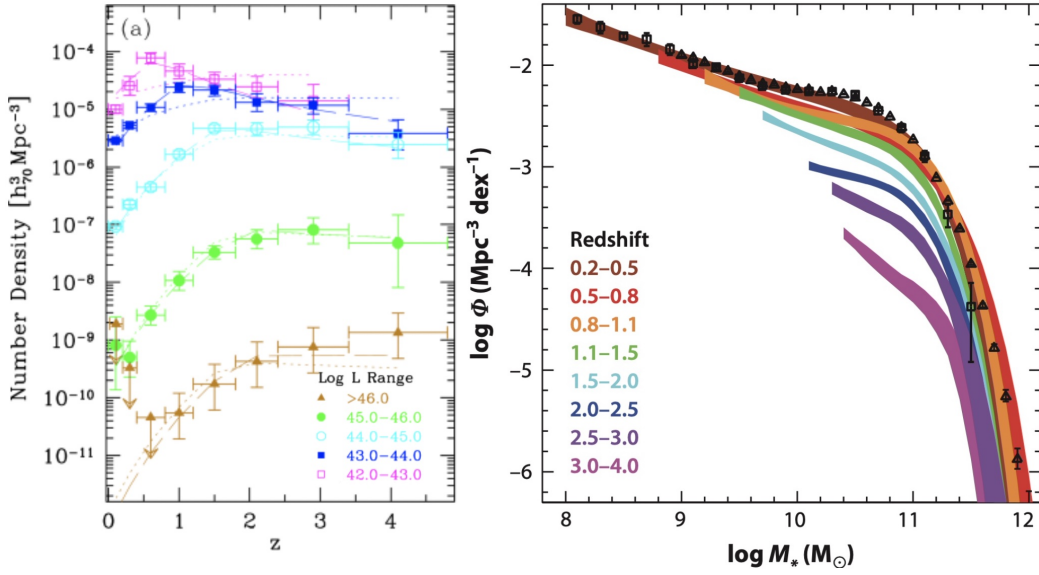


Figure 3.2: Left: The space density of AGNs as a function of redshift in different luminosity ranges. Right: The stellar mass function for the sample of galaxies at $0 < z < 4$ range. Credits: [Hasinger et al. \(2005\)](#), [Madau & Dickinson \(2014\)](#)

which high-luminosity AGN reach the peak of activity earlier (i.e. at higher redshift) than low-luminosity AGN ([Hasinger et al. 2005](#), [Bongiorno et al. 2007, 2012](#), [Ueda et al. 2014](#)). An example of the luminosity-dependent AGN evolution is shown in the left panel of Figure 3.2. So AGN with lower luminosity grow at a slower rate with redshift and as a result a large fraction of local AGN belong to the low-luminosity population, while high-luminosity AGN are rare. At the same time, this evolutionary picture is similar to the so-called ‘cosmic downsizing’ trend observed in star-forming galaxies ([Cowie et al. 1996](#), [Menci et al. 2006](#), [Marchesini et al. 2009](#), [Thomas et al. 2010](#), [Madau & Dickinson 2014](#)), which shows that intensive growth of massive galaxies (or galaxies with high SFR) happened at earlier times (i.e. at higher z). Instead, the local galaxy population is composed of low-to-medium mass galaxies (the most massive elliptical galaxies are rare), which accumulated their mass from the continuous secular processes and possibly minor mergers. An example of this effect is shown in the right panel of Figure 3.2.

In addition to scaling relations and similar evolution, an additional indication of co-evolution between galaxies and their SMBHs is provided by the

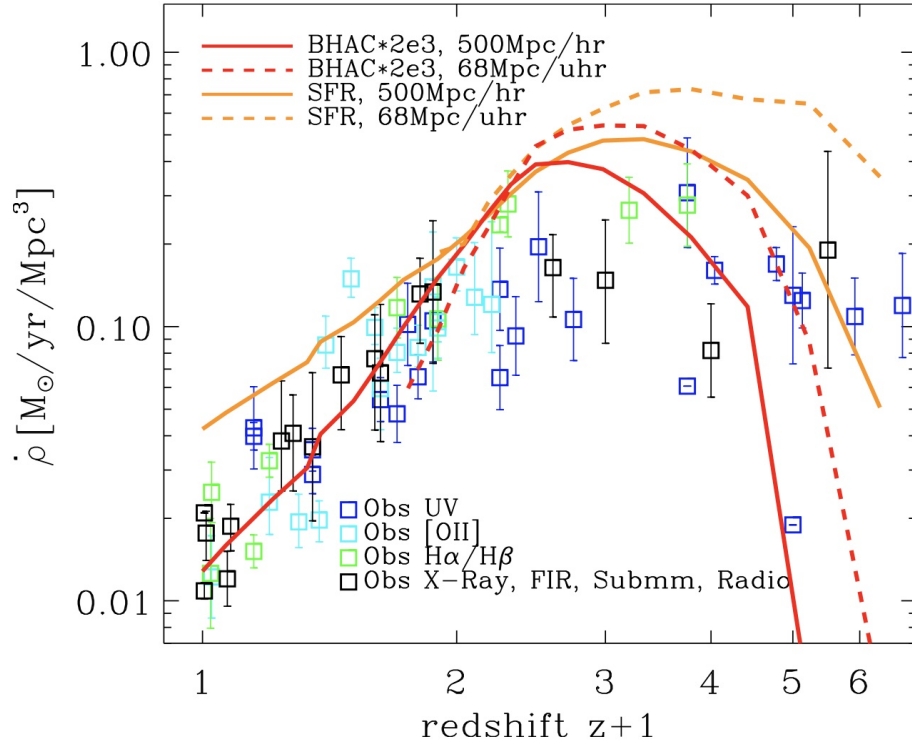


Figure 3.3: The cosmic evolution of mean SFR (orange lines) and BHAR densities multiplied by a factor of 2×10^3 (red lines) obtained by the cosmological hydrodynamic simulations. Credit: [Hirschmann et al. \(2014\)](#)

observed correlations between AGN accretion and star-formation processes in the host galaxy. Several studies ([Dickinson et al. 2003](#), [Delvecchio et al. 2014](#), [Madau & Dickinson 2014](#), [Aird et al. 2015](#)) showed that the shapes of the total AGN accretion curve as a function of redshift and of the global star-formation rate (SFR) are nearly identical, both reaching a peak at redshift $z \sim 1-3$ with a rapid decline toward the present epoch (see Figure 3.3). However, the BH accretion rate (BHAR) reaches a maximum 250–600 Myr after the star-formation peak ([Davies et al. 2007](#), [Schawinski et al. 2009](#), [Wild et al. 2010](#), [Hopkins 2012](#), [Hirschmann et al. 2014](#)). The most possible explanation for this effect is that the intensive star-formation processes (i.e. starbursts) provide the fuel for the Black Hole via stellar winds from massive AGB stars or SN explosion (so-called stellar feedback, see Section 3.5) and therefore enhance the SMBH accretion.

3.2 The SFR-BHAR connection

Several studies showed that moderate-to-high luminosity AGN predominantly lie in galaxies with active star-formation (Merloni et al. 2010, Rosario et al. 2013, Heinis et al. 2016, Aird et al. 2018, Stemo et al. 2020), an observation which can be explained by the cold gas fuelling both AGN activity and star-formation in the galaxy. To establish a connection between BH accretion rate and star-formation rate we need to be able to separate the AGN and host galaxy emission. This issue is non trivial, especially in the local Universe, because the population of local AGN are predominantly low-luminosity sources making their identification difficult in the optical and infrared (IR) bands where the host galaxy emission is dominant. Being produced in the innermost regions of the Active Nucleus, the X-ray emission is a good tracer of the accretion processes, allowing to study the AGN population over a wide range of redshifts down to relatively low luminosities (Alexander & Hickox, 2012). Despite this, previous investigations have found only little correlation between nuclear X-ray luminosity and stellar formation. For instance, AGN with similar X-ray luminosity lie in galaxies with broad ranges of stellar mass and SFR (Mullaney et al. 2012, Aird et al. 2013, Rosario et al. 2013, Azadi et al. 2015). On the other hand, galaxies with the same SFR can contain AGN with a broad range of accretion rates (Aird et al. 2012, Bongiorno et al. 2012, Azadi et al. 2015). The absence of correlation between SFR and accretion rate for the individual objects was explained by the different variability timescales of these two processes (Hickox et al., 2009). In fact even if nuclear activity and stellar formation are connected at any time, the SF is relatively stable over ~ 100 Myr, while AGN luminosity may vary of orders of magnitude on very short time scale $\sim 10^5$ yr (Bongiorno et al. 2012, Mullaney et al. 2012, Aird et al. 2013, Hickox et al. 2014, Paolillo et al. 2017). Therefore, the relation between AGN activity and galaxy properties can be discovered by the study of the average properties of large samples

of objects.

For instance, [Chen et al. \(2013\)](#) used the far-IR-selected galaxies from *Herschel Space Observatory* and AGN selected by IR and X-ray criteria and found a linear relation between the average SMBH accretion rate (BHAR) and SFR for galaxies across a wide range of SFR and with redshifts $0.8 < z < 2.5$. Additionally, a similar relation between SFR and average BHAR (and stellar mass) was found by [Delvecchio et al. \(2015\)](#) on the basis of a far-IR sample of star-forming galaxies and X-ray selected AGN at $z < 2.5$. These and other studies ([Yang et al. 2018](#), [Aird et al. 2019](#), [Stemo et al. 2020](#)) also show that the SFR–BHAR correlation becomes more significant at redshift $z > 0.8$. Additional studies ([Masmoura et al. 2018](#), [Aird et al. 2019](#)) found that the average AGN X-ray luminosity can change depending on the host galaxy position relative to the main sequence (MS) of star-forming galaxies, possibly indicating an enhancement of star-forming processes due to the AGN when its host lies below the MS line and its quenching when the host galaxy lie above the MS. However, [Rovilos et al. \(2012\)](#) and [Shimizu et al. \(2015\)](#) found no evidence of this effect for AGN in the local Universe. Such relations between BHAR/X-ray luminosity and SFR are consistent with a scenario in which AGN activity and SFR are connected over galaxy evolution timescales by the common cold gas supply, but the AGN contribution to galaxy quenching remains controversial.

The study of large statistical samples of galaxies allows to build the BHAR probability function, i.e the probability of a galaxy with a given property (stellar mass, SFR and morphological type) to host an AGN with a given BHAR, and derive the level of AGN activity in the Universe. Several works have shown that the BHAR probability function follows a power-law shape with an exponential cut-off at high accretion rates, flattening or even decreasing toward low BHAR (see Figure 3.4; [Aird et al. 2012](#), [Bongiorno et al. 2012](#), [Aird et al. 2018](#)). Furthermore, the more recent study by [Aird et al. \(2018\)](#) for different host galaxy types shows that quiescent galaxies have typically lower probability of hosting

an AGN than star-forming galaxies pointing toward a lower fraction of cold gas (i.e. lower BHAR) in the quiescent galaxies.

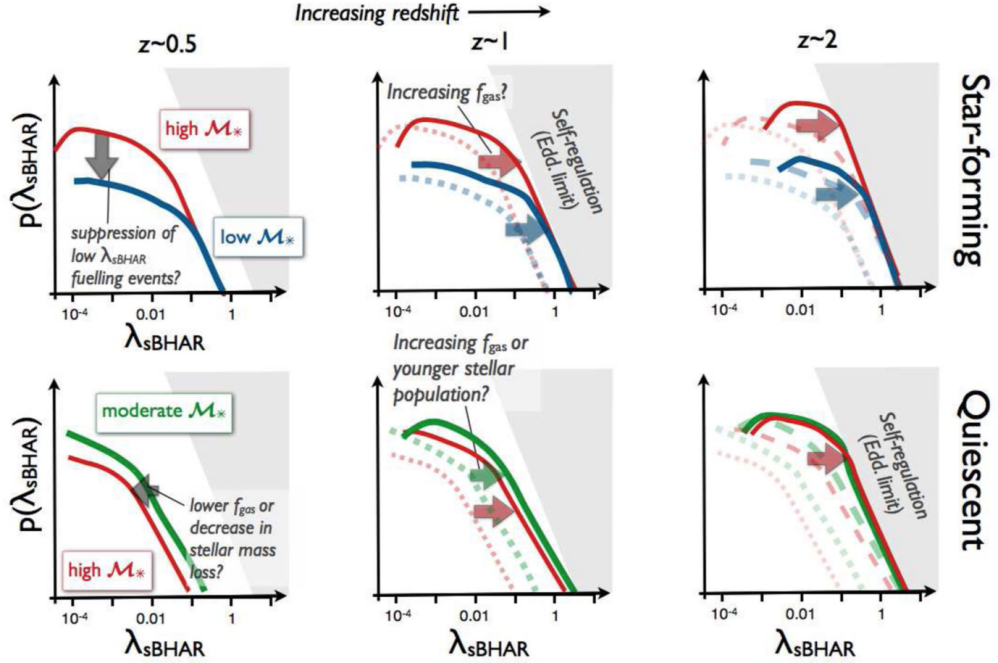


Figure 3.4: A schematic representation of the shape, redshift evolution and stellar mass dependence of the probability distribution of specific Black Hole accretion rates within galaxies of given redshift and stellar mass. Credit: [Aird et al. \(2018\)](#)

3.3 AGN feeding processes

Since the AGN accretion and star-formation processes operate typically on different spatial scales the details of the mechanisms responsible for such co-evolution are still poorly known. The gravitational influence of SMBH becomes dominant only at the scales ≈ 10 pc (this radius is dependent on \mathcal{M}_{BH}), while host galaxy processes like star-formation typically operate on greater spatial scales (from ~ 100 pc up to a few dozens of kpc). To generate a continuous inflow the gas has to lose $\sim 99.9\%$ of its angular momentum going from a stable orbit at $r = 10$ kpc down to nuclear region ($r = 10 - 100$ pc) where it will fall under the gravitational influence of the SMBH.

Hydrodynamical simulations and individual observations of the closest galax-

ies suggest a scenario where a major role in the gas transportation to the galaxy centre can be played by the large-scale gravitational torques produced by major mergers, minor interactions or disk instabilities (Heckman & Best, 2014, Storchi-Bergmann & Schnorr-Müller, 2019). As it was discussed in Section 2.2 major mergers of gas-rich galaxies at high- z can generate a massive gas inflow towards the nucleus of galaxies and trigger the intensive star formation. Many observations also confirm this scenario and found that the most luminous quasars are hosted by galaxies undergoing mergers (Treister et al. 2012, Glikman et al. 2015, Fan et al. 2016). The minor mergers are also able to provide the fuel for low-and-moderate luminosity AGN (Neistein & Netzer 2014, Couto et al. 2016). The brightest example of AGN fueling by a minor merger event is the local Seyfert 1 galaxy Mrk 509 ($z = 0.034$). The calculated accretion rate for this AGN appeared to be unusually high for a Seyfert 1 (Eddington ratio ~ 0.31), but further observations from the Hubble Space Telescope (HST) showed the sign of small galaxy remnant, which is falling into Mrk 509 (Fischer et al., 2015).

Besides major and minor mergers, AGN in galaxy clusters can be fed by accretion of cold gas streamers. These cooling flows are usually generated inside a turbulent galaxy cluster halo through the cooling of hot plasma, which then can condense and fall chaotically into the nucleus region (so called chaotic cold accretion, CCA; Gaspari et al. 2013, 2015, 2018). This feeding mechanism seems to be associated with low-luminosity AGN hosted by classical bulges and ellipticals. Several observations of molecular cloud motions (David et al. 2014, Tremblay et al. 2016, Diniz et al. 2017) and $H\alpha$ filaments (Fabian, 2012, Russell et al., 2016) in nearby galaxies clusters may support this feeding scenario. In case of pseudobulge galaxies a dominant role in AGN feeding is played by the secular (internal) galaxy evolution, where the inward transportation of the gas is due to the gravitational instabilities in the disk (nuclear spirals, bars, rings etc). This scenario is supported by the hydrodynamical simulation of Hopkins

& Quataert (2010), which reveals the formation of a broad range of gas morphologies (including spirals, rings, clumps, ovals, bars with bars) in a circumnuclear region of a few hundred parsecs. However, these morphologies are not smooth and really short-lived, so they cannot sustain a continuous AGN activity. At the same time, they are efficient only down to scales $\sim 10-100$ pc, where the gas required another set of instabilities resulting in small-size additional nuclear spirals or nested bars.

In any case, observing the gas inflow inside individual galaxies is complicated due to the vicinity of the circumnuclear region to bright nucleus. Only spatially-resolved spectroscopy can separate the stellar from gas kinematics and reveal the structural features not visible by photometry alone. In fact some spectroscopic studies compared the gas and stellar kinematics on $< \text{kpc}$ scales for inactive and active galaxies, and found structural features like warps, counter-rotating disks and motions directed outside of the galactic plane only for galaxies hosting AGN (Dumas et al., 2007, Stoklasová et al., 2009, Storchi-Bergmann & Schnorr-Müller, 2019). However, in the case of high luminosity AGN, even spatially-resolved spectroscopy becomes less efficient because of the contamination by the gas outflow generated by strong AGN winds (see details in Section 3.5).

At smaller scales ($< 10-100$ pc) the numerical simulations suggest the presence of a high-density gaseous region which feels negligible effects from axisymmetric galaxy structures (spiral arms and bar), but it seems to have its own set of instabilities, which produce the nested bars and nuclear spirals. The observation of the nearby Seyfert galaxy NGC 1097 detected a gas inflow streaming along such nuclear spiral structures towards the galaxy center on scales ≈ 3.5 pc with velocity $\lesssim 60$ km/s (Fathi et al. 2006, Dumas et al. 2007, Storchi-Bergmann et al. 2007). Moreover, several models suggest that the passage from the region dominated by the host galaxy to the BH gravitational potential can produce warps in the gas, making it unstable and being able to form

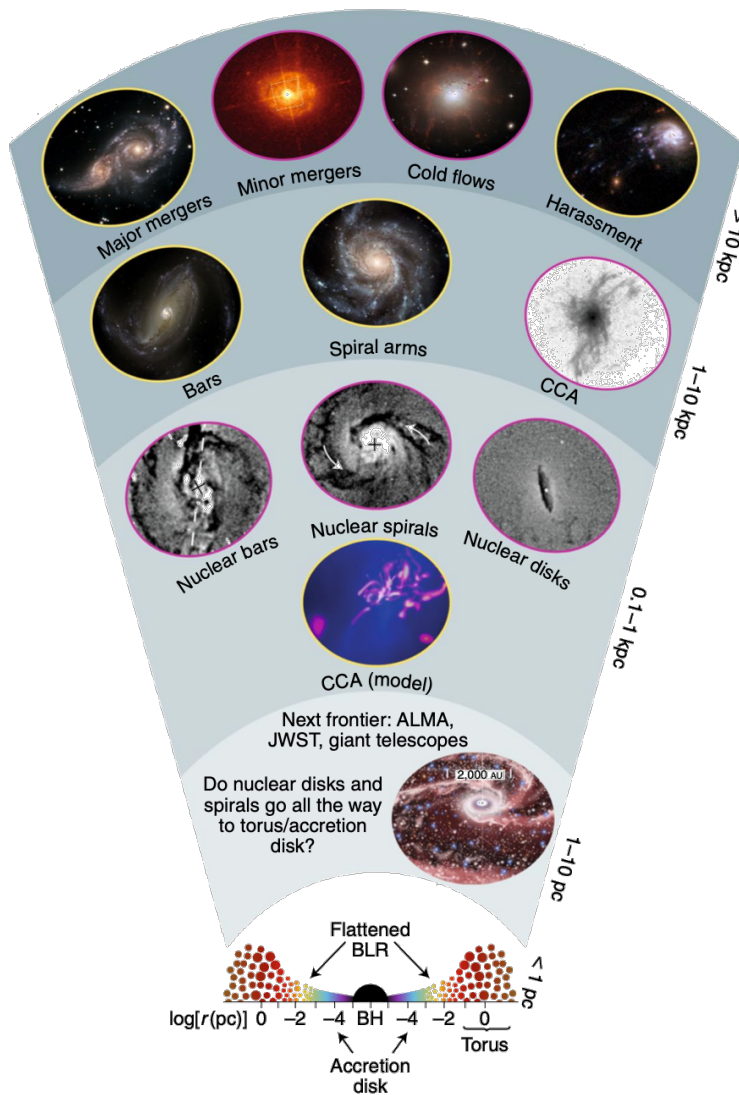


Figure 3.5: The quest for SMBH feeding. Mechanisms of gas inflow to feed SMBHs at the centre of galaxies from extragalactic, to galactic, to 100 pc scales and the next frontier: resolved observations at parsec scales. In the bottom axis, r is the distance from the SMBH, shown in logarithmic scales. Credit: [Storchi-Bergmann & Schnorr-Müller \(2019\)](#)

new stars ([Vollmer et al. 2008](#), [Bregman & Alexander 2009](#), [Schartmann et al. 2009](#)). Such star-formation process depletes the gas reservoir and thereby decreases the AGN activity. Nevertheless, the stars generated in this way can provide recycled material for BH accretion (so-called stellar mass loss; [Schartmann et al. 2009](#)). Moreover, simulations show that stellar winds and SN explosion can significantly enhance the BH mass-accretion rates through the injection of some turbulence in the remaining nuclear gas, which ‘puffs’ it up to torus scales ~ 10 pc ([Hobbs et al., 2011](#)).

A summary of the different mechanisms for gas transportation that were discussed above is schematically illustrated in Figure 3.5.

3.4 Accretion onto the supermassive Black Hole

At scales ≈ 1 pc the gas begins to form the accretion disk under influence of SMBH gravitational force. As it was mentioned in the previous Section, the gas should to lose $\sim 99\%$ of its angular momentum to be accreted onto a Black Hole. The key parameters in this process are the viscosity and the accretion rate. The first one is responsible of transferring the angular momentum outwards through the viscous heating allowing the gas to cool and form the geometrically thin disk-structure. The matter inflow in the accretion disk occurs through a set of Keplerian circular orbits with characteristic accretion rate. This accretion rate can be expressed in the form of the Eddington ratio: the ratio between AGN bolometric luminosity and the Eddington luminosity, the maximum possible accretion that can be sustained in the terms of the equilibrium between the gravitational force acting inward and radiation pressure acting outward (see Section 7.1).

The currently used accretion disk models are thus divided predominantly according to the Eddington ratio of the flow: radiatively efficient accretion ($> 1\%$ of Eddington rate) and radiatively inefficient ($< 1\%$ Eddington).

The model for radiatively efficient accretion proposed by [Shakura & Sunyaev \(1973\)](#) is characterised by the presence of the **optically thick and geometrically thin accretion disk** with high accretion rate (1-100% of Eddington). The viscosity forces and high density of this disk allow the gas to cool efficiently and to emit locally as a black-body from UV to optical wavelength. Heat advection is negligible in this model, and the disk emission is due to gravitational energy release, and hence the accretion efficiency of the flow is set by the position of the ISCO (the innermost stable circular orbit). Such radiatively efficient type of accretion is typical of the ‘classical’ moderate-to-high luminosity AGN and is usually referred to as *radiative-mode AGN*. The structure and main components of radiative-mode AGN were discussed in details in Section 1.2.

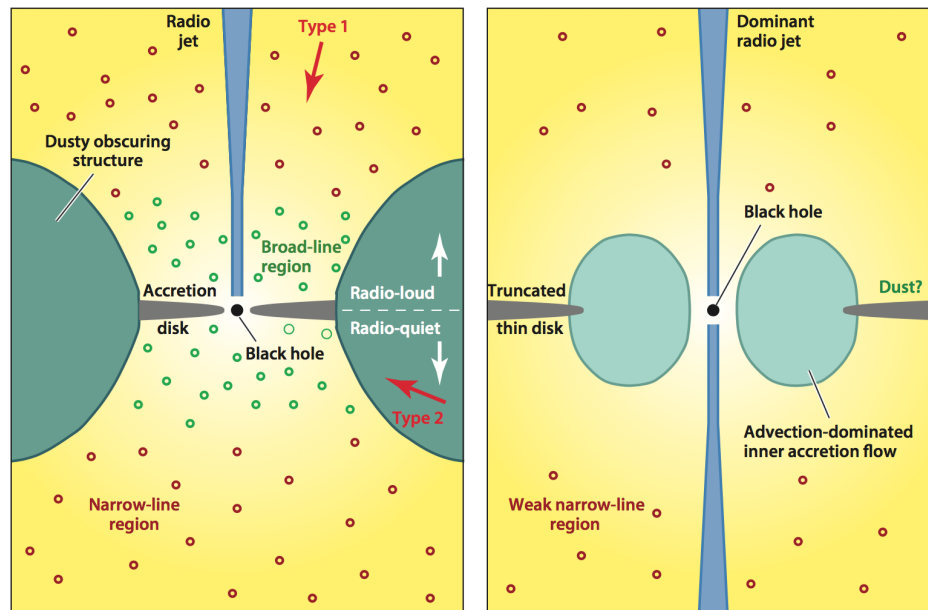


Figure 3.6: A schematic representation of the main components of radiative and jet-mode AGN. Credit: Heckman & Best (2014)

The second model is assumed to be the presence of an **optically thin accretion disk** characterised by a slow accretion (the rate is less than 1% of Eddington). Such slow accretion is unable to cool the gas efficiently and thus the energy is transferred through non-radiative processes such as advective (or convective) transport of energy and angular momentum or an outflowing wind. A significant fraction of the energy is then advected towards the black hole, so-called advection-dominated accretion flow (ADAF) or radiative-inefficient accretion flow (RIAF) (Narayan et al., 1997). Such type of accretion is typical of low-luminosity AGN or *Jet-mode AGN*.

The main characteristic of jet-mode AGN is the production of two-sided collimated jets. Furthermore, the structure of jet-mode AGN seems to be different from radiative-mode AGN (see Figure 3.6). The geometrically thin disk can be absent or truncated in the inner regions, instead the accretion flow becomes a hot, quasi-spherical structure, whose dynamics may be dominated by advection, convection or outflows (Quataert, 2003). This model is supported by the presence of intrinsically hard X-ray emission and the absence of the Big Blue Bump in most of the nearest low-luminosity AGN, which is the classical signa-

ture of a thin accretion disk absence (Ho, 2008, Yuan et al., 2013). Moreover, the observations of low-luminosity jet-mode AGN revealed the absence of strong mid-IR emission and of broad absorption lines in the optical spectra (even in polarised light), which can be the evidence of a missing BLR and dusty torus (Ho, 2008). According to BLR formation models, an important role in the BLR sustainability is played by the radiation pressure and by the wind generated by the central engine (Nicastro 2000, Elitzur & Shlosman 2006). Since radiatively inefficient jet-mode AGN are incapable to generate such wind and they will not be able to sustain the BLR (and torus in some cases; Murray & Chiang 1997, Xu & Cao 2007, Ho 2008).

Historically, radiative-mode AGN have been called either Seyfert galaxies or quasars, while the low-excitation radio galaxies and LINERs with low radiative efficiency and presence of jets are usually referred as the jet-mode AGN. In addition, it is possible that the transition between these modes can be caused by a change in the disk viscosity or in the mass accretion rate, which leads to a transition from an optically thin to an optically thick state (Ho, 2008, Russell et al., 2016). This transition state seems to happen at Eddington ratio of $\sim 10^{-3} - 10^{-2}$.

In addition to the optically thick and thin accretion disks there are two accretion modes, which are commonly used to describe AGN: the spherical *Bondi accretion* with negligible angular momentum (Russell et al., 2016) and the *slim accretion disk*. The first one is usually used to describe the slow accretion of hot gas in massive ellipticals. The second one is characterised by very high accretion rate ($>100\%$ of Eddington) and the presence of radiatively-inefficient advection (Frank et al. 2002, Abramowicz & Fragile 2013, Czerny 2019). The accretion efficiency is lower than in the standard optically thick disk, because part of the is lost through inflow across the BH horizon. This model is used to explain the fast growth of BHs in the early Universe (e.g. super-Eddington quasars).

3.5 AGN and stellar feedback

As discussed in Section 3.1 the co-evolution between central SMBH and its host galaxies can be due to AGN feedback, an interaction between the energy produced by accretion onto the SMBH and the gas in the host galaxy. This process can affect different processes inside the galaxy (and possibly the galaxy cluster) and be responsible for the formation of the galaxy bulge, the termination of star formation, maintaining the hot intergalactic medium and even the self-regulation of SMBH accretion.

According to the AGN feedback paradigm there are two main modes of AGN output (Fabian, 2012, Heckman & Best, 2014). The first one is associated with radiatively-efficient AGNs (see Section 3.4) with energetic output in the form of the electromagnetic radiation generated by the efficient accretion onto the SMBH; the so-called *quasar* mode of AGN feedback. The second one, the *radio* mode of AGN feedback, is associated with less powerful AGN with radiatively inefficient accretion, which generates powerful jets (see jet-mode AGN Section 3.4).

In the quasar mode the interaction of the AGN with the gas in the host galaxy is due to radiation pressure or powerful winds, which heat and/or blow the cold gas away from the galaxy suppressing the formation of stars (*negative AGN feedback*). Through such mechanisms an AGN can quench star-formation (Croton et al., 2006, Rosario et al., 2013) and also significantly reduce its own accretion (self-regulation of the nuclear activity; Fabian 2012). In some cases, AGN feedback affect with the host galaxy in the opposite way triggering the star-formation by compressing the gas in the interstellar medium, i.e. *positive AGN feedback*, (Ishibashi & Fabian 2012, Combes 2017). A schematic view of quasar-mode AGN feedback is presented in the left panel of Figure 3.7.

Quasar-mode feedback is most likely dominant in the most powerful AGN at high redshift. At that stage, the galaxy has a large reservoir of cold gas, which

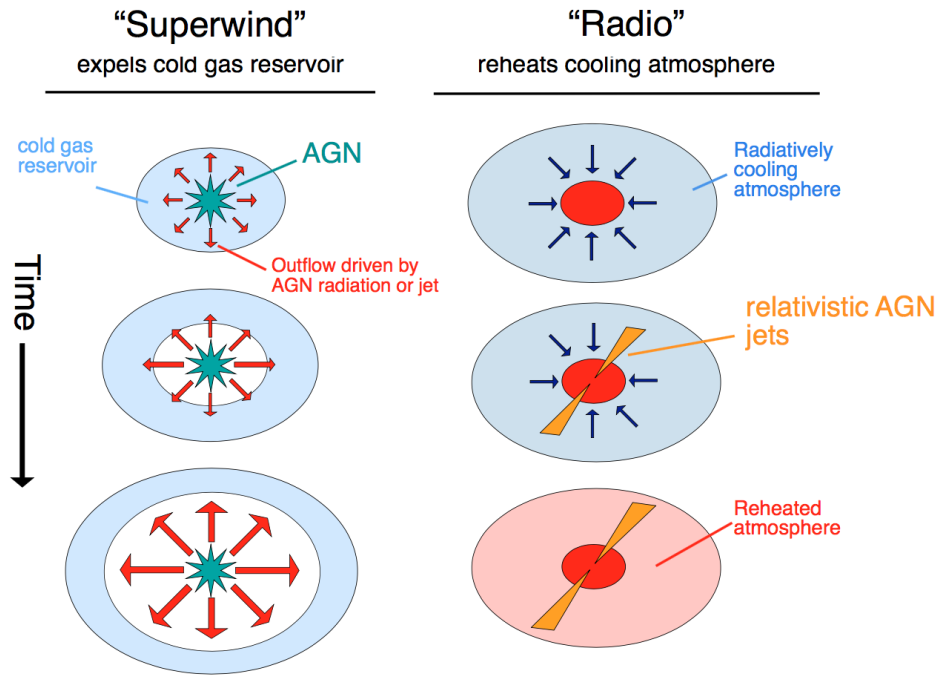


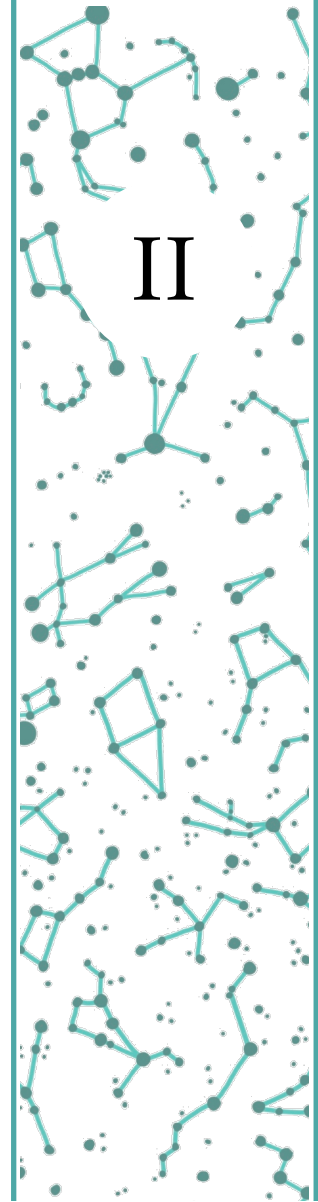
Figure 3.7: Schematic diagrams to illustrate the two main modes of AGN feedback: quasar-mode with ‘superwind’ outflows (high-luminosity AGN) and radio-mode outflows (radio-loud AGN). Credit: [Alexander & Hickox \(2012\)](#)

can be used for BH growth and star formation. However, such high density can probably lead to high obscuration of the central nucleus and hence complicate a direct observations. Direct evidence of AGN winds was found in high- z powerful quasars through the set of blue-shifted absorption lines in their optical/UV spectra (so-called broad absorption lines, BAL quasars). The corresponding outflow velocities for these absorption lines $v_{\text{outflows}} \lesssim 10^4$ km/s. The same lines were also observed in local type 1 Seyfert, but with lower outflow velocities $v_{\text{outflows}} \sim 100 - 1000$ km/s. Most of Seyfert 2 galaxies do not show similar high-velocity outflows indicating either that they are not able to produce such winds, or that their wind operates only on the nuclear scales (~ 10 pc) and thus is not visible. In any case, such a nuclear wind in Seyfert 2 is not able to affect the entire galaxy.

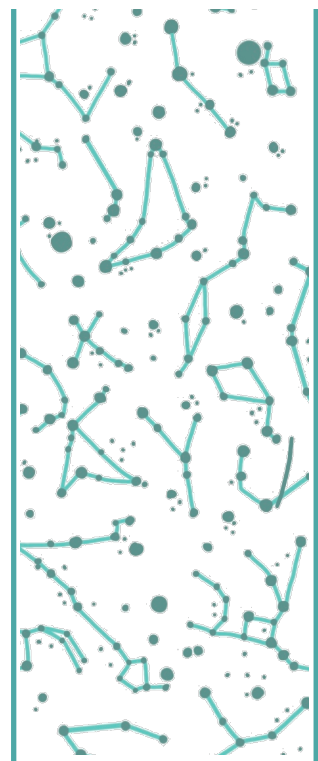
The radio mode feedback is more easily observed in the local Universe, because it tends to occur in nearby massive galaxies with low-luminosity AGN (typically in galaxy groups and clusters). In such systems, the accretion flow

(ADAF or Bondi accretion) is able to produce the powerful jets. These relativistic jets generate expanding radio lobes and inflate bubbles filled with relativistic plasma on either side of the nucleus, which can be clearly observed by X-ray and radio observations. In this way, jets play a key role in the maintenance of the cooling/heating balance inside the elliptical galaxies (and their environment), i.e. they produce a cooling inflows sufficient to feed the low-luminosity AGN, but prevents a strong cooling of the gas and the formation of new stars (Fabian 2012, Morganti et al. 2013, Blandford et al. 2019). The radio-mode AGN feedback is schematically presented on right panel of Figure 3.7.

On the contrary, the presence of active star-formation in the galaxy can affect the central SMBH through stellar feedback. As it was mentioned in Section 3.3 the stellar population in the galaxy nucleus (at scales 10-100 pc) can significantly affect the nuclear accretion reducing it by ‘stealing’ the gas or increasing it by the turbulence injection in the circumnuclear region (Schartmann et al. 2009, Fabian 2012, Heckman & Best 2014). The observations of the most massive stars show that they can generate outflows with velocities up to $v \sim 1200$ km/s, which is sufficient to feed AGN in classical bulges and ellipticals. At the same time, the outflows produced by SN explosions can also heat or blow away the gas in the galaxy nucleus preventing the accretion of gas by the SMBH (Wild et al. 2010, Hopkins et al. 2016).



The host galaxies of AGN in the local Universe



4 The optical and X-ray galaxy samples

4.1 SDSS brief overview

The Sloan Digital Sky Survey (SDSS) is one of the largest imaging and spectroscopic redshift surveys of modern astronomy. The observations began on in 2.5-m wide-angle optical telescope at Apache Point Observatory (New Mexico, USA) in 2000. Nowadays SDSS has 16 data releases, which cover more than 35% of the sky in the Northern hemisphere and contain the photometry for nearly 1 billion objects and spectroscopy for more than 5 million objects.

The imaging camera of the telescope is made up of 30 CCD chips, each with a resolution of 2048×2048 pixels (approximately 120 megapixels in total). All chips combined in 5 rows (6 chips in each row), where each rows has a different optical filter: *u*-band with average wavelengths of $\bar{\lambda} = 3551 \text{ \AA}$, *g*-band with $\bar{\lambda} = 4686 \text{ \AA}$, *r*-band with $\bar{\lambda} = 6165 \text{ \AA}$, *i*-band with $\bar{\lambda} = 7481 \text{ \AA}$ and *z*-band with $\bar{\lambda} = 8931 \text{ \AA}$, the limit magnitudes for each band are 22.0^m , 22.2^m , 22.2^m , 21.3^m , and 20.5^m . The *urgiz*-photometry from these filters allows to select different astrophysical objects (stars, galaxies as targets for the spectroscopic follow-up).

For the spectroscopic observations, SDSS uses two spectrographs, which process the light of source through the optical fiber connected to the specific hole made in a unique aluminum plate. Each hole on this plate is positioned specifically for a selected individual object. Nowadays, the updated spectrograph attached to the telescope is capable to record 1000 spectra simultaneously from one plate; over the course of each night the telescope typically uses between six and nine plates for recording spectra.

Over 20 years SDSS completed four observations phases, which were dedicated to the observation projects concentrated around the study of the Milky Way stellar population, processes inside local galaxies and distant active galactic nuclei.

The first and second phases of SDSS was concentrated on the spectroscopic study of more than 800 thousand galaxies, which allowed to map galaxies in filaments and voids and reconstruct the large-scale structure of the Universe. During the second phase, SDSS also began the project Sloan Extension for Galactic Understanding and Exploration (SEGUE) in order to study the stellar population of Milky Way and create the detailed 3-dimensional map of our Galaxy.

The third SDSS phase worked from 2008 to 2014 and consists of four separate surveys. The SEGUE-2 was continued from the previous phase extending the studies of the Galactic stellar halo. At the same time, the largest fraction of the observational time was dedicated to the main spectroscopic project Baryon Oscillation Spectroscopic Survey (BOSS), which was focused on mapping of the spatial distribution of quasars and LRGs and the measurement of the expansion rate of the Universe. The new project APO Galactic Evolution Experiment (APOGEE) was designed to study the red giant stars in the inner region Milky Way with the usage of high-resolution and high signal-to-noise IR spectroscopy. One more survey for the study of the Milky Way, Multi-object APO Radial Velocity Exoplanet Large-area Survey (MARVELS) was created to moni-

tor the radial velocities of bright stars inside our Galaxy and to detect their gas giant exoplanets.

The fourth SDSS phase began in 2014 with the extension of APOGEE-2 and BOSS (eBOSS) projects. In addition to these projects Mapping Nearby Galaxies at APO (MaNGA) survey dedicated to the detail mapping of the nuclear processes in the nearby galaxies with the usage of spatially resolved spectroscopy.

At the end of 2020 SDSS began the new fifth phase. At first, the collaboration will embark in modernisation and automatisisation of some processes on the SDSS telescope. The main goal of the fifth phase is the detail mapping of the interstellar gas of nearby galaxies (the Local Volume Mapper survey) and the analysing of their supermassive Black Holes (the Black Hole Mapper survey). In addition, the Milky Way Mapper survey is going to target the spectra of six million stars inside the Milky Way.

4.2 galSpec SDSS galaxy samples

Our galaxy sample is based on the *galSpec* catalogue of galaxy properties¹ which was produced by the MPA–JHU group as a subsample of the main galaxy catalogue from the 8th Data Release of the Sloan Digital Sky Survey (SDSS DR8). The stellar masses in the catalogue are obtained through Bayesian fitting of a grid of models to the SDSS *ugriz* photometry and two spectral indicators (the so-called Balmer decrement D_n4000 and $H\delta_A$ absorption line). The D_n4000 and $H\delta_A$ indicators provide the ages of the stellar populations in galaxies and allow to separate continuous and star formation histories dominated by bursts. The set of simulated observables (the spectral indices D_n4000 and $H\delta_A$, the $g-r$ and $r-i$ colours, the burst mass fraction over the past 2 Gyr, the dust-attenuation correction and the stellar mass-to-light ratio) were derived of a library of synthetic spectra created assuming the different star-forming histories and a wide range of metallicities; the initial mass function was adopted as

¹https://www.sdss.org/dr12/spectro/galaxy_mpajhu/

in [Kroupa \(2001\)](#). The comparison of the simulated D_n4000 and $H\delta_A$ with observed ones allowed to get estimates of the dust-attenuation correction and the stellar mass-to-light ratio for each galaxy in the catalogue. For each accepted model the total stellar mass was computed by multiplying the dust-corrected galaxy luminosity in the z-band by stellar mass-to-light ratio predicted by the model. The more detailed description of the stellar masses determination and its accuracy are presented in [Kauffmann et al. \(2003\)](#), [Tremonti et al. \(2004\)](#).

The estimate of the galaxy star-formation rate (SFR) was obtained in two different ways described in [Brinchmann et al. \(2004\)](#). In short, the object selection was based on the BPT criteria ([Baldwin et al., 1981](#)), according to which the objects with high signal-to-noise for four specific emission lines were classified as ‘star-forming galaxies’, ‘AGN’ and ‘composite’. The BPT criteria cannot be applied if the objects have low S/N value ($S/N < 3$) for at least one of the required emission line, therefore such objects were classified as low S/N star-forming galaxies and AGN. The objects with weak emission lines or no line at all were marked as unclassified (see [Brinchmann et al. \(2004\)](#) for details). The values of SFRs for SFGs and low S/N SFGs were determined using the $H\alpha$ emission line luminosity. However, such SFR estimates can be underestimated due to the absorption by galaxy dust. Therefore, the SFR estimates based on $H\alpha$ luminosity are corrected for dust extinction on the basis of the Balmer decrement, D_n4000 ([Kauffmann et al., 2003](#)). In addition, the $H\alpha$ line is not an accurate indicator of SFR for all galaxies. Firstly, some galaxies do not have $H\alpha$ line in their spectra or it can be blended with close emission lines (such as $N\text{II } \lambda 6583$). Secondly, according to the BPT-diagram classification, a major fraction of galaxies in *gal-Spec* catalogue have an active nucleus and therefore the $H\alpha$ line is due to both star formation and accretion processes. In these cases the SFR was inferred from the empirical relation between SFR and $D4000$ ([Kauffmann et al., 2003](#)). All SFR measures are corrected for the fiber aperture following the approach proposed by [Salim et al. \(2007\)](#). The stellar masses \mathcal{M}_* and SFRs are computed

by assuming a Kroupa IMF (Kroupa, 2001) and are adjusted to a Chabrier IMF (Chabrier, 2003).

The *galSpec* catalogue contains reliable spectroscopic information for about 1.5 million galaxies with redshift $z \leq 0.33$. We selected objects with reliable spectroscopic parameters (i.e. with `RELIABLE != 0`) and redshift (i.e. with `zWarning = 0`; see Aihara et al. 2011, for further details). Additionally, *galSpec* catalogue may have multiple spectroscopic observations for an individual galaxy. Some of these objects were intentionally re-observed, as part of a different program or survey, or as part of a repeated plate observation. Therefore we rejected such duplicates and choose only objects which are ‘primary’ in the sample using the `mode` flag (for ‘primary’ objects `mode = 1`). The values of SFR and \mathcal{M}_* for duplicate observations are very similar, with the majority of the objects in agreement within a few percent. In any case, objects with low quality SDSS photometry in r and i bands were excluded from our sample due to the need of accurate r - and i -band magnitudes for AGN selection described in Section 5.2. For this purpose, we used the basic photometric processing flags recommended on SDSS website² to clean the sample from objects with deblending (`PEAKCENTER != 0`, `NOTCHECKED != 0`, `DEBLEND_NOPEAK != 0`) and interpolation problems (`PSF_FLUX_INTERP != 0`, `BAD_COUNT_ERROR != 0` and `INTERP_CENTER != 0`). The magnitudes and photometric flags for our sample were obtained by the online service CasJobs SDSS SkyServer. After excluding all objects described above our final SDSS sample consists of 703 422 galaxies. The redshift distribution of our final galaxy sample is shown in Figure 4.1.

4.3 The galaxy distribution on the SFR– \mathcal{M}_* diagram

The distribution of galaxies on the SFR– \mathcal{M}_* plain demonstrates that most galaxies can be separated into two main populations (as also discussed in Section 2.2).

²https://www.sdss.org/dr12/algorithms/photo_flags_recommend/

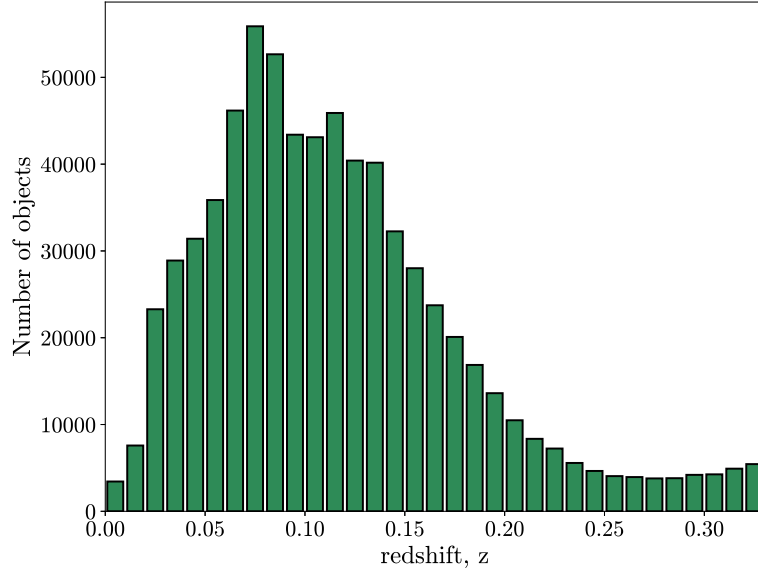


Figure 4.1: The redshift distribution for our final SDSS galaxy samples.

First, the ‘star-forming’ galaxies (SFGs) with steady processes of new stars formation and generally late-type morphologies with significant disc components (e.g. [Faber et al. 2007](#), [Noeske et al. 2007](#), [Blanton & Moustakas 2009](#), [Aird et al. 2017](#)), and second, the ‘quiescent’ galaxies with passively evolving stellar populations and early-type morphologies. The distribution of our sample on SFR– \mathcal{M}_* plane is shown in Figure 4.2.

We classify galaxies in our sample as star-forming or quiescent based on their SFRs relative to the evolving ‘star-forming main sequence’ setting the threshold between the two classes 1.3 dex below the main sequence defined by [Aird et al. \(2017\)](#), and given by:

$$\log \text{SFR}_{\text{cut}}(z) [\mathcal{M}_{\odot} \text{year}^{-1}] = -8.9 + 0.76 \log \mathcal{M}_* / \mathcal{M}_{\odot} + 2.95 \log(1 + z). \quad (4.1)$$

Galaxies that fall below this cut were classified as passive or quiescent while those above the line as star-forming. Note that the relation in Equation 4.1 is redshift-dependent so that for the classification we used the redshift of each individual object.

Our final sample consists of 703 422 galaxies, of which 376 938 are classified as star-forming (53.6%) and 326 484 as quiescent galaxies (46.4%), respectively.

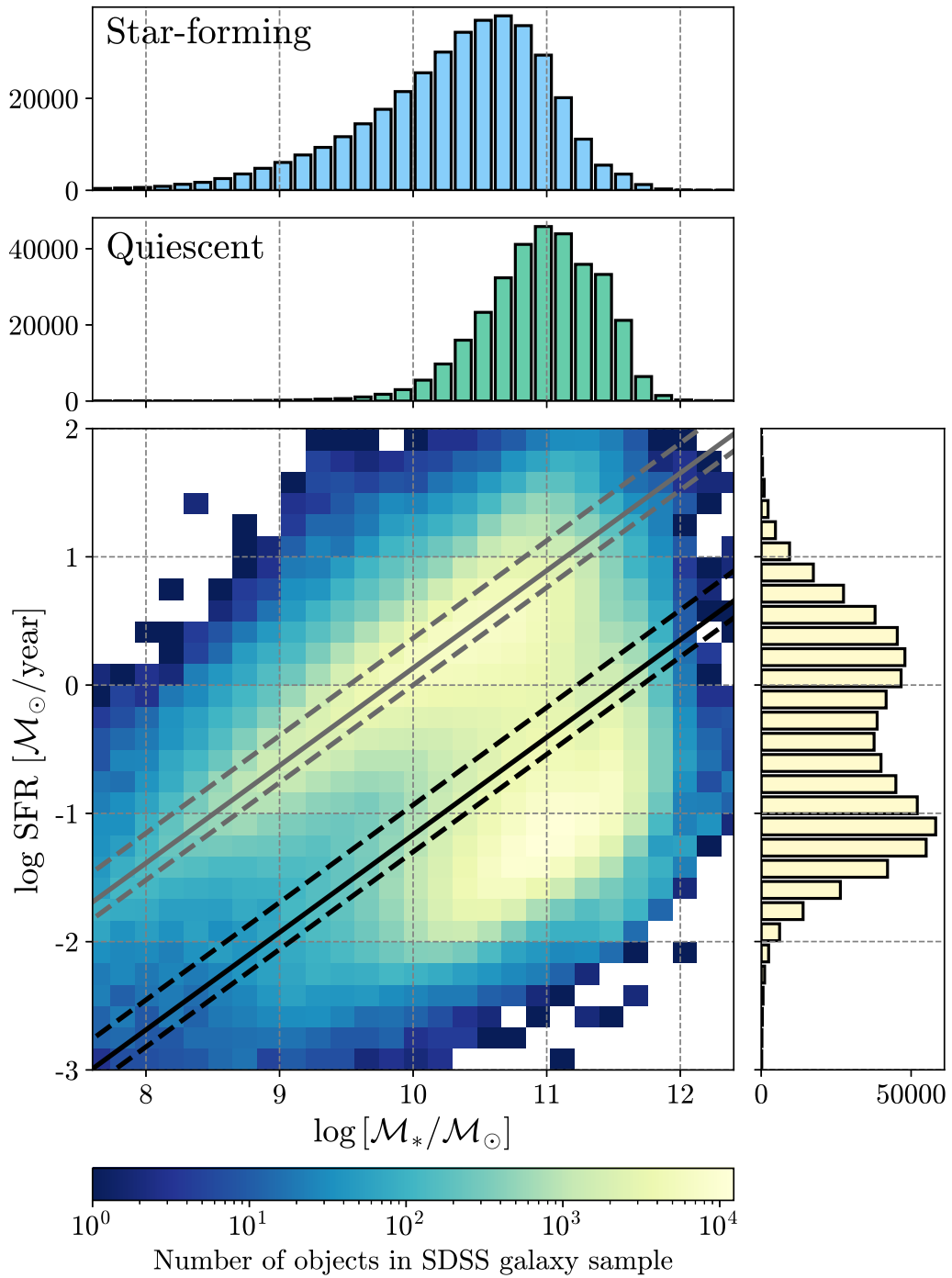


Figure 4.2: The distribution of star-formation rate vs. stellar mass for our final SDSS galaxy sample. The right and top histograms represent the distribution of our sample in SFR and M_* . The individual objects with X-ray emission found in 3XMM-DR8 catalogue are shown by grey circles. The grey lines show the main sequence (MS) of star-forming galaxies defined by Equation 4.1. All objects were divided into star-forming and quiescent galaxies by the cut 1.3 dex below the MS of SFGs (black lines). The bottom dashed, solid and top dashed lines correspond to the lowest, mean and highest redshift in our sample ($z = 0.00, 0.11, 0.33$), respectively.

4.4 The XMM-Newton Space Telescope and its source catalogues

XMM-Newton or X-ray Multi-Mirror Mission is an X-ray space observatory launched by the European Space Agency in December 1999. The mirror system of X-ray telescopes is different from optical telescopes, because the aluminised parabolic mirrors usually possessed by normal optical telescope absorb the high-energetic X-ray photons and hence are not able to reflect them. This problem is solved by the usage of the nested cylindrical paraboloid and hyperboloid surfaces, which provide a low grazing angle and therefore are capable of reflecting X-ray photons. The *XMM-Newton* mirror system consists of 58 gold-coated nested mirrors with the diameters from 30 to 70 cm (the thickness of the mirror substrates varies from 0.47 to 1.07 mm). As a result, the total effective geometric area of the mirror is 4650 cm^2 (Jansen et al., 2001), which makes *XMM-Newton* the telescope with the largest effective area among other X-ray telescopes. The advantage of such large collective area is the ability of the telescope to make long uninterrupted exposures providing highly sensitive observations. However, such complicated mirror system complicates the focusing of the incoming X-ray photons and therefore degrades the angular resolution of the telescope (it is near $6''$ for *XMM-Newton*).

The *XMM-Newton* has on board three imaging cameras, two spectrometers and an optical telescope. The primary instrument is set of the European Photon Imaging Cameras (EPIC), which is composed of a single PN-CCD camera and two MOS-CCD cameras (with total field of view of 30 arcminutes). The energy sensitivity range for EPIC cameras is between 0.15 and 15 keV (or 82.7 to 0.83 \AA). The cameras have three types of the filters transparent for X-ray and can be independently operated in a variety of modes depend on the image sensitivity and required exposure. The PN camera is used to detect high-energy X-rays sources and consists of a single silicon chip with 12 individual CCDs

(each 64×189 pixels). On the contrary, the MOS cameras are used to detect low-energy X-rays. Each camera is composed of seven silicon chips, where one chip is in the centre and six around it (each chip containing a matrix of 600×600 pixels). The field-of-view (FOV) for EPIC cameras is $30'$.

The secondary system inboard of the spacecraft is the pair of Reflection Grating Spectrometers (RGS), which are composed of two Focal Plane Cameras and their associated Reflection Grating Arrays. These systems are used to obtain the X-ray spectroscopic data and operate at energy range from 0.35 to 2.5 keV (5 and 35 Å, respectively). Such energy range allows to detect the spectral lines of several chemical elements (such as iron, carbon, nitrogen, oxygen) and study the chemical abundance of the X-ray sources.

In addition, *XMM-Newton* has a small optical/ultraviolet telescope (i.e. Optical Monitor), which was designed to provide simultaneous observations together with other spacecraft's instruments. The sensitivity range of the optical monitor lies between 1700 and 6500 Å in a $17' \times 17'$ square field of view co-aligned with the centre of the X-ray telescope's field of view.

All the data obtained by the *XMM-Newton* telescope are used to produce the XMM-Newton Serendipitous Source Catalogues. In the present work, we use 3XMM DR8, which contains the information from 10 242 EPIC observations made between 2000 and 2017. In total, 3XMM DR8 contain more than 775 thousand detections, of which 531 thousand are unique sources, which cover 1089 square degree (2.64%) of the sky (Rosen et al., 2016). The catalogue includes information for each source in 5 basis bands with energy ranges of 0.2–0.5 keV, 0.5–1.0 keV, 1.0–2.0 keV, 2.0–4.5 keV and 4.5–12.0 keV, and 4 broad bands: soft (0.2–2.0 keV), hard (2.0–12.0 keV), total (0.2–12.0 keV) and XID (0.5–4.5 keV) bands. In addition, the spectra and lightcurves are provided for more than 32% of the detections.

However, the latest publicly available data release of *XMM-Newton* is 4XMM DR10, which was released at the end of 2020 (Webb et al., 2020). We do not use

the latest 4XMM DR10 due to lack of sensitivity maps, which are required for BHAR distribution reconstruction in Section 7.2.

4.5 The crossmatch between SDSS galaxy sample and XMM-Newton catalogue

To quantify the accretion onto the central SMBH we used data from the XMM-Newton Serendipitous Source Catalogue³ (3XMM DR8, [Rosen et al. 2016](#)). The comparison of our optical sample with 3XMM footprint revealed that only 40 914 objects fall in the area of the sky observed by *XMM-Newton*. The distribution of both SDSS galaxy sample and 3XMM footprint on the sky is shown in Figure 4.3.

The crossmatch of 3XMM DR8 with our optical sample (with a matching radius of 5'') gives 3742 X-ray counterparts (the spurious identification rate is about 6.4%). Firstly, we rejected all objects with the detection flag⁴ `SUM_FLAG` ≥ 3 , which indicates problems with the detection such as sources with a low coverage on the detector, sources in problematic areas near a bright source etc. Secondly, we selected objects with zero extension parameter to avoid including spatially extended objects (such as hot gas regions or galaxy clusters). In Section 8.3 we evaluated the effect of including the extended sources on our results.

The XMM catalogue contains the observations from three cameras PN, MOS1 and MOS2⁵. For our study we selected detections from the most sensitive PN camera. For objects with multiple observations we choose the one with the highest exposure time. When the data from PN camera were missing we used those from MOS1 or MOS2 cameras. This choice is motivated by the requirement to use robust flux upper limits in Section 7.2.

³http://xmmssc.irap.omp.eu/Catalogue/3XMM-DR8/3XMM_DR8.html

⁴https://xmmssc-www.star.le.ac.uk/Catalogue/3XMM-DR4/col_flags.html

⁵<https://www.cosmos.esa.int/web/xmm-newton/technical-details-epic>

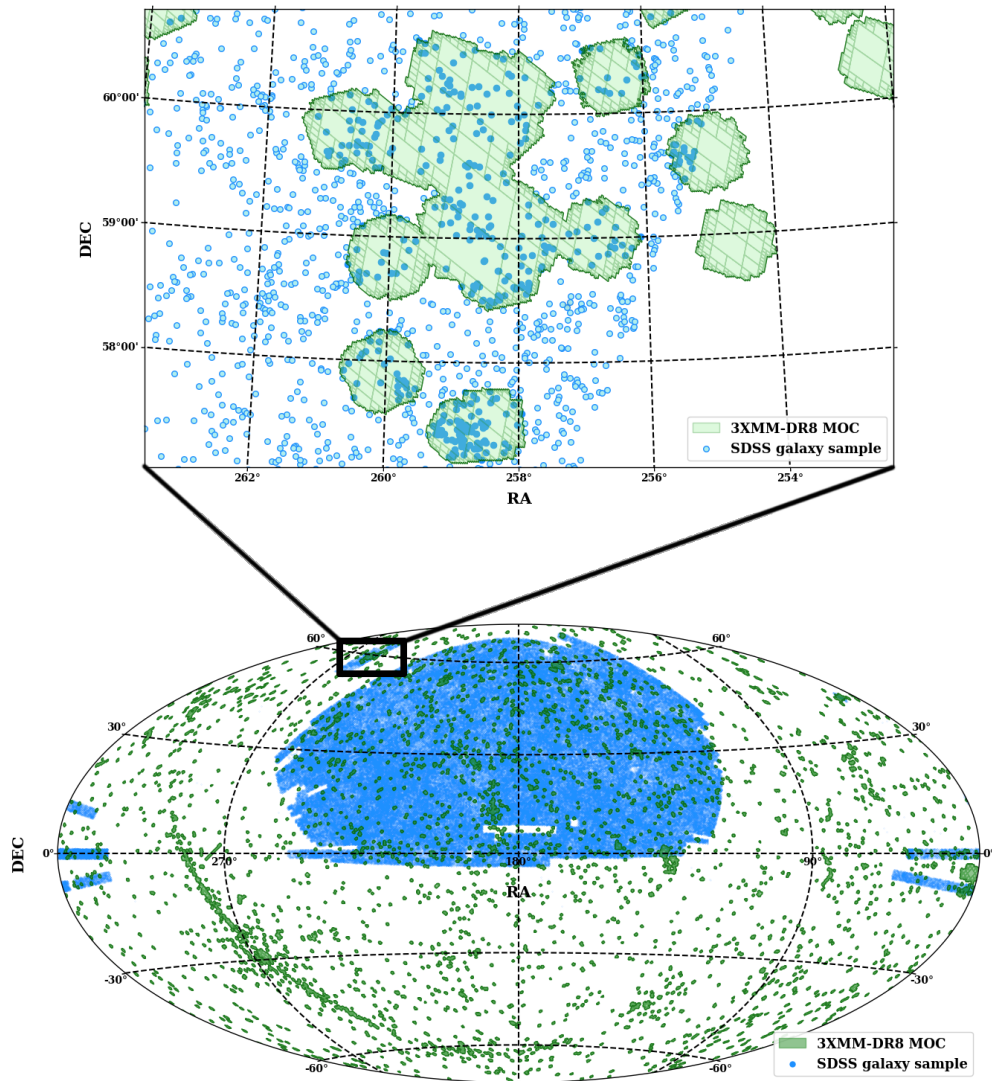


Figure 4.3: The distribution on the sky of all galaxies from our SDSS galaxy sample (blue color) and the 3XMM footprint area (green color). The top panel shows the enlarged area of the map, where the optical galaxies inside the area observed by XMM-Newton are showed by filled blue circles, while the objects outside the footprints are marked by open blue circles.

After all these constrains the final 3XMM-SDSS sample contains 1953 objects (991 star-forming and 962 quiescent galaxies); their distribution on SFR- M_* plane is shown in Figure 4.4 by grey circles. The number of sources obtained at each step of data reduction is presented in Table 4.1.

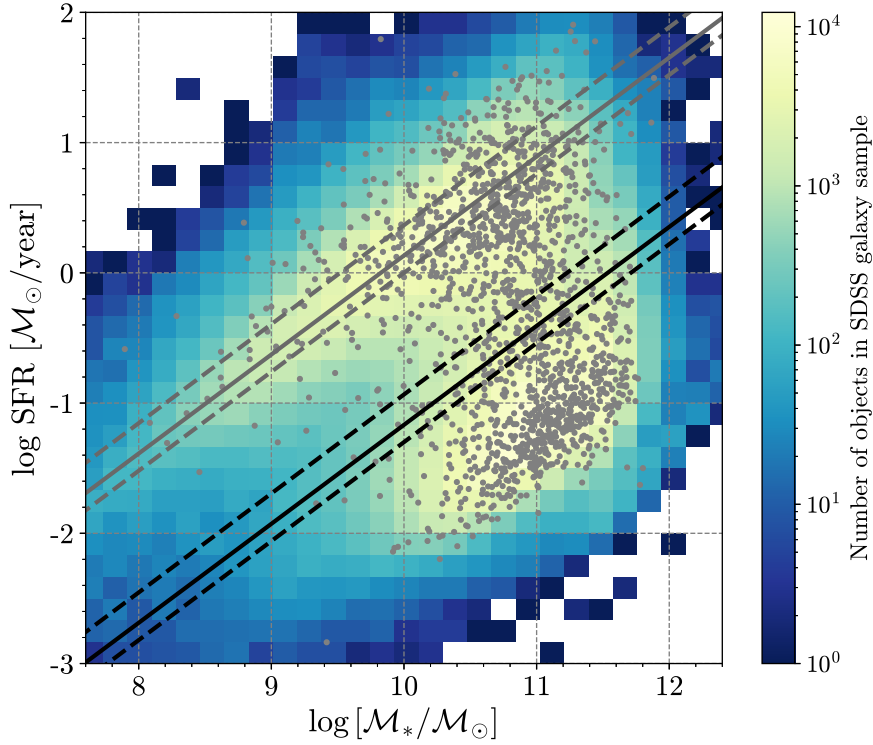


Figure 4.4: The distribution of star-formation rate vs. stellar mass for our SDSS galaxy sample. The distribution of individual objects with X-ray emission found in 3XMM-DR8 catalogue is shown by grey circles.

Table 4.1: The number of sources obtained by the crossmatch of our SDSS galaxy sample and 3XMM-DR8 catalogue at each step of data reduction (see description in the text).

The name of the sample	The number of sources
The SDSS galaxy sample	703 422
The SDSS sample in the 3XMM footprint	40 914
3XMM counterparts for the SDSS sample	3742
• the sources with <code>SUM_FLAG < 3</code>	3352
• the extended sources	343 ^a
• the sources with one X-ray detection	1613
• the sources with multiple X-ray detections	340 ^b
The 3XMM-SDSS sample	1953

^athe total number of detection with non-zero extension parameter; some extended sources have multiple observations;

^bwe choose the detection with the highest exposure time (340 objects), while the total number of all the detections for these 340 sources is 1396.

5 Multiwavelength identification of AGN

In order to identify AGN and study the properties of their host galaxies we need to identify the presence of nuclear non-stellar emission. Since our primary sample is based on an optical SDSS ‘galaxy’ catalogue, which by definition excludes quasar and other sources strongly dominated by nuclear emission, the majority of our sources are type 2 AGN. This type of AGN are partially obscured and provide the opportunity to observe emission not only from the nuclear region, but also from the host galaxy. Given the presence of both nuclear and star-formation emission in the galaxy we used a combination of multiwavelength techniques to identify ‘classical’ AGN.

5.1 Optical selection: BPT-diagrams

A common technique to distinguish AGN from normal star-forming galaxies is the so-called BPT diagram discovered by [Baldwin et al. \(1981\)](#) and improved by [Veilleux & Osterbrock \(1987\)](#). It is based on the comparison of the flux ratios of two pairs of strong emission lines with different level of ionisation. Since these ratios are almost completely insensitive to reddening or to errors in the

spectrophotometry, it is useful for separating AGN and star-forming galaxies due to the different processes producing these emission lines in their spectra.

MPA-JHU SDSS catalogue already has the BPT classification flag (BPTCLASS inside *galSpecLines* file), which is based on $[\text{O III}] \lambda 5007/\text{H}\beta$ ratio versus the ratio $[\text{N II}] \lambda 6583/\text{H}\alpha$ (hereinafter BPT- $[\text{N II}]$) described in detail in [Brinchmann et al. \(2004\)](#) work. The galaxies were classified as star-forming galaxies (SFGs), AGN or composite objects that have contribution from both AGN and star-formation. Additionally, [Brinchmann et al. \(2004\)](#) defined two additional classes: SFGs and AGN with low S/N for at least one of the emission lines required for the BPT classification. The residual objects with no emission lines at all were marked as unclassified.

To verify the BPT classification already presented in the MPA-JHU SDSS catalogue we used the empirical criteria by [Kauffmann et al. \(2003\)](#) to separate the ‘pure’ SFGs from composite objects and [Kewley et al. \(2006\)](#) to separate the latter from AGN. We use fluxes and its errors for each emission line from the *galSpec* catalogue, derived by [Brinchmann et al. \(2004\)](#) and [Charlot et al. \(2002\)](#). Since the application of the BPT selection criteria requires the objects with $\text{S/N} > 3$ for all four emission lines, we selected 1260 objects (64.5%) from our 3XMM-SDSS sample which satisfied the S/N condition for emission lines required for BPT- $[\text{N II}]$ diagram. Additionally, we refine the BPT classification using the two other diagnostic diagrams proposed by [Kewley et al. \(2006\)](#) that involving the ratios $[\text{O I}] \lambda 6300/\text{H}\alpha$ (BPT- $[\text{O I}]$) and $[\text{S II}] \lambda 6717/\text{H}\alpha$ (BPT- $[\text{S II}]$) to distinguish the two classes of narrow-line AGN: Seyfert 2 and low-ionisation nuclear emission line objects (LINER). In this case, we selected 1165 objects (59.7% of our 3XMM-SDSS sample) and 947 (48.5%) objects in the BPT- $[\text{S II}]$ and $[\text{O I}]$, respectively.

The results obtained by BPT- $[\text{N II}]$ coincide with the BPT flag obtained by [Brinchmann et al. \(2004\)](#) and it is presented on top panel of Figure 5.1. The BPT- $[\text{O I}]$ and BPT- $[\text{S II}]$ diagrams are shown in Figure 5.1 (bottom panel).

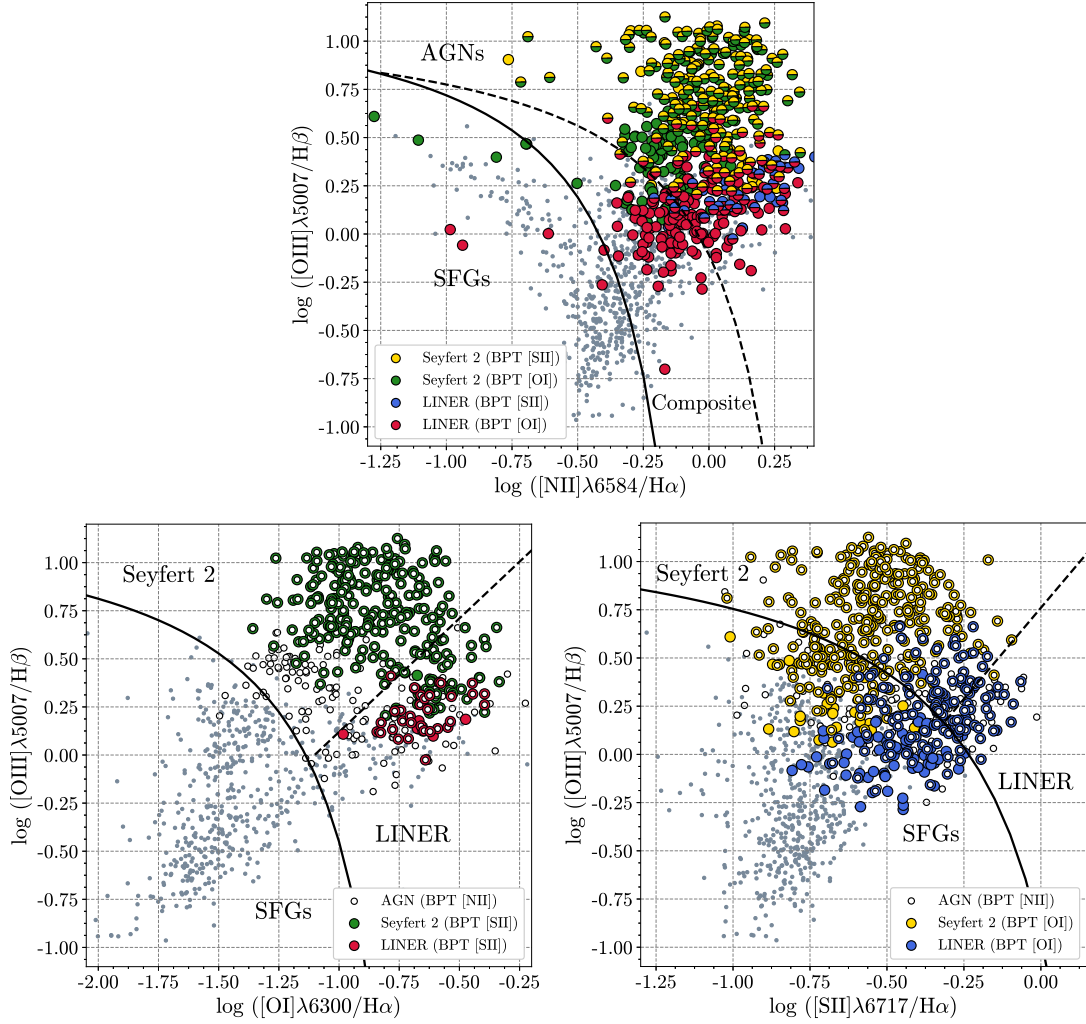


Figure 5.1: The BPT-diagrams for the 3XMM-SDSS sample. Top: $[O\ III]\lambda 5007/H\beta$ vs $[N\ II]\lambda 6583/H\alpha$ flux ratios diagram. The solid line represents the empirical criterion defined by [Kauffmann et al. \(2003\)](#) for separating star-forming and composite galaxies. The dashed line is the criterion by [Kewley et al. \(2006\)](#) for AGN identification. The color circles show AGN identified by two other diagnostic criteria based on the $[S\ II]\lambda 6717$ and $[O\ I]\lambda 6300$ lines. Bottom and left: $[O\ III]\lambda 5007/H\beta$ vs $[O\ I]\lambda 6300/H\alpha$ flux ratios. The criteria of [Kewley et al. \(2006\)](#) for SFG/AGN and Seyfert 2/LINER separation are represented by the solid and dashed lines, respectively. The colour circles show AGN identified by the two other criteria based on the $[N\ II]\lambda 6583$ and $[S\ II]\lambda 6717$ lines. Bottom and right: $[O\ III]\lambda 5007/H\beta$ vs $[S\ II]\lambda 6717/H\alpha$ flux ratios. The colour circles show AGN identified by the two other diagnostic criteria on the basis of $[N\ II]\lambda 6583$ and $[O\ I]\lambda 6300$ lines.

We found that 553 objects were classified as AGN in the BPT-[N II] diagram, 318 as Seyfert 2 and 189 as LINER at least by one of BPT-[S II] or [O I] diagrams and 50 objects were classified as Seyfert 2 by one diagram and LINER by another. The number of classified objects for each BPT diagram is presented in Table 5.1. The distribution of these objects on the star-formation rate–stellar masses diagrams (see Figure 5.2) shows that 15.2% of sources in our 3XMM-SDSS sample, classified as AGN due to BPT-[N II], are located in SFGs and 13.2% in quiescent galaxies. Simultaneously, Seyfert 2 identified by BPT-[S II] and/or BPT-[O I] are mainly in SFGs (11.7%) and only 4.6% in quiescent galaxies. On the contrary, a higher percentage of LINER is located in quiescent galaxies (5.7%) while only 4.0% in SFGs. These results are consistent with the paradigm that LINERs are located mostly in host galaxies with little star formation and older stellar population (Kauffmann et al. 2003, Ho 2008, Heckman & Best 2014 and may show the presence of a strong jet (Falcke et al., 2004).

The BPT-diagram is powerful for AGN identification in optical band, but it has several significant limitations. As it was mentioned before the application of BPT method requires high-S/N detection of 4 emission lines. For example, objects with strong [O III] λ 5007 line which is a reliable tracer of AGN activity can not be classified without the presence of less intense lines such as $H\beta$, [N II] etc. However, the most powerful AGN can also be selected only in the presence of strong [O III] λ 5007 and an upper limit on $H\beta$ by the criterion of $\log([O III]/H\beta) > 1$. Additionally, some AGN have weak or no emission lines due to high obscuration by the circumnuclear and galactic dust. Furthermore, some SFGs may contain a low-luminosity AGN, which may not be identified since the emission of the star-forming processes will dominate the spectrum.

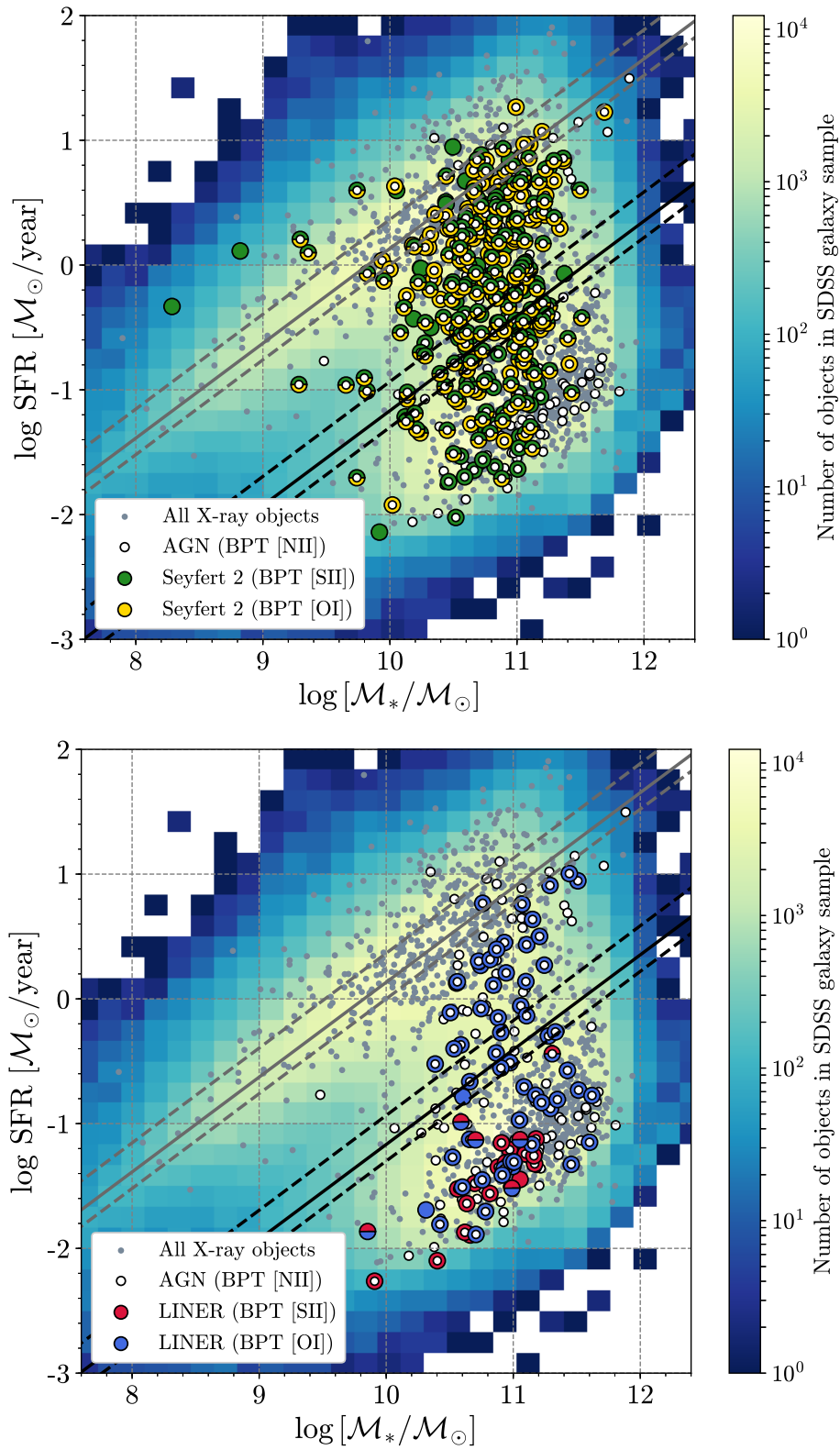


Figure 5.2: The distribution of star-formation rate vs. stellar mass for X-ray sample in hard band (grey circles). The gradient from blue to yellow shows the 2D histogram of the density distribution of galaxies in our optical SDSS sample. The black and grey lines are the same as in Figure 4.2. All symbols represent the AGN selected by the BPT criteria shown in Figure 5.1.

Table 5.1: The number of galaxies classified as star-forming, composite and AGN according to the BPT diagrams (see description in the text and Figure 5.1).

	BPT-[N II]	BPT-[S II]	BPT-[O I]
the total number of objects ^a	1260	1165	947
star-forming galaxies	333	838	436
composite	374	—	—
AGN	553	327	511
Seyfert 2	—	270	291
LINER	—	57	220

^athe total number of objects with $S/N > 3$ for all four emission lines required for each BPT selection criteria.

5.2 X-ray AGN selection criteria

As can be seen in the previous section the proper separation of AGN and host galaxy emission component is complicated in UV/optical band, where the host galaxy emission is dominant. This issue is more critical in the local Universe because the population of local AGN is dominated by low-luminosity sources. However, accretion of matter onto SMBH also produces more energetic emission, which is not typical of the main stellar population of the host galaxy. Thus, X-ray observations are a powerful tool to derive the AGN component separately from the host galaxy emission and allows us to examine the AGN population properties over a wide range of redshifts down to relatively low luminosities (Brandt & Hasinger 2005, Alexander & Hickox 2012). Furthermore, being produced in the innermost regions of the Active Nucleus, the X-ray emission is an good tracer of the accretion rate.

We classified an X-ray source as an AGN if it satisfied at least one of the following three criteria: (1) an intrinsic luminosity $L_X \geq 3 \cdot 10^{42}$ erg s⁻¹ in the hard band; (2) X-ray-to-optical flux ratio of $\log(f_X/f_{\text{opt}}) > -1$ and (3) X-ray-to-IR flux ratio of $\log(f_X/f_{\text{Ks}}) > -1.2$. Such X-ray luminosity threshold is usually

adopted as a criterion to select AGN due to fact that normal galaxies rarely exceed $\sim 10^{42}$ erg/s (Fabbiano, 2006). A similar physical motivation is at the origin of the empirical X-ray-to-optical and X-ray-to-IR flux relations (Maccacaro et al. 1988, Mainieri et al. 2002, Xue et al. 2011); thus stars and normal galaxies typically show smaller ratios $\log (f_X/f_{\text{opt},K_S}) < -2$, while powerful AGN exhibit larger ($\log (f_X/f_{\text{opt}}) > -1$ and $\log (f_X/f_{K_S}) > -1.2$).

The last two criteria, X-ray/optical and X-ray/IR ratios, were calculated in the form:

$$\log (f_X/f_j) = \log f_X + \frac{\text{mag}_j}{2.5} + C_j, \quad (5.1)$$

where f_X is the hard-band detected flux, f_j is f_{opt} in the SDSS r - or i -band fluxes or f_{K_S} in the 2MASS K_S -band flux; mag_j is the magnitude in r -, i - or K_S -band, C_j is calibration constant determined from band parameters as described in Ananna et al. (2017). The X-ray luminosity in the hard band (2.0–12 keV) was calculated through the following formula:

$$L_X = 4\pi d_L^2(z) f_X, \quad (5.2)$$

where z is the redshift and $d_L(z)$ the luminosity distance is defined as:

$$d_L(z) = \frac{c(1+z)}{H_0} \int_0^z \frac{dz'}{\sqrt{\Omega_M(1+z')^3 + \Omega_\Lambda}}, \quad (5.3)$$

where c is the speed of light, $\Omega_M = 0.3$ and $\Omega_\Lambda = 0.7$ are the normalised values of the present matter density and dark energy density, respectively, and the Hubble constant $H_0 = 70 \text{ km s}^{-1} \text{ Mpc}^{-1}$.

In total, we identified 469 AGN (24.0% of our 3XMM-SDSS sample; hereinafter ‘classical’ AGN), 362 were selected by the X-ray luminosity threshold, 397 and 372 by X-ray-to-optical flux ratio in r - and i -bands and 281 by X-ray/IR flux ratio. Only 212 objects are classified as AGN by all criteria (see a summary in Table 5.2) The redshift distribution of AGN selected by the L_X criterion are shown in Figure 5.3, the X-ray/optical flux ratios in SDSS r - and i -band (top panel) and X-ray/IR flux ratio are presented in Figure 5.4 (bottom panel).

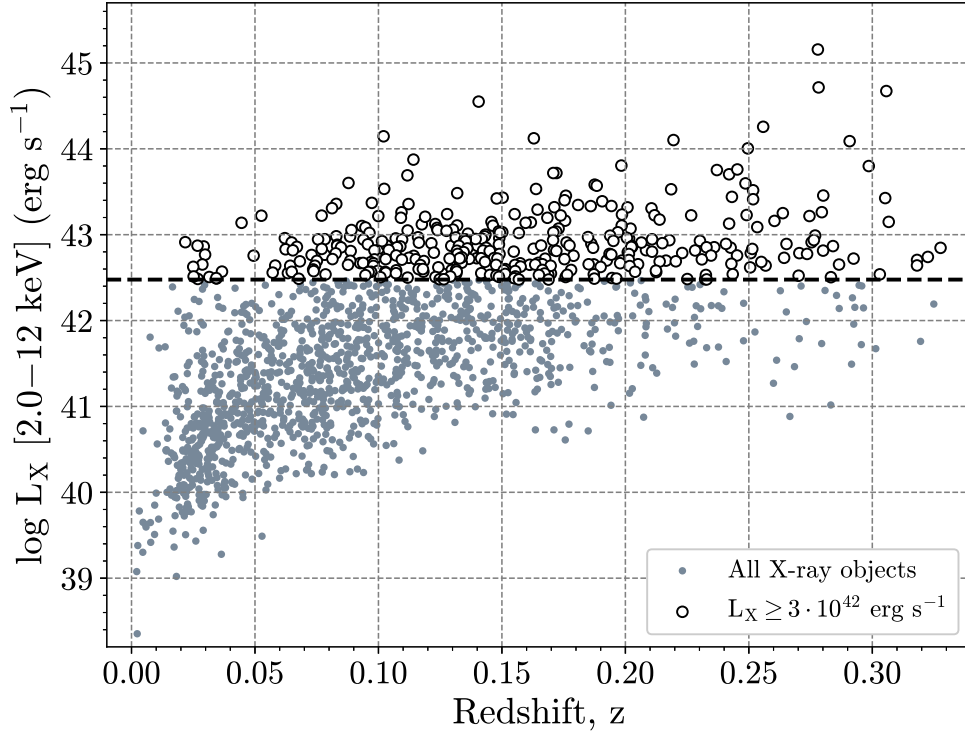


Figure 5.3: The X-ray luminosity vs. redshift for the objects in X-ray sample. The horizontal dashed line indicates $L_{X,\text{int}} \geq 3 \cdot 10^{42} \text{ erg s}^{-1}$ criteria utilized to classify AGN (black circles).

The distribution of our sample on the SFR vs stellar mass diagrams in the hard band is shown in Figure 5.5. AGN selected with the above X-ray criteria tend to occupy predominantly the star-forming main-sequence (67.6% of all X-ray selected AGN), while only 32.4% of AGN were found in quiescent galaxies. Such preference of AGN to be hosted by star-forming galaxies was also found by [Mullaney et al. \(2012\)](#), [Mendez et al. \(2013\)](#), [Rosario et al. \(2013\)](#), [Shimizu et al. \(2015\)](#), [Delvecchio et al. \(2015\)](#), [Aird et al. \(2018\)](#), [Stemo et al. \(2020\)](#) for AGN selected by different IR and X-ray criteria. At the same time, the percentage of star-forming and quiescent galaxies hosting an AGN in our 3XMM-SDSS sample are 32.0% and 15.8%, respectively.

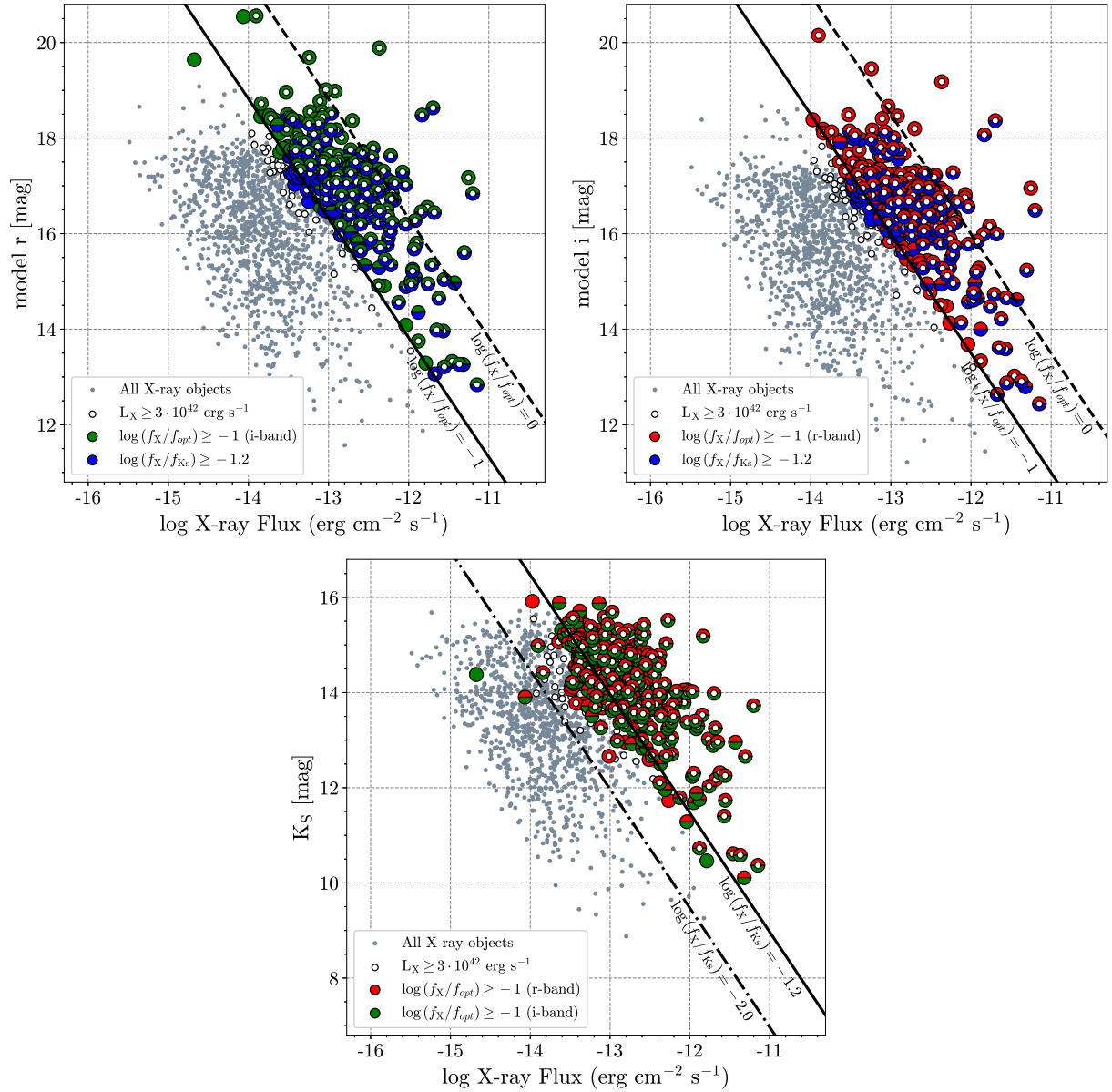


Figure 5.4: Top: The X-ray flux in hard band vs. optical SDSS *r*-band and *i*-band magnitude for sources in our X-ray sample (grey circles). White circles indicate AGN having $L_{X,\text{int}} \geq 3 \cdot 10^{42} \text{ erg s}^{-1}$ in Figure 5.3. AGN selected by the X-ray/optical flux ratios in *r*- and *i*-band are represented by red and green circles, by X-ray/IR ratio by blue circles. Diagonal lines indicate constant flux ratios between the SDSS *r*- and *i*-band and X-ray hard band, the area under the line $\log(f_X/f_{\text{opt}}) > -1$ is used as one of the criteria to classify the location of AGN. Bottom: The X-ray flux in hard band vs. 2MASS infrared *K_S*-band magnitude. The colors of circles are the same as on top panel. Diagonal lines indicate constant flux ratios between the 2MASS *K_S*-band and X-ray hard band, the area under the line $\log(f_X/f_{K_S}) > -1.2$ is used as one of the criteria to classify the location of AGN.

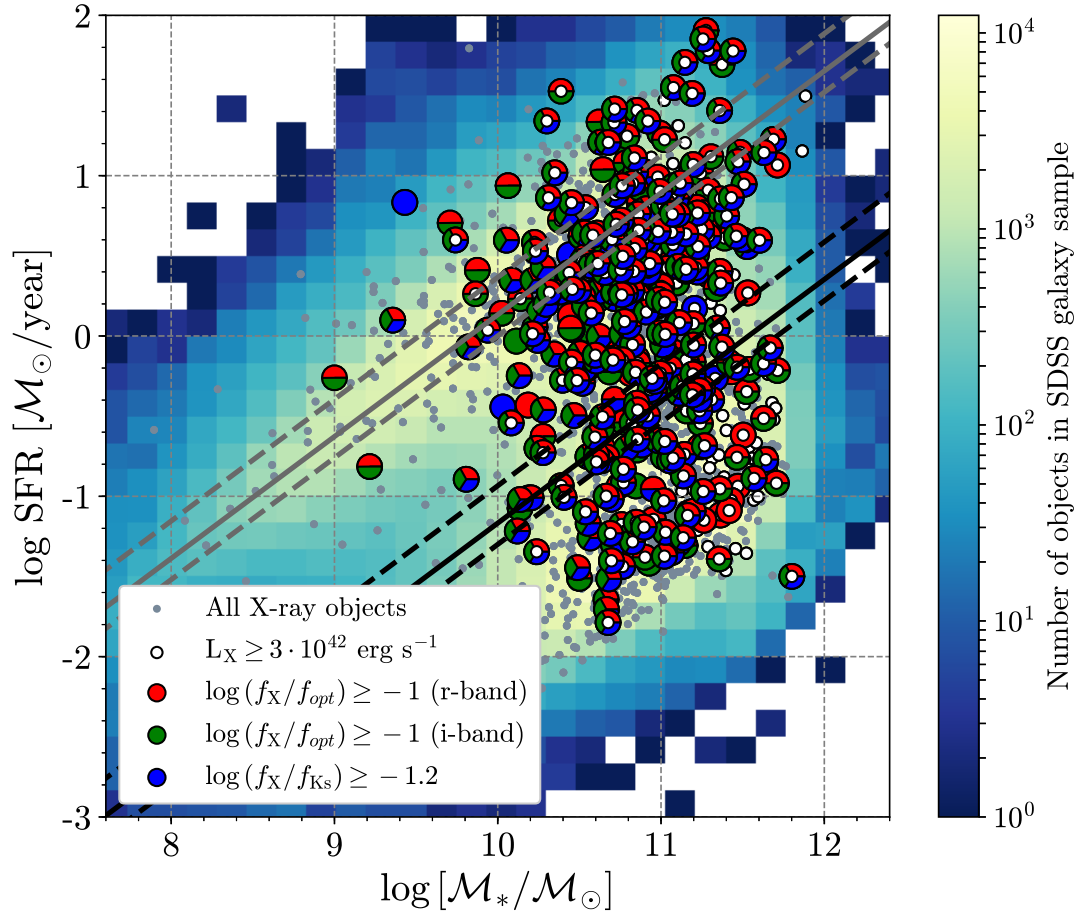


Figure 5.5: The distribution of star-formation rate vs. stellar mass for X-ray sample in hard band (grey circles). The gradient from blue to yellow shows the 2D histogram of the density distribution of galaxies in our optical SDSS sample. The black and grey lines are the same as in Figure 4.2. All symbols represent the AGN selected by the X-ray criteria described in Section 5.2.

Table 5.2: The number of AGN selected by different X-ray criteria (see description in the text).

The name of the sample/criterion	The number of objects
The 3XMM-SDSS sample	1953
The ‘classical’ AGN selected by	469
• the X-ray luminosity threshold	362
• the X-ray-to-optical flux ratio in <i>r</i> -band	397
• the X-ray-to-optical flux ratio in <i>i</i> -band	372
• the X-ray/IR flux ratio	281

5.3 The combination of the optical and X-ray AGN selection criteria

As we have already mentioned in the previous section only 496 (24.0%) of all X-ray sources in our 3XMM-SDSS sample were classified as AGN according to three X-ray criteria. Such small fraction of objects can be explained by the fact that the empirical AGN selection criteria are able to select only the most bright AGN, whose emission dominate their host galaxy emission. We decided to verify this effect and combine AGN selected by different X-ray criteria with the BPT diagrams (see Figure 5.6). It should be noticed that not all 496 AGN selected by X-ray criteria can be verified also by the BPT diagrams due to the lack of one or several emission lines with $S/N > 3$ (see Table 5.3). As a result we found that large fraction of X-ray AGN occupy the area of the optical AGN and composite objects in the BPT-[N II] diagram (see Table 5.3). Moreover, the separation of AGN into Seyfert and LINER by the BPT-[O I] and BPT-[S II] diagrams show that AGN selected by X-ray criteria are preferentially Seyfert 2 than LINER, which are less powerful AGN by definition. However, a significant fraction of X-ray selected AGN also resides in star-forming galaxies region (63.6% and 33.1% in the BPT-[O I] and BPT-[S II] diagrams, respectively), which can be explained by the fact that the part of galaxies in our 3XMM-SDSS sample can be optically obscured AGN and hence they were not selected as AGN by the BPT diagrams.

Furthermore, Figure 5.6 shows that a fraction of objects in SFG and LINER areas that were not classified as AGN by X-ray criteria. This effect can be due to the fact that a galaxy contains low-luminosity AGN, which cannot be selected by X-ray criteria alone. Furthermore, low-luminosity AGN can be present in objects selected as SFG in the BPT diagrams, but their optical emission may be contaminated by the host galaxy or highly obscured by circumnuclear dust.

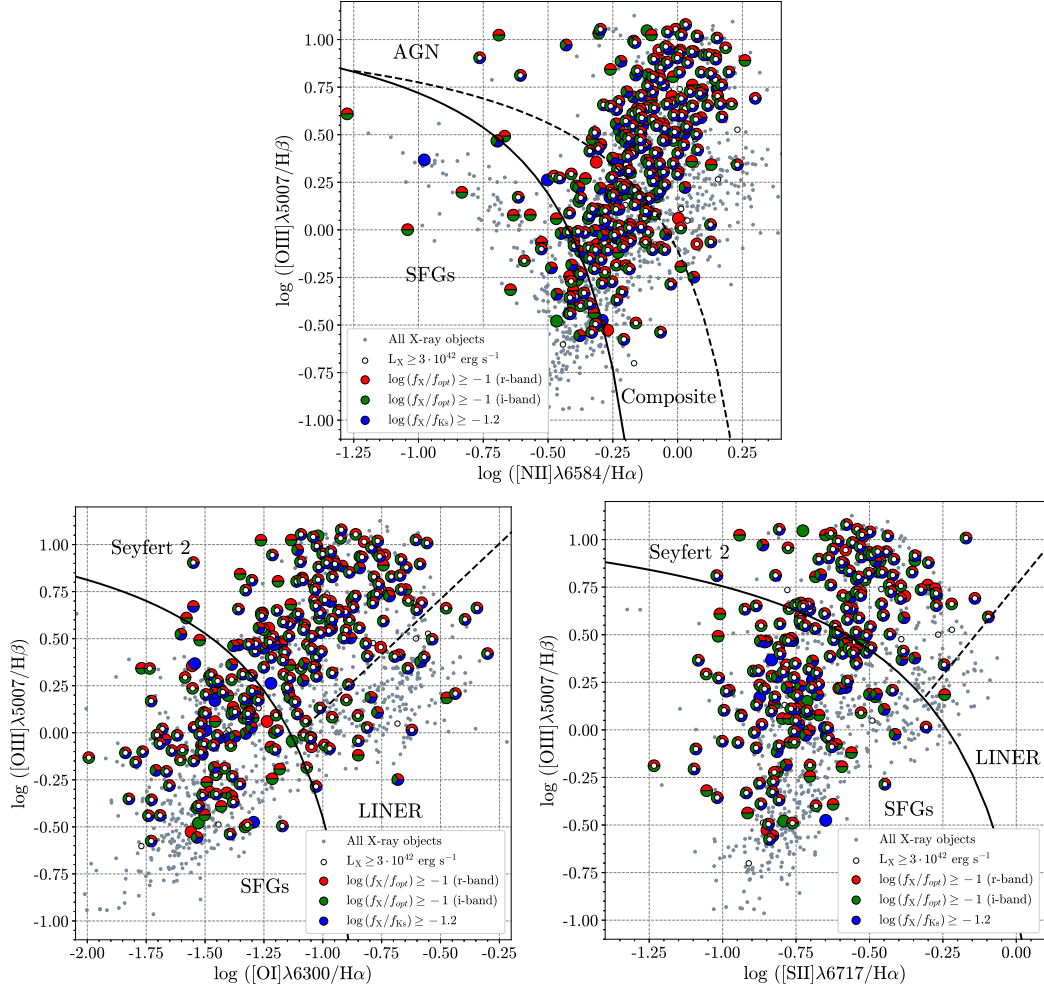


Figure 5.6: The similar BPT-diagrams for the 3XMM-SDSS sample as in Figure 5.1. AGN selected by X-ray criteria are presented by the same symbols and colors as in Figure 5.5.

Table 5.3: The number of X-ray selected AGN classified as star-forming, composite and AGN according to the BPT diagrams (see Figure 5.6).

	BPT-[N II]		BPT-[S II]		BPT-[O I]	
X-ray selected AGN ^a	343		316		257	
star-forming galaxies	43	12.5%	201	63.6%	85	33.1%
composite	112	32.7%	—	—	—	—
AGN	188	54.8%	115	36.4%	172	66.9%
Seyfert 2	—	—	113	35.8%	136	52.9%
LINER	—	—	2	0.6%	36	14.0%

^athe number of AGN selected by X-ray criteria (see Section 5.2) with S/N > 3 for all four emission lines required for each BPT diagram.

6 The X-ray emission from host galaxies and low-luminosity AGN

An estimate of the level of AGN activity from the X-ray emission requires to determine the contribution of the host galaxy. Galaxy populations have different contributions to their X-ray emission; for example, X-ray radiation in star-forming galaxies is mainly due to X-ray binaries. Low mass X-ray binaries (LMXBs) are associated to the old stellar population in bulges of spirals, while high-mass X-ray binaries (HMXBs) are associated to younger stars and are concentrated preferentially in the disk of spirals galaxies. On the other hand, quiescent galaxies with elliptical morphology have only one type of X-ray binaries, i.e LMXBs, but the fraction of X-rays emitted by the hot gas can be significant or even dominate the total emission (Fabbiano, 2006, Kim & Fabbiano, 2013). Hence it is clear that the X-ray luminosity has to be corrected by taking into account the different types of contributions. The correction for our 3XMM-SDSS sample is made separately for the two populations of galaxies (star-forming and quiescent) defined in Section 4.3. Also, we decided to use only the hard X-ray band (2.0–12 keV) since it allows to minimise the contribution from hot gas, SN remnants and other soft X-ray components.

6.1 The K-correction

The expansion of the Universe causes the effect that the extragalactic sources, which observed through the same waveband at different redshifts, have different rest-frame frequencies. In the case of X-ray observations, the energies of the detected photons from a particular object will be $(1+z)$ times lower than the energy actually emitted by it. This means that the flux we measure within a certain waveband does not match the same waveband in the rest-frame of the object. Thus we need the so-called K-correction to convert the flux (or luminosity, magnitude) of object into the frame of the observer.

We computed the rest-frame X-ray luminosities in the hard band (2.0–12 keV) applying the K-correction $k(z)$ to the Equation 5.2 as follows:

$$L_X = 4\pi d_L^2(z) f_X \cdot k(z) = 4\pi d_L^2(z) f_X \cdot (1+z)^{\Gamma-2}, \quad (6.1)$$

where following [Luo et al. \(2017\)](#) we assumed a photon index $\Gamma = 1.4$ appropriate for a moderately obscured AGN spectrum with the absorption column density $\log N_{\text{H}} \simeq 22.5 \text{ cm}^{-2}$ (also see [Tozzi et al. 2006](#), [Liu et al. 2017](#)). Usually the photon index for each individual object can be measured from the X-ray spectral fitting or the ratio of counts in soft and hard wavebands (i.e. hardness ratio). However, the majority of our X-ray sources do not have high quality spectra, while a reliable hardness ratio is available only for 22% of the objects.

6.2 Correction for star formation

Different independent analyses show that X-ray emission from SFGs correlates directly with SFR ([Ranalli et al. 2003](#), Mineo:12, Vattakunnel:12, [Fragos et al. 2013](#), [Symeonidis et al. 2014](#), [Lehmer et al. 2016](#)). We calculated the expected X-ray luminosities of SF galaxies using the scaling relation between $L_{\text{X,SF}}$ and SFR, stellar masses \mathcal{M}_* and redshift z of galaxies from [Lehmer et al. \(2016\)](#) in

the following form:

$$L_{X,\text{hard}} [\text{erg s}^{-1}] = \alpha(1+z)^\gamma \mathcal{M}_*/\mathcal{M}_\odot + \beta(1+z)^\delta \text{SFR} [\mathcal{M}_\odot \text{ year}^{-1}], \quad (6.2)$$

where $\log \alpha = 29.37 \pm 0.17$, $\log \beta = 39.28 \pm 0.05$, $\gamma = 2.03 \pm 0.06$ and $\delta = 1.31 \pm 0.13$ for hard band. The X-ray luminosity vs redshift distribution for SFGs, before and after correcting for the contribution from XRBs, is shown in Figure 6.1.

Since the X-ray luminosity of quiescent galaxies (ETGs) is mainly due to LMXBs and hot gas (Boroson et al. 2011, Kim & Fabbiano 2013, Civano et al. 2014) we have to apply a different type of correction. We use the relation between luminosity of the galaxy in the K -band and L_X of different components of quiescent galaxies. Using 30 normal early-type galaxies observed by *Chandra* Boroson et al. (2011) found that the X-ray luminosity due to LMXBs correlates with K -band luminosity as

$$L_X [\text{erg s}^{-1}] = 10^{29.0 \pm 0.176} \cdot L_K [L_{K\odot}]. \quad (6.3)$$

Other types of stellar sources that can radiate X-rays and therefore provide a contribution to the total X-ray luminosity of the galaxy are coronally active binaries (ABs) and cataclysmic variables (CVs). For their study Boroson et al. (2011) used the *Chandra* observation of M31 and M32 galaxies in hard band (2–10 keV) as their proximity allows us to resolve the individual X-ray sources inside the galaxies. They found a similar relation between X-ray and K -band luminosity:

$$L_X [\text{erg s}^{-1}] = 4.5_{-0.6}^{+0.8} \cdot 10^{27} \cdot L_K [L_{K\odot}]. \quad (6.4)$$

In addition, to evaluate the contribution of the hot gas we used the relation between the X-ray emission and the K -band luminosity in the form $L_X \sim L_K^\alpha$ with exponential slope $\alpha = 4.5$ from Civano et al. (2014).

We used K_S magnitudes from the 2MASS¹ Point Source Catalogue (PSC) and Extended Source Catalogue (XSC), Skrutskie et al. (2006). Firstly, we cross-matched our 3XMM-SDSS sample with the XSC as the galaxies in our sample

¹<https://old.ipac.caltech.edu/2mass/>

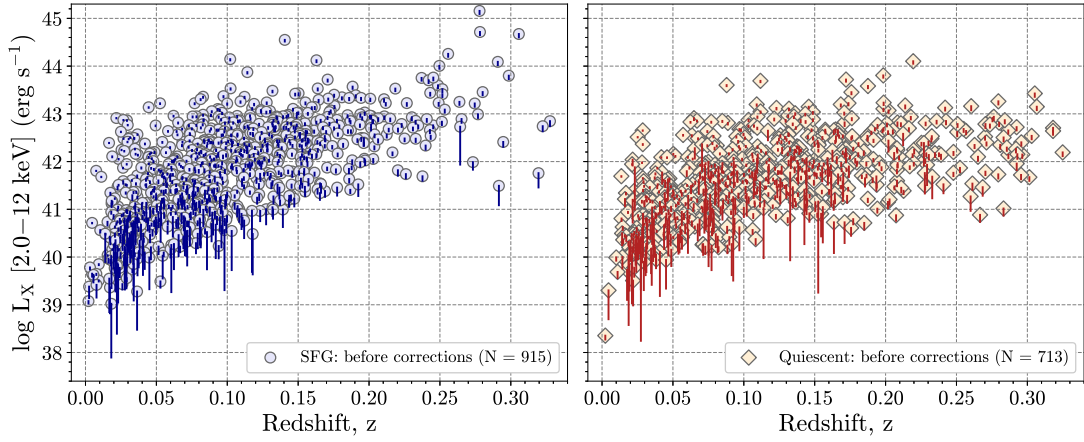


Figure 6.1: The X-ray luminosity vs redshift distribution of the 1628 objects from our 3XMM sample. The uncorrected L_X values for SFGs and passive galaxies are presented on left and right panels as solid circles and diamonds, respectively. The change in L_X after corrections for each object is shown by a solid line.

are located at low redshift and should have extended shapes in 2MASS. Most of the objects in the PSC are stars of the Milky Way, but the catalogue also contains a significant number of unresolved, more distant galaxies; therefore we made additional crossmatch between the PSC and our sample. We found that 1457 objects (74.6% of our 3XMM-SDSS sample) have the counterparts in XSC and 1743 (89.2%) in PSC. 1323 objects in 3XMM-SDSS sample were found in both catalogues because PSC contains entries and point source-processed flux measurements for virtually all extended sources in the XSC. We refined our selection rejecting objects with low S/N, contamination or blending according to the quality flags described in the Explanatory Supplement to the 2MASS² and reduced the number of sources to 1809 (1330 extended and 479 point-like sources).

We calculate the K_S -band luminosity in units of solar luminosity for 921 quiescent galaxies using the equation from Civano et al. (2014):

$$L_{K_S} [L_\odot] = 10^{-(K_S - K_\odot)/2.5} \cdot (1+z)^{\alpha-1} \cdot (d_L [\text{pc}]/10)^2 \quad (6.5)$$

where K_S is the magnitude from the 2MASS catalogue, z is the redshift, and d_L is the luminosity distance in parsecs and $K_\odot = 3.33$ mag is the magnitude

²<https://old.ipac.caltech.edu/2mass/releases/allsky/doc/explsup.html>

of Sun in K -band. To evaluate rest-frame K -band luminosities, we assumed a spectral shape of the type $f_\nu \propto \nu^\alpha$, where $\alpha = -(J - K_S) / \log(\nu_J / \nu_{K_S})$, where $J - K_S$ is colour taken from the 2MASS catalogue.

We determined the X-ray luminosity for AB+CV from Equation 6.4, LMXBs from Equation 6.3 and hot gas components (with the slope $\alpha = 4.5$) and subtracted the luminosities from our intrinsic X-ray luminosity. The redshift distribution of X-ray luminosity in hard band for quiescent galaxies after corrections is shown in Figure 6.1 (right panel).

Our final sample (hereinafter 3XMM AGN sample) contains 1628 objects with positive residual X-ray luminosity after correction for the X-ray emission from binaries and hot gas (83.4% from the 3XMM-SDSS sample before correction), 915 of which are SFGs and 713 are quiescent ETGs.

6.3 AGN host galaxies in the local Universe

Previous study examining the properties of AGN host galaxies show that X-ray AGN prefer to reside in gas-rich massive galaxies with active star formation (Lutz et al. 2010, Mullaney et al. 2012, Mendez et al. 2013, Rosario et al. 2013, Shimizu et al. 2015, Birchall et al. 2020, Stemo et al. 2020 and Section 3.2). We extend these results to low redshift, finding that AGN selected by X-ray criteria (X-ray luminosity threshold, X-ray-to-optical ratio, see Section 5.2) reside mainly on the main sequence of star-forming galaxies (67.6% of all X-ray selected AGN) as opposed to the quiescent galaxy region (only 32.4%) as shown in Fig 5.5. This result shows that the fraction of AGN in SFGs is a factor ~ 2 higher than in quiescent galaxies and it is consistent with the result obtained using different AGN selection criteria. For instance, AGN selected by variability in the optical band (Heinis et al., 2016) or through IR and X-ray criteria (Lutz et al., 2010, Rosario et al., 2013, Stemo et al., 2020) show that AGN are more likely hosted by galaxies with higher star-formation activity, younger stellar population and late-type morphologies over a wide redshift range. Addi-

tionally, [Mullaney et al. \(2012\)](#) and [Shimizu et al. \(2015\)](#) studied in detail the position of X-ray selected AGN on the $\text{SFR}-M_*$ diagram and found that AGN preferentially reside in galaxies in transition from the main-sequence of SFG to quiescent galaxies; instead galaxies with a higher level of SFR on and above the MS (i.e. starburst) have a smaller probability of hosting an AGN. In our work, we found that 239 AGN hosted by SFGs (75.4% of all AGN found in SFGs) are located below the MS, while only 78 AGN are above the MS (24.6%). The larger fraction of AGN in the transition region from SFGs to quiescent seem to support the scenario in which high-efficiency accreting AGN play a role in galaxy quenching.

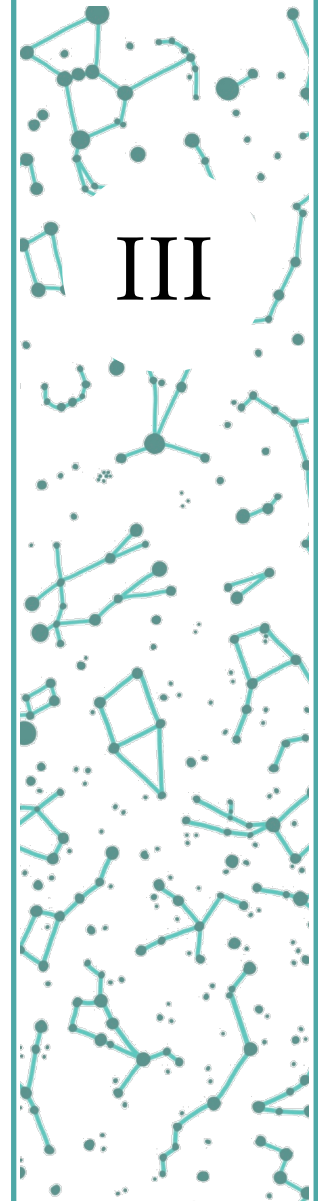
We point out that only 24.0% of all X-ray sources in our 3XMM-SDSS sample were classified as AGN according to X-ray criteria mentioned in Section 5.2. The analysis performed in Section 6.2 shows however that many galaxies that do not respect those criteria, present anyway an excess X-ray emission indicating that they likely host low luminosity AGN. In fact, the empirical AGN selection criteria identify AGN which dominate the host galaxy in some part of the electromagnetic spectrum, and therefore tend to miss sources with low luminosity and/or inefficient accretion. The numbers of AGN selected without/with X-ray luminosity correction are presented in Table 6.1. The combination of ‘classical’ and ‘low luminosity’ AGN reveal a similar tendency of AGN to be hosted by SFGs as was shown above for ‘classical’ AGN. The same result was obtained by several studies over a broad redshift range ([Mullaney et al. 2012](#), [Delvecchio et al. 2015](#), [Aird et al. 2018](#)) with the use of near- and far-IR and X-ray data corrected for star-formation processes in the host galaxies.

Finally, we can derive the fraction of galaxies hosting AGN, based on our 3XMM-SDSS sample. As mentioned in Section 4.5, 40 914 galaxies (20 462 star-forming and 20 452 quiescent) of our SDSS sample fall within the 3XMM footprint. Of these only 4% (1628 objects) have a residual X-ray emission after correcting for the host-galaxy emission, suggesting the presence of an AGN, and

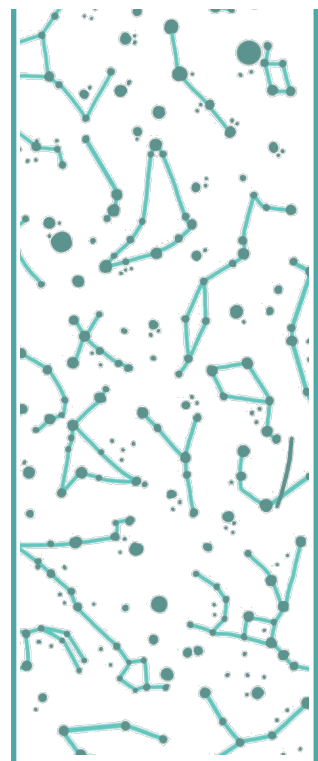
Table 6.1: Composition of the 3XMM-SDSS X-ray sample. The left columns ('X-ray sources') show the number of AGN and other sources selected according to the 'classical' X-ray criteria to SDSS sources detected in the 3XMM catalogue (Section 5.2); the right columns show the number of AGN in the 3XMM AGN sample of sources which could be corrected for the host-galaxy contribution, thus identifying also 'low luminosity' AGN. The percentages refer to the respective sample sizes.

	X-ray sources ($N = 1953$)				AGN after L_x correction ($N = 1628$)					
	'classical' AGN		other X-ray sources		'classical' AGN		'low luminosity' AGN		all AGN	
	N	%	N	%	N	%	N	%	N	%
All	469	24.0%	1484	76.0%	454	27.9%	1174	72.1%	–	–
Star-forming	317	16.2%	674	34.4%	317	19.5%	598	36.7%	915	56.2%
Quiescent	152	7.8%	810	41.5%	137	8.4%	576	35.4%	713	43.8%

only 469 (1%) of these are 'classical' AGN. Specifically 4.5% of star-forming galaxies in the local Universe host AGN (1.5% 'classical' AGN) and 3.5% of quiescent galaxies host AGN (0.7% 'classical' AGN).



The Black Hole accretion rate in the local Universe



7

The specific Black Hole accretion rate

A fundamental component of the standard AGN model is the accretion disk around the SMBH (see Section 3.4). The properties of the accretion disk can be defined by several parameters such as the SMBH mass and the accretion rate, the disk inclination etc. Reliable BH masses have been estimated for many nearby galaxies and for distant active galaxies using a broad variety of different techniques such as reverberation mapping methods, studies of the stellar dynamics in the nuclear region, the scaling relations etc (see Section 8.2).

The accretion rate plays an important role in shaping the AGN behaviour, the observational properties and evolution. The study of its variation with time, type of source and properties of the host galaxy can give insights into Black Hole accretion physics, constraining the models for the evolution of AGN properties and its effect on the host galaxy. The determination of the BH accretion rate requires the measurement of the intrinsic AGN emission (i.e. the AGN SED). However, the reconstruction of the SED is very difficult and affected by many factors such as dust obscuration, the emission of the host galaxy and also the limitation of our observing capabilities.

7.1 The sBHAR definition

In Section 3.4 we mentioned that the accretion rate of Black Hole can be derived in the form of the Eddington ratio, i.e. the ratio between AGN bolometric luminosity and the maximum possible Eddington luminosity. The latter one is defined from the equilibrium between the gravitational force acting inward and the radiation pressure acting outward onto the infalling material, i.e.

$$F_{rad} \leq F_{grav}:$$

$$\frac{\sigma_T L}{4\pi r^2 c} \leq \frac{G \mathcal{M}_{BH} m_p}{r^2}, \quad (7.1)$$

where the proton mass $m_p = 938.27 \text{ MeV} = 1.67 \cdot 10^{-27} \text{ kg}$ (we assume a neutral material on average), the Thompson cross-section $\sigma_T = 6.65 \cdot 10^{-29} \text{ m}^2$, the gravitational constant $G = 6.673 \cdot 10^{-11} \text{ m}^3 \text{ kg}^{-1} \text{ s}^{-2}$ and \mathcal{M}_{BH} is the mass of SMBH. Hence we can easily express the luminosity as:

$$\begin{aligned} L \leq \frac{4\pi c G \mathcal{M}_{BH} m_p}{\sigma_T} = L_{Edd} &\simeq 6.31 \cdot 10^4 \mathcal{M}_{BH} \text{ erg s}^{-1} \simeq \\ &\simeq 1.3 \cdot 10^{38} \left(\frac{\mathcal{M}_{BH}}{\mathcal{M}_{\odot}} \right) \text{ erg s}^{-1} \end{aligned} \quad (7.2)$$

Moreover, the luminosity produced by accretion onto a compact supermassive BH can be derived the accretion rate itself. We assume that the SMBH is accreting mass from its surroundings with a rate $\dot{m} = dm/dt$, and that a small fraction of the gravitational potential energy of the accreting material is transformed into radiation. This fraction can be expressed by the efficiency parameter η , which is equal to zero in the case of no emission and complete accretion of matter, and reaches unity when all the rest-mass energy is converted into the radiation. Thus, the luminosity radiated away can be expressed as $L = \eta \dot{m} c^2$. In case of a typical AGN the efficiency parameter is assumed to be $\eta \sim 0.1$ as the matter in the galaxy nucleus has a significant angular momentum, i.e. it can't fall directly into the SMBH and forms an accretion disk considering that most of the energy is released several gravitational radii away from the SBMH.

Hence, the accretion rate for AGN can be expressed as:

$$\dot{m} = \frac{L}{\eta c^2} \simeq 1.8 \cdot 10^{-3} \frac{L_{44}}{\eta} \mathcal{M}_{\odot} \text{ year}^{-1}, \quad (7.3)$$

At the same time, the luminosity produced by accretion can't exceed the Eddington luminosity, otherwise all material will be blown away by radiation pressure (i.e. a feedback process). Hence, the Eddington luminosity implies a limit on the steady accretion rate:

$$\dot{m}_{\text{Edd}} = \frac{L_{\text{Edd}}}{\eta c^2} \simeq 3 \mathcal{M}_8 \left(\frac{\eta}{0.1} \right)^{-1} \mathcal{M}_{\odot} \text{ year}^{-1} \simeq 2.2 \mathcal{M}_8 \mathcal{M}_{\odot} \text{ year}^{-1}, \quad (7.4)$$

where $\mathcal{M}_8 = \mathcal{M}_{\text{BH}}/10^8 \mathcal{M}_{\odot}$.

Since the bolometric luminosity (i.e. the total luminosity radiated by an object at all wavelengths) is the only quantity can be measured directly by observations, we can express the accretion rate in terms of the Eddington ratio $\lambda = \dot{m}/\dot{m}_{\text{Edd}}$, where the bolometric luminosity:

$$L_{\text{bol}} = \dot{m} \eta c^2 = \dot{m} \frac{L_{\text{Edd}}}{\dot{m}_{\text{Edd}}} = \left(\frac{\dot{m}}{\dot{m}_{\text{Edd}}} \right) 1.3 \cdot 10^{38} \frac{\mathcal{M}_{\text{BH}}}{\mathcal{M}_{\odot}} \text{ erg s}^{-1} \quad (7.5)$$

and therefore

$$\lambda_{\text{Edd}} = \frac{L_{\text{bol}}}{L_{\text{Edd}}}. \quad (7.6)$$

Since in present work we have only stellar masses \mathcal{M}_{\star} instead of \mathcal{M}_{BH} , we follow the definition from [Bongiorno et al. \(2012\)](#), [Georgakakis et al. \(2014\)](#), [Bongiorno et al. \(2016\)](#), [Aird et al. \(2018\)](#) and assume that the Black Hole mass scales with the host galaxy stellar mass as $\mathcal{M}_{\text{BH}} = 0.002 \mathcal{M}_{\star}/\mathcal{M}_{\odot}$ as in [Häring & Rix \(2004\)](#). This assumption is however ambiguous in some cases (its implications will be discussed further in Section 8.2), but it allows us to calculate the so-called specific Black Hole accretion rate (λ_{sBHAR}), the rate of accretion onto the central SMBH scaled relative to the stellar mass of the host galaxy:

$$\lambda_{\text{sBHAR}} = \frac{k_{\text{bol}} L_{\text{X,hard}}}{1.3 \cdot 10^{38} \times 0.002 \mathcal{M}_{\star}/\mathcal{M}_{\odot}}, \quad (7.7)$$

where k_{bol} is a bolometric correction factor for the hard band, $L_{\text{X,hard}}$ is the 2.0–12 keV X-ray luminosity. Although the bolometric correction factor is dependent on the luminosity ([Marconi et al. 2004](#), [Lusso et al. 2012](#), [Bongiorno](#)

et al. 2016), here we adopted an average bolometric correction of $k_{\text{bol}} = 25$ since the other systematics discussed below dominate the final uncertainty. The additional scale factors are defined from Equation 7.2 assuming $\lambda_{\text{sBHAR}} \approx \lambda_{\text{Edd}}$, where the Eddington ratio $\lambda_{\text{Edd}} \propto L_{\text{X}}/M_{\text{BH}}$.

7.2 The sBHAR distribution as a function of stellar mass

To study the BHAR in the local Universe we plot first the observed BHAR distribution for star-forming and quiescent galaxies. As the sensitivity of the X-ray observations covering our SDSS galaxy sample varies across the sky (due to different exposure time, off-axis angle, detector) we have to correct our 3XMM AGN sample for the fraction of missed sources as a function of flux. For this purpose, we used the count/flux upper limit service for XMM data, XMM FLIX¹ (Carrera et al., 2007). The 3XMM-DR8 catalogue includes the sources with EPIC detection likelihood $\text{DET_ML} > 6$ in the full band (0.2–12 keV); however a large number of these sources have a lower detection probability in hard band (2.0–12 keV) because of the AGN spectral shape coupled with the lower sensitivity of the *XMM-Newton* detectors at higher energies. Since FLIX service allows to calculate the detection limits only for the values of the likelihood detection higher than 6 (3σ), we were forced to reduce our final sample from 1628 objects to 570 objects choosing only those objects with the detection likelihood $\text{DET_ML} > 6$ in hard band (grey area in Figure 7.2 and 7.3). We then collected the values of the flux upper limit, which corresponds to a 3σ detection threshold of the 3XMM survey, at the position of each source in our optical sample falling in the 3XMM footprint and compiled the cumulative curves shown in Figure 7.1 which describe the likelihood of detecting the X-ray counterpart of our galaxies at each flux level. The cumulative curves were applied as statistical

¹<https://www.ledas.ac.uk/flix/flix.html>

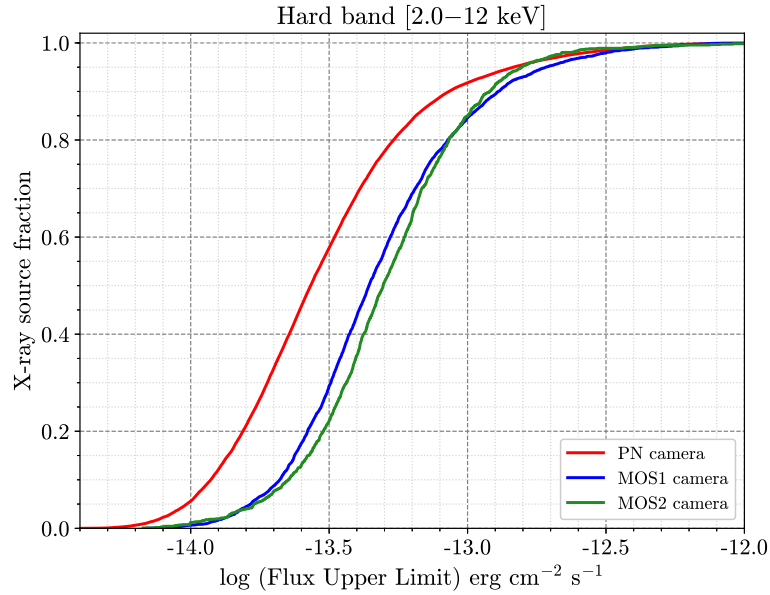


Figure 7.1: The cumulative histogram of flux upper-limit in hard band [2.0–12 keV] for XMM cameras from XMM FLIX service.

weights to scale the number of objects in BHAR distribution in Figure 7.2 and 7.3 to correct for the variable sensitivity across the sky.

The corrected λ_{sBHAR} distribution shows that ‘classical’ AGN have higher accretion rates ($\log \lambda_{\text{sBHAR}} \geq -3$) than the rest of the accreting SMBH population in all ranges of stellar masses. This result is in agreement with previous works (Mullaney et al. 2012, Chen et al. 2013, Mendez et al. 2013, Delvecchio et al. 2015, Stemo et al. 2020). Such limit on BHAR for X-ray selected ‘classical’ AGN can be caused by the fact that the selection criteria based on the X-ray flux/luminosity were calibrated to detect moderate and high luminosity AGN, and do not work properly for low-luminosity AGN.

The shape of the corrected λ_{sBHAR} distribution is approximately consistent with a power-law flattening at low accretion rates between $-3 \lesssim \log \lambda_{\text{sBHAR}} \lesssim -2$ for all stellar mass ranges. Star-forming galaxies have slightly higher values of sBHAR peaking at $\log \lambda_{\text{sBHAR}} \approx -3$ (Figure 7.2) than quiescent ones, peaking at $\log \lambda_{\text{sBHAR}} \approx -4$ (Figure 7.3). On the other hand, the λ_{sBHAR} distribution shows a lack of objects at high ($\log \lambda_{\text{sBHAR}} > -2$) BHAR due to the lack of bright SMBH accreting up to the Eddington limit usually found in AGN studies

based on flux-limited surveys extending to high redshifts. In fact, as discussed before, our initial sample was selected from optical galaxies with an estimate of the intrinsic SFR derived from the optical spectrum, and thus, by definition, non-AGN dominated systems; furthermore we are limited to low-redshift sources and thus the presence of bright AGN and quasars is suppressed by the strong evolution of the AGN luminosity function with cosmic time (we quantify this effect further in Section 8.4). Additionally, we should mention the possible presence of a selection bias due to the flux limit of SDSS, which translates in different stellar mass limits for star-forming and quiescent galaxies (Georgakakis et al., 2014). This results in a lack of quiescent galaxies at low redshift compared to SFGs of the same stellar mass. However, this bias affects galaxies only with stellar mass $\mathcal{M}_* \gtrsim 10^{10} M_\odot$. This bias will be taken into account in our future work.

7.3 The sBHAR and L_X correlation with stellar mass and SFR

To infer the dependence of AGN activity on galaxy properties, we divided our 3XMM AGN sample in bins of SFR and \mathcal{M}_* and calculated the median λ_{sBHAR} and L_X in each bin; we point out that negative values (after the correction for the host galaxy contamination) are included in the calculation to avoid biasing the result. The distribution of λ_{sBHAR} (and L_X) on the SFR– \mathcal{M}_* diagram is shown in Figure 7.4. The Figure shows that L_X increase with \mathcal{M}_* for both star-forming and quiescent galaxies. To verify the statistical significance of this trend we applied the one-way ANOVA analysis for L_X values in six stellar mass bins for star-forming and quiescent galaxies separately. As a result we found a significant statistical difference in L_X between these mass bins for star-forming (P value = 0.001) and quiescent galaxies (P value = 0.004). This trend is consistent with the results of Mullaney et al. (2012), Delvecchio et al. (2015), Stemo

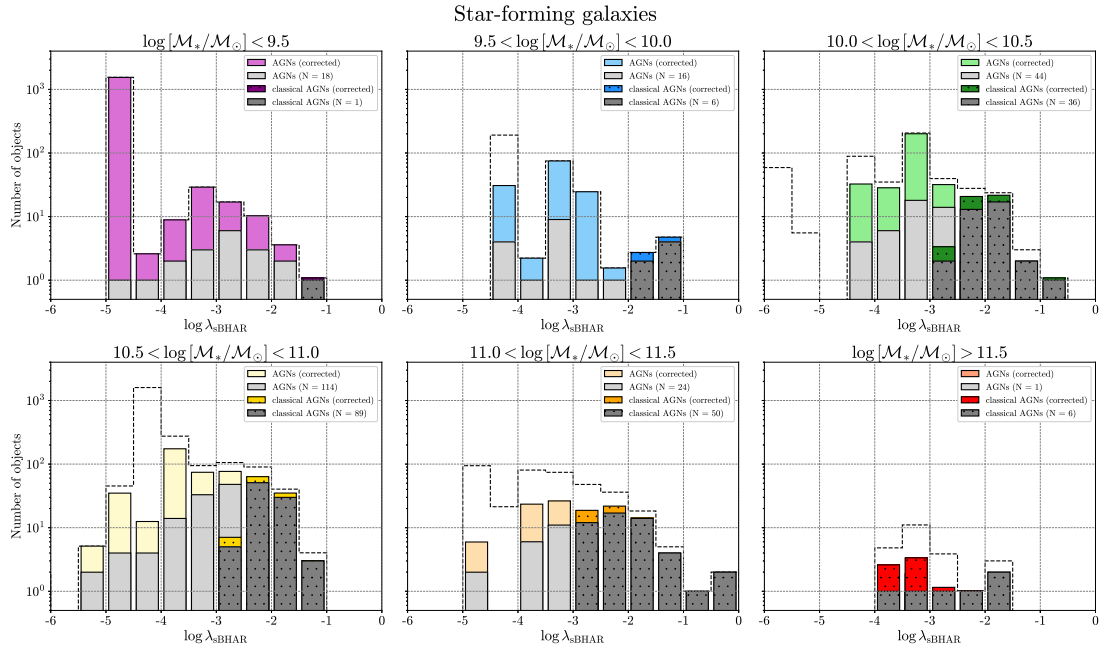


Figure 7.2: The distribution of the specific Black Hole accretion rate (sBHAR) for AGN in star-forming galaxies in six $\log[M_*/M_\odot]$ ranges. The ‘classical’ AGN (Section 5.2) shown by the dotted area and darker colour. The original data, before correcting for the 3XMM survey sensitivity, are shown by grey colours. The black dashed line represents the total distribution of sources in the 3XMM AGN sample without SF/quiescent galaxy separation.

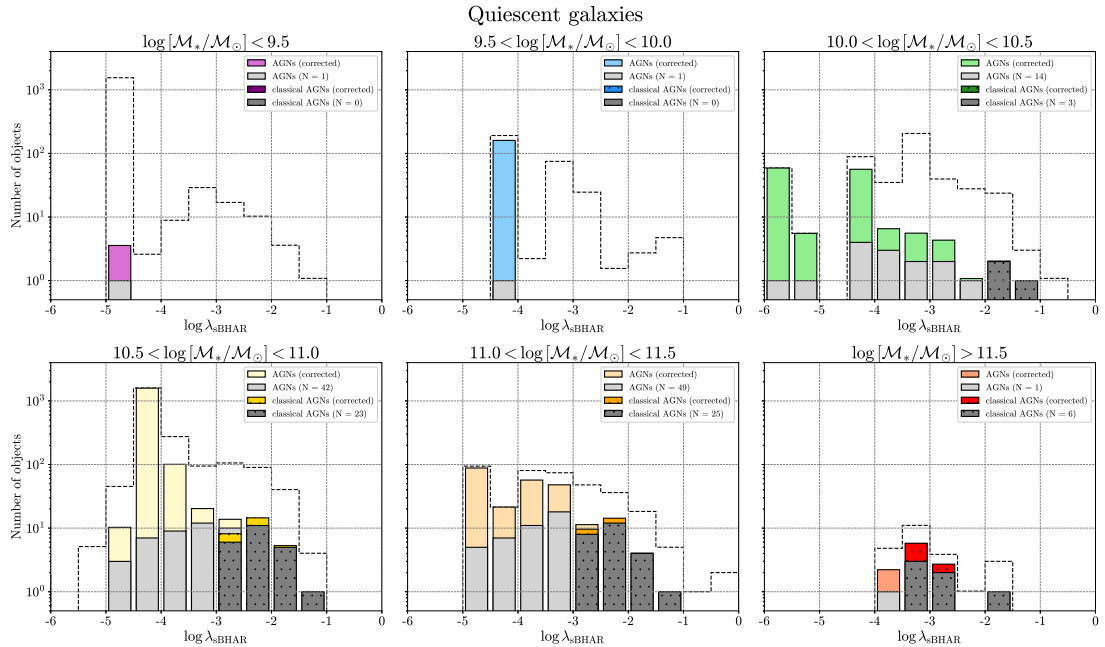


Figure 7.3: The same distribution of sBHAR as Figure 7.2 for quiescent galaxies.

[et al. \(2020\)](#) according to which high-mass galaxies have the tendency to host AGN with much higher X-ray luminosity than less massive (dwarf) galaxies. However, the presence of this correlation can also be caused by the selection effect, since massive galaxies contain more massive BH (i.e. more luminous AGN) than galaxies with lower stellar mass (i.e. less massive SMBH). To reduce the influence of this selection effect and reveal the underlying correlation with stellar mass we can analyse sBHAR instead of L_X as sBHAR is already normalised to stellar mass by definition (see Eq. 7.7). As a result, the bottom panel of Figure 7.4 shows that sBHAR for star-forming galaxies is increasing with stellar mass (P value = 0.008), but this trend is weaker compared to X-ray luminosity (see top panel of Figure 7.4). On the other hand, this trend is absent for quiescent galaxies and they show on average the same values of sBHAR for different stellar masses (P value = 0.351). Moreover, star-forming galaxies have systematically higher λ_{sBHAR} (and L_X respectively) at fixed \mathcal{M}_* than quiescent ones; on average the median λ_{sBHAR} for SFGs varies from -3.2 to -2.4 , while for quiescent galaxies from -4.2 to -3.5 . The same result was found for optical, IR and X-ray selected samples in [Rodighiero et al. \(2015\)](#), [Heinis et al. \(2016\)](#).

The correlation between $\langle \log \lambda_{\text{sBHAR}} \rangle$ and $\log \text{SFR}$ is presented separately for quiescent and star-forming galaxies in six stellar mass ranges in Figure 7.6. For each \mathcal{M}_* interval the mean $\langle \lambda_{\text{sBHAR}} \rangle$ was calculated in 10 bins of SFR in the range $-3.0 < \log \text{SFR} < 2.0$. The uncertainty of $\langle \lambda_{\text{sBHAR}} \rangle$ was computed using jackknife resampling. The Figure confirms the lower level of accretion rate for quiescent galaxies in 5 stellar mass ranges, while for the lowest stellar masses, we cannot verify the existence of the same trend due to presence of only two quiescent galaxies in this mass range (see left top panel in Figure 7.6). To evaluate the statistical significance of the BHAR-SFR correlation we applied a regression analysis and fitted our data using the least-squares approximation by linear function. The best-fit parameters are listed in Table 7.1: in particular the P -values confirm that sBHAR is correlated with SFR at $> 95\%$ confidence

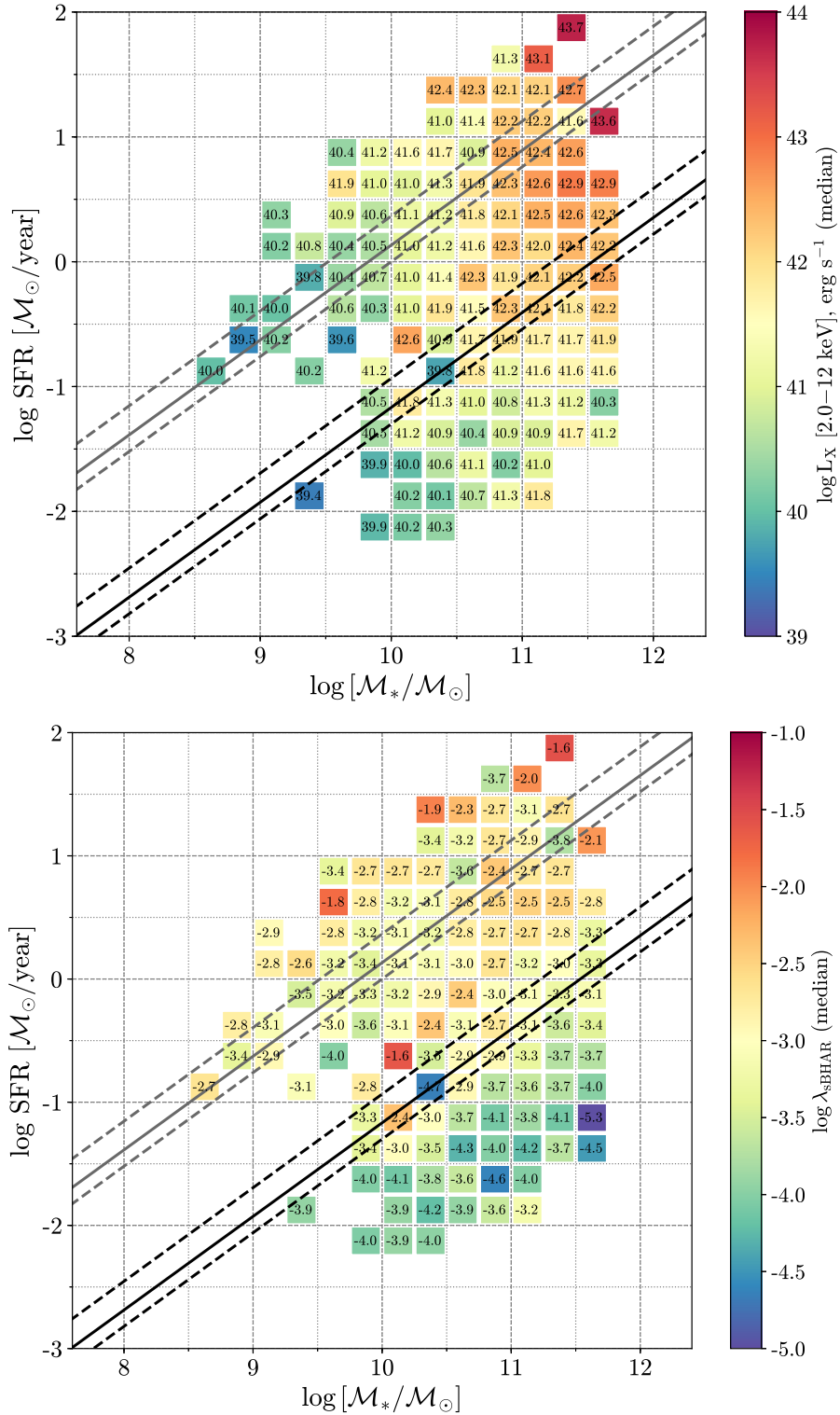


Figure 7.4: The distribution of X-ray luminosity (top) and the specific BH accretion rate λ_{sBHAR} (bottom) on SFR- M_* plane. The actual median value of λ_{sBHAR} (X-ray luminosity) for each bin of SFR and M_* is written inside the square. The black and grey lines are the same as in Figure 4.2. The number of points in both diagrams ranges from 76 in the central part to 2-3 in the edges (see Figure 7.5).

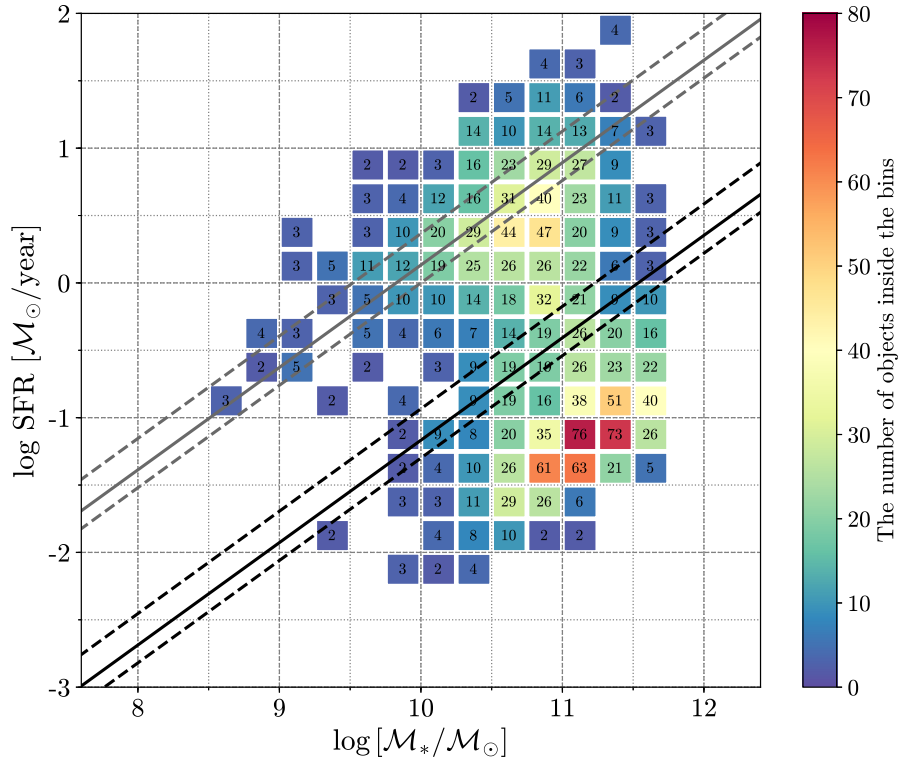


Figure 7.5: The number of points in each SFR and M_* bin for both diagram presented in Figure 7.4.

(P -value < 0.05) for all six stellar mass intervals. The best-fitting slope is close to the result found in [Delvecchio et al. 2014](#) ($\alpha = 0.54 \pm 0.27$) for the low redshift subsample ($0.01 < z < 0.25$), but is systematically flatter compared to high redshift samples in [Chen et al. 2013](#), [Delvecchio et al. 2015](#), [Aird et al. 2019](#) (see Figure 7.7). This would indicate that the $\langle \log \lambda_{\text{SBHAR}} \rangle$ -log SFR relation is not linear and flatter at low SFR than at high SFR. On the other hand, the high- z studies do not sample well the low-SFR regime and thus a definitive conclusion is not straightforward.

A number of studies suggest the existence of a connection between X-ray luminosity for star-forming galaxies and their location related to main sequence. For instance, [Masoura et al. \(2018\)](#) found that L_X increases with SFR for galaxies below the MS and decrease with SFR above MS, and suggested that this trend can be explained by the enhancing/quenching of star-formation processes by AGN depending on the position of the host galaxy in relation to MS. To verify the existence of this effect in our 3XMM AGN sample, we calculated the

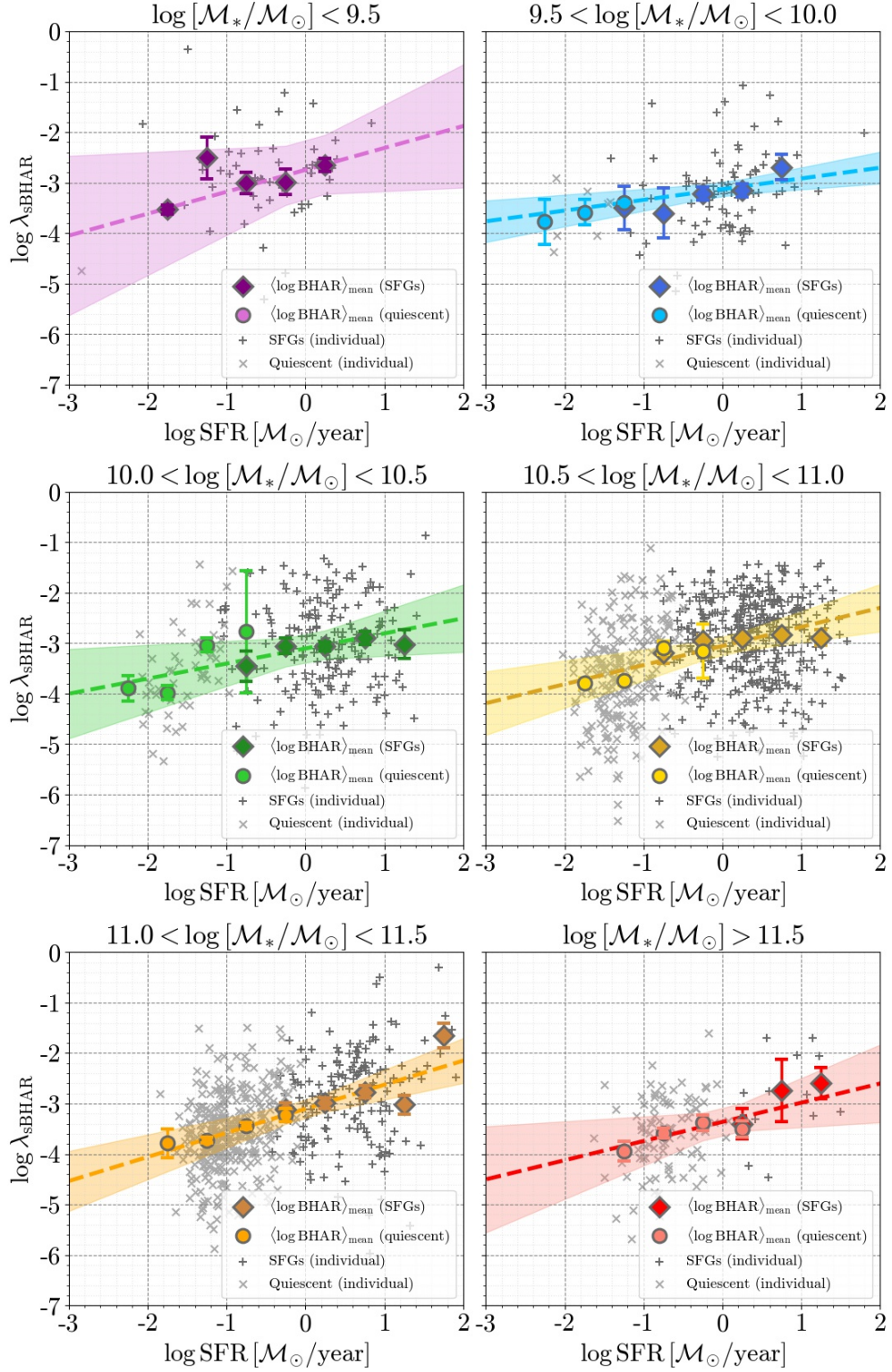


Figure 7.6: The jackknife mean value of $s\text{BHAR}$ vs SFR for star-forming (diamond) and quiescent galaxies (circles) for six stellar masses ranges. The individual objects from our 3XMM AGN sample represented by grey crosses (SFGs) and pluses (quiescent). The errorbars were calculated as a variance of the jackknife mean. The dashed line shows the least-square linear best-fit with 95% confidence interval. The best-fit and goodness-of-fit parameters are presented in Table 7.1.

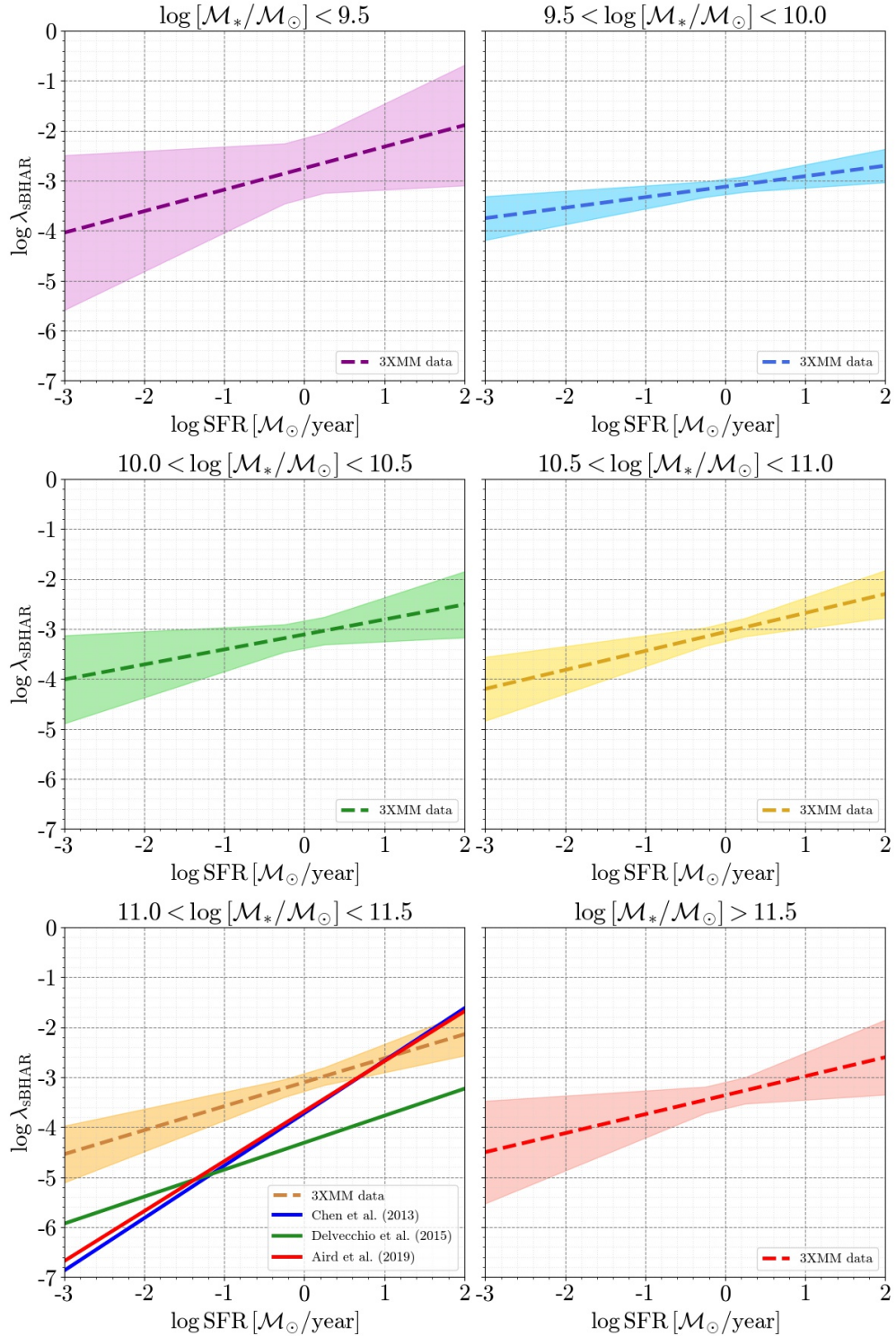


Figure 7.7: The least-square linear best-fit of sBHAR vs SFR correlation with 95% confidence interval in six stellar masses ranges for 3XMM AGN sample. The best-fit and goodness-of-fit parameters are presented in Tables 7.1. The best-fits of sBHAR-SFR correlation from works of [Chen et al. \(2013\)](#), [Delvecchio et al. \(2015\)](#) and [Aird et al. \(2019\)](#) are presented by solid blue, green and red lines, respectively.

normalised SFR as the ratio of the SFR of each galaxy to the SFR of the main-sequence at the same mass. For each interval of the normalised SFR the mean L_X and its uncertainty were calculated using jackknife resampling in 6 bins of $\log[\text{SFR}/\text{SFR}_{\text{MS}}]$ and presented on left panel of Figure 7.8. At first sight it looks like the effect is confirmed, as we observe an average lower L_X at larger (normalised) SFR that is qualitatively consistent with the result obtained by [Masoura et al. \(2018\)](#). However, analysing the L_X -SFR relation separately for six stellar mass bins (right panel of Figure 7.8) it seems that this effect is mainly due to the fact that at lower \mathcal{M}_* we have only SFGs with typically lower L_X than at higher stellar mass, and thus could be driven by the incompleteness effects. Furthermore no evidence of this effect is observed for ‘classical’ AGN, (see left panel of Figure 7.8) in agreement with the studies of [Rovilos et al. \(2012\)](#), [Shimizu et al. \(2015\)](#) for low-redshift samples.

Table 7.1: The best-fit parameters obtained from a linear relation between $\langle \log \lambda_{\text{sBHAR}} \rangle$ and $\log \text{SFR}$ for six stellar mass ranges for the 3XMM-SDSS sample (see Figure 7.6). The slope, intercept with their standard errors and all statistics parameters (F -statistic, P value and R^2) were found from the least-square linear regression. In this work, we consider the confident level as P -value < 0.05 . N is the number of points in each stellar mass bin.

#	Stellar mass range	slope	intercept	F -statistic	P value (F -stat)	R^2	N
1	$\log [M_*/M_\odot] < 9.5$	0.43 ± 0.08	-2.75 ± 0.12	26.66	0.0141	0.899	5
2	$9.5 < \log [M_*/M_\odot] < 10.0$	0.21 ± 0.04	-3.12 ± 0.05	31.56	0.0014	0.840	8
3	$10.0 < \log [M_*/M_\odot] < 10.5$	0.30 ± 0.09	-3.11 ± 0.09	11.09	0.0126	0.613	9
4	$10.5 < \log [M_*/M_\odot] < 11.0$	0.38 ± 0.07	-3.06 ± 0.06	30.90	0.0009	0.815	9
5	$11.0 < \log [M_*/M_\odot] < 11.5$	0.48 ± 0.06	-3.10 ± 0.06	56.49	0.0001	0.890	9
6	$\log [M_*/M_\odot] > 11.5$	0.38 ± 0.10	-3.36 ± 0.07	13.92	0.0136	0.736	7

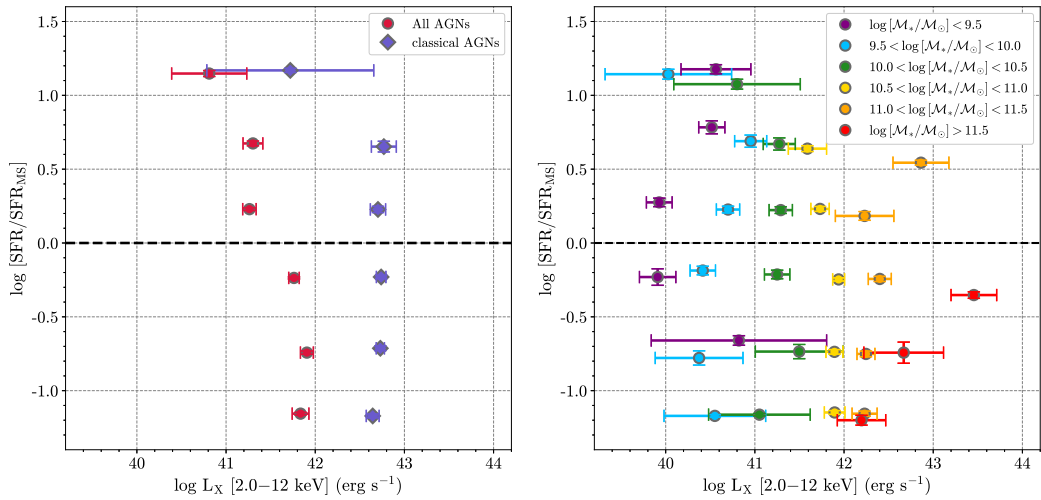


Figure 7.8: Left: The normalised SFR as a function of the mean L_X obtained by the jackknife resampling in $\log[\text{SFG}/\text{SFR}_{\text{MS}}]$ bins for SFGs in 3XMM AGN sample (circles) and for ‘classical’ AGN selected by X -ray criteria in Section 5.2 (diamonds). Right: The normalised SFR as a function of the mean L_X obtained by the jackknife resampling in $\log[\text{SFG}/\text{SFR}_{\text{MS}}]$ bins for SFGs in 3XMM AGN sample for six stellar mass bins. The errorbars were calculated as a variance of the jackknife mean. The dashed line is the position of the main sequence of star-forming galaxies (see definition in the text).

8 Sources of uncertainty in the sBHAR determination

The results discussed in the previous Sections are affected by various factors and assumptions. To evaluate these effects on the sBHAR determination and the SFR–BHAR relation, we made several tests which are presented below.

8.1 The reliability of SFR and \mathcal{M}_*

In order to test the reliability of our results we investigated the accuracy of our optical star-formation rates comparing them with those derived using different measurement methods. An analysis of the accuracy of SFR measurements based on $H\alpha$ and D4000 from the *galSpec* catalogue are presented by [Popesso et al. \(2019\)](#). According to their work the values of SFR from $H\alpha$ in *galSpec* are in the good agreement with SFR obtained from far-IR luminosity from *Wide-field Infrared Survey Explorer (WISE)* ([Salim et al., 2016](#)) and *Herschel* ([Elbaz et al., 2011](#)). However, the D4000-based SFR (which, we recall, was used by [Brinchmann et al. 2004](#) when line-based measurements were not possible, i.e. mainly for quiescent galaxies) reveals a systematic underestimate with respect to L_{IR} -based SFR and an overestimate at low SFRs ($< 0.01\mathcal{M}_{\odot}\text{yr}^{-1}$) compared

to SED-fitting measurements (Salim et al., 2016). A correction to D4000-based SFR in *galSpec* was proposed by Oemler et al. (2017) as a calibration parameter derived from UV+IR estimates with a correction based on the galaxy inclination and the NUV–g rest-frame colour (GALEX–SDSS filters). The combination of UV and IR bands was chosen in order to reproduce the fraction of galaxy radiation lost in optical band, e.g. the ionising UV emission from hot stars and mid-IR due to radiation absorbed by dust.

We calculated a corrected estimate of SFR for our 3XMM AGN sample using the relation $\log(\text{sSFR})_{\text{corr}} = 1.07 \cdot \log(\text{sSFR})_{\text{our}} + 0.64$ derived by Oemler et al. (2017), where sSFR is the so-called specific star-formation rate defined as $\log(\text{sSFR}) = \log(\text{SFR}) - \log \mathcal{M}_*$. A comparison of the uncorrected and corrected SFR for our 3XMM AGN sample is presented in Figure 8.1 (left panel) and the effect of the SFR correction on the SFR– \mathcal{M}_* diagram is shown in the right panel of Figure 8.1. It is clear that the SFR correction becomes significant only at the lowest SFRs, i.e. for quiescent galaxies with $\text{SFR} < 0.01 \mathcal{M}_\odot \text{yr}^{-1}$ (with a maximum difference of the $(\log(\text{SFR})_{\text{uncorr}} - \log(\text{SFR})_{\text{corr}}) \sim 0.3$) as was claimed also by Oemler et al. (2017), Popesso et al. (2019). In our work, we used the SFR in two cases: as tracer of the X-ray emission from X-ray binaries in star-forming galaxies (see Section 6.2) and in evaluating the correlation between SFR and Black Hole accretion rate (BHAR, Section 7.3). The maximum SFR correction $\Delta \text{SFR} = 0.15$ derived for SFGs in our 3XMM AGN sample does not change significantly the X-ray luminosity correction in Section 6.2 ($\Delta L_{\text{XBs}} = 1.41 \text{ erg s}^{-1}$) and therefore it does not affect significantly the BHAR calculation. The SFR– λ_{sBHAR} can change due to the SFR correction for the most massive quiescent galaxies ($\mathcal{M}_* > 10^{11.5} \mathcal{M}_\odot$), but we have a small fraction of such object in our sample and therefore it does not change our final results either.

To evaluate the accuracy of the stellar masses derived by Brinchmann et al. (2004) we used the catalogue of bulge, disk and total stellar masses for SDSS DR7 from Mendel et al. (2014). These masses were estimated from SED fitting

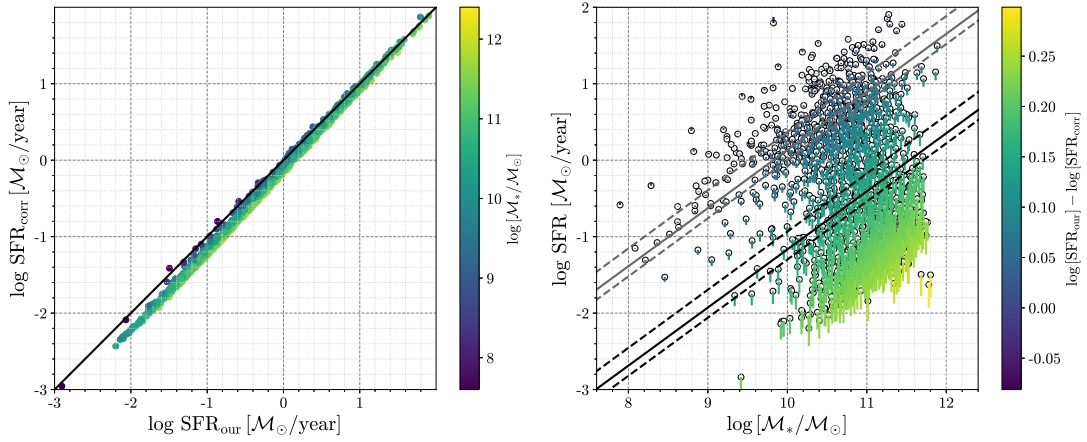


Figure 8.1: Left: The ratio of SFR for our 3XMM AGN sample calculated by [Brinchmann et al. \(2004\)](#) and SFR corrected according to the criteria proposed by [Oemler et al. \(2017\)](#). The colour shows the $\log[M_*/M_\odot]$ range in our sample. The 1:1 line is represented by black solid line. Right: The distribution of star-formation rate vs. stellar mass for our 3XMM AGN sample (black circles). The value of SFR correction is represented by colour. The black and grey lines are the same as in Figure 4.2.

in u,g,r,i,z SDSS bands similar to the mass estimate described in [Kauffmann et al. \(2003\)](#), but with significant differences in the stellar population synthesis (SPS) model grid. In fact [Mendel et al. \(2014\)](#) excluded bursty star-forming histories from their SPS model grid considering their rarity in the local Universe ($<10\%$) and the difficulty to identify them only by photometric data. In total we thus found counterparts for 1362 galaxies (83.3% of our 3XMM AGN sample) in the [Mendel et al. \(2014\)](#) catalogue.

The comparison between the stellar masses used in our work and those derived by [Mendel et al. \(2014\)](#) in the left panel of Figure 8.2 shows that M_* and $M_{*,\text{Mendel}}$ are generally consistent for all objects in our 3XMM AGN sample. However, galaxies with extreme SFR tend to have systematically lower values of $M_{*,\text{Mendel}}$ stellar masses compared to those used in this work. The same difference is also visible in the SFR– M_* diagram (right panel of Figure 8.2) and it is most likely caused by the excluding of bursty star-forming galaxies from SPS model grid used by [Mendel et al. \(2014\)](#). The accuracy of stellar mass determination affects the X-ray correction for SFGs (see Equation 6.2 in Section 6.2) and BHAR determination (Section 6.3) as $\lambda_{\text{sBHAR}} \propto M_*^{-1}$. We calculated λ_{sBHAR}

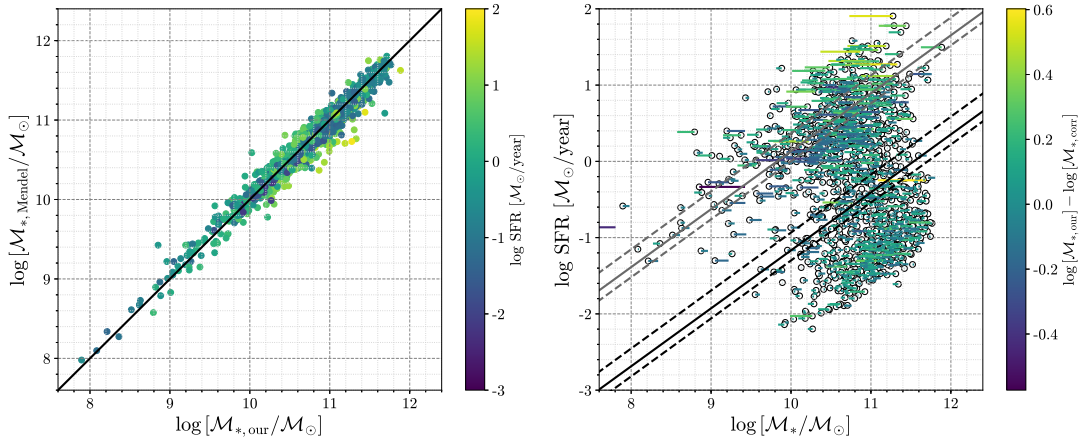


Figure 8.2: *Left:* The stellar mass for our 3XMM AGN sample calculated by [Brinchmann et al. \(2004\)](#) vs. the stellar mass computed by [Mendel et al. \(2014\)](#). The colour shows the distribution of $\log \text{SFR}$ in our sample. The 1:1 line is represented by black solid line. *Right:* The distribution of star-formation rate vs. stellar mass for our 3XMM AGN sample (black circles). The value of $\log [M_{*,\text{our}}] - \log [M_{*,\text{Mendel}}]$ is represented by colour. The black and grey lines are the same as in [Figure 4.2](#).

using the stellar mass from [Mendel et al. \(2014\)](#) catalogue and compared the obtained sBHAR with that one obtained in [Section 6.3](#). To evaluate the change of sBHAR calculated on the basis of different stellar mass we calculated the relative change in percentage unit. The sBHAR relative change distribution on $\text{SFR}-M_*$ plane in [Figure 8.3](#) shows only 105 objects significantly changed sBHAR and their absolute values of relative change are more than 50%. At the same time, these objects are located predominantly above MS of SFGs where it was discussed above such high number of changes can be caused by the underestimation of stellar mass for starburst galaxies in [Mendel et al. \(2014\)](#) catalogue.

According to all findings discussed in this section we decided not to use any correction for SFR and stellar mass as the existent uncertainties of SFR and stellar mass have insignificant effect on our final results.

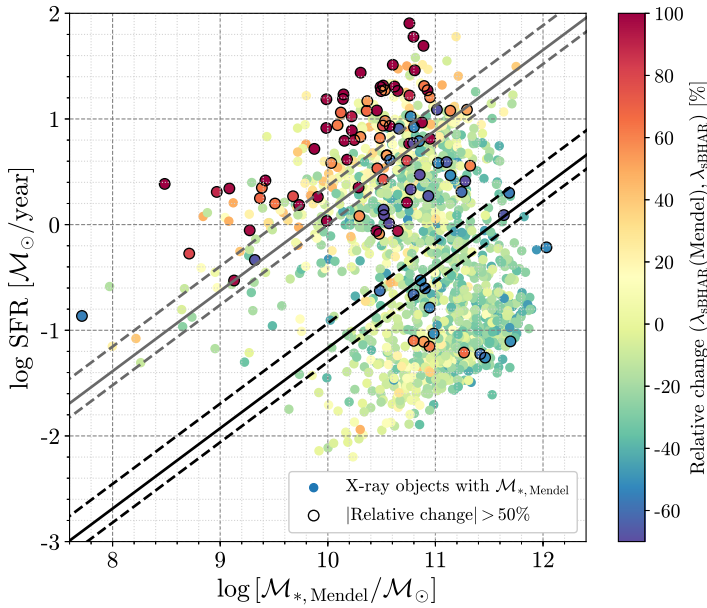


Figure 8.3: The distribution of star-formation rate vs. stellar mass from Mendel catalogue for 1362 X-ray objects. The colour gradient shows the relative percentage change between sBHAR calculated on the basis of stellar mass from our SDSS sample and stellar mass from Mendel catalogue. Black circles represent the objects with the absolute value of relative change more than 50%.

8.2 The relation between bulge, total stellar and supermassive BH masses

The masses of supermassive Black Holes in the local Universe can be measured with high accuracy using direct methods based on the kinematics of gas and stars around SMBH (Shen et al. 2011, Kormendy & Ho 2013). However, these direct techniques require long observations of individual galaxies thus making such mass determination for large number of objects a challenging effort. Also, the accuracy of such method depends on the spectral resolution, on the orientation and geometry of broad-line region, on obscuration etc (Merloni et al. 2010, Shen et al. 2011, Reines & Volonteri 2015). To estimate the SMBH masses for larger samples and over wide redshift ranges the usual approach consists in using indirect methods where the SMBH mass is inferred from observable host-galaxy properties that correlate with the Black Hole mass (i.e scaling relation). For instance, several studies showed that the mass of supermassive Black Hole correlates with the velocity dispersion of stars in the galaxy bulge (Ferrarese & Merritt, 2000, Gültekin et al., 2009), the bulge luminosity and mass (Häring & Rix, 2004, Kormendy & Ho, 2013, McConnell & Ma, 2013) and the total stellar

mass of the host galaxy (Reines & Volonteri 2015, Shankar et al. 2017, 2020).

The knowledge of the host galaxy parameters allows us to use scaling relations as an additional indirect method for BH mass determination, but the accuracy of SMBH mass derived by such method is dependent on the uncertainties and biases of the underlying scaling relations. In fact the assumption that SMBH mass correlates with the total stellar mass of the host galaxies has a key role in the specific BH accretion rate (λ_{SMBHAR}) calculation in Section 6.3, but the reliability of such assumption is controversial in some cases. Reines & Volonteri (2015) showed that the BH-to-stellar mass relation for nearby galaxies varies greatly depending on morphological type and AGN activity. Local AGN host-galaxies with SMBH masses measured by reverberation mapping or virial methods show significantly lower values than quiescent galaxies with masses determined by dynamical methods. It was suggested that such difference in BH-to-stellar mass relation is caused by the host galaxy properties. For instance, the most local AGN tend to be located in late-type spiral galaxies with pseudobulges, while the early-type elliptical galaxies (i.e. spheroids or classical bulges) mainly host inactive BHs and have a tendency to follow the canonical BH-to-bulge mass relation (Häring & Rix, 2004, Kormendy & Ho, 2013, McConnell & Ma, 2013). The same result was obtained by Shankar et al. (2016, 2017) for the sample of early and late-type galaxies with dynamical BH mass estimates derived by Savorgnan et al. (2016). Furthermore, the BH-to-stellar mass relation can be systematically biased by spatial resolution limits of current instruments or other observational effects (Shankar et al., 2020). In this case, the gravitational sphere of influence of SMBH cannot be resolved and hence the dynamical estimation of SMBH mass is inaccurate and distorts the scaling relations.

Using the bulge masses from Mendel et al. (2014) we calculated SMBH mass for our 3XMM AGN sample applying the BH-to-bulge mass relation by Mc-

Connell & Ma (2013):

$$\log\left(\frac{\mathcal{M}_{\text{BH}}}{\mathcal{M}_{\odot}}\right) = (8.46 \pm 0.08) + (1.05 \pm 0.11) \cdot \log\left(\frac{\mathcal{M}_{\text{Bulge}}}{10^{11} \mathcal{M}_{\odot}}\right) \quad (8.1)$$

The comparison of the obtained BH mass with \mathcal{M}_{*} in Figure 8.4 (top panel) shows that \mathcal{M}_{BH} scales with stellar mass by coefficient close to 0.002 for all quiescent galaxies of our sample, while the fraction of star-forming galaxies shows significantly wider distribution. This effect can be caused by the fact that BH-to-bulge mass relations were estimated with high accuracy only for elliptical galaxies (i.e. the bulge mass is equivalent to the total stellar galaxy mass) and for S/S0 galaxies with classical bulges, while for spiral galaxies with pseudobulges the existence of this relation is not clear. At the same time, the bulge masses in Mendel et al. (2014) were derived on the basis of the decomposition into bulge and disk components, whose accuracy depends on the spatial resolution and the signal-to-noise of the data and therefore may lead to high level of uncertainty in the bulge mass for some spiral galaxies. In addition, in Figure 8.4 we overplotted lines obtained by Shankar et al. (2016, 2020), which show the biased and unbiased empirical BH-to-stellar mass relations.

The results presented in Figure 8.4 together with the result of Reines & Volonteri (2015) indicates that the BH-to-stellar mass relation is the consequence of the existence of the underlying BH-to-bulge relation, i.e it does not work properly for spiral (i.e star-forming) galaxies with less prominent bulges. This fact can lead to inaccurate estimates of the BH mass for such star-forming galaxies which causes the underestimation of the BHAR (for 1 dex in average). To obtain the reliable BHAR for these galaxies it is necessary to estimate the BH mass using more accurate methods (e.g. stellar dynamics or reverberation mapping). Since such BH mass estimates are not available for our sample, we left the final results without applying a correction for this effect. Moreover, the fraction of galaxies with less prominent bulges is low compared to the total number of objects in our sample and hence, their effect on our results will be minimal.

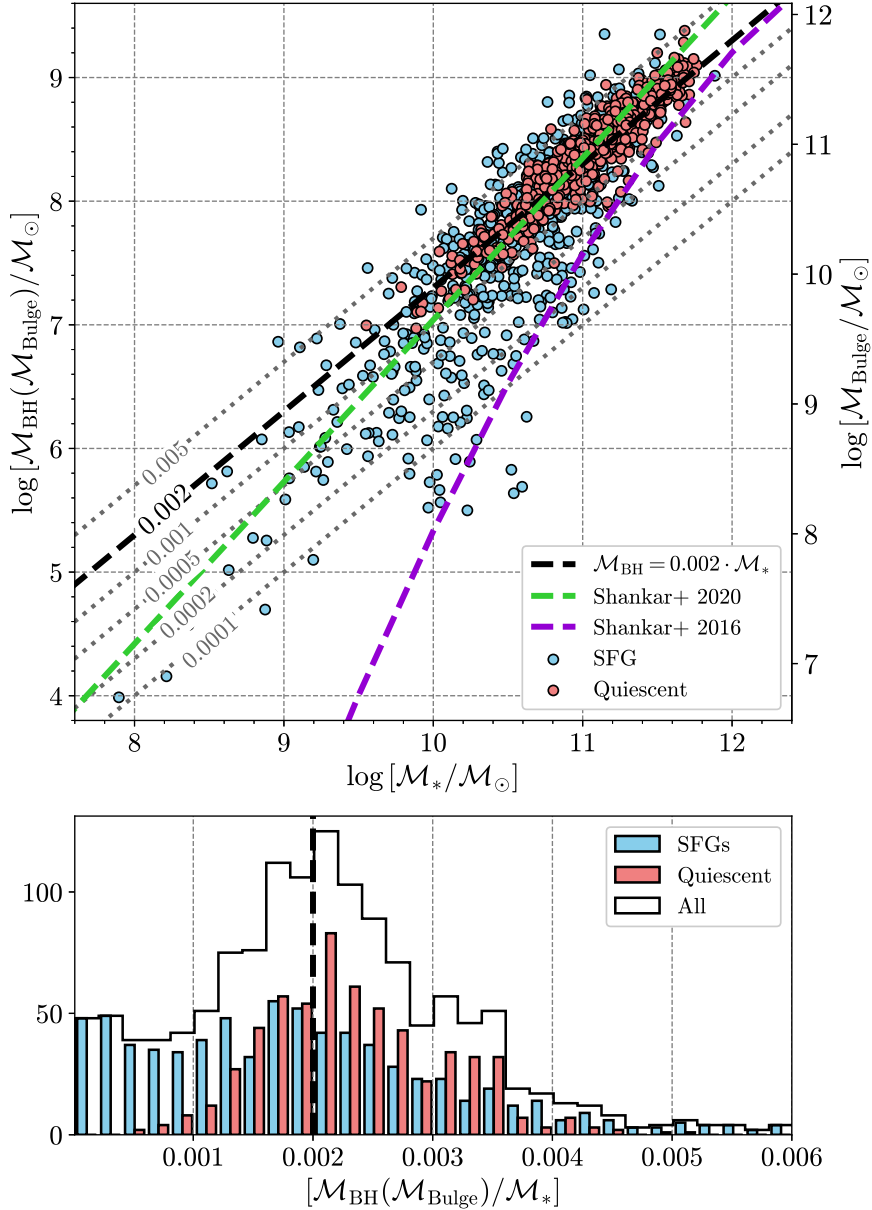


Figure 8.4: Top: The BH-to-stellar mass diagram for star-forming and quiescent galaxies in our 3XMM AGN sample. The SMBH mass is calculated due to the canonical BH-to-bulge relation derived by [McConnell & Ma \(2013\)](#) using the bulge mass from [Mendel et al. \(2014\)](#). The black dashed line show the mass scaling relation $\mathcal{M}_{\text{BH}} = 0.002 \cdot \mathcal{M}_*$ used in λ_{sBHAR} determination in Section 6.3. The grey dotted lines are correspond to the BH-to-stellar mass relation with a scaling coefficient in range from 0.0001 to 0.005. The green dashed line corresponds to the BH-to-stellar scaling relation from [Shankar et al. \(2020\)](#), which is obtained from the sample with reliable dynamically-measured \mathcal{M}_{BH} in the centre of local quiescent galaxies. The violet dashed line is represent the intrinsic or unbiased BH-to-stellar mass correlation from [Shankar et al. \(2016\)](#) obtained by a series of the Monte Carlo simulations to correct the bias effect due to the observation limits. Bottom: The histogram represents the distribution of the scaling coefficient calculated as BH-to-stellar mass ratio for star-forming (blue colour) and quiescent galaxies (red colour). The black histogram shows the same distribution for all galaxies in the sample.

8.3 The extended X-ray sources and their effect on the sBHAR-SFR connection

In Section 4.5 we selected the X-ray sources with zero extension parameter to avoid spatially extended objects, i.e. individual galaxies whose X-ray emission may be dominated by hot gas and LMXBs. The fraction of the extended objects may also be galaxy groups and clusters, whose angular size is smaller than the angular resolution of the *XMM-Newton* telescope (see Section 4.4) and hence, individual galaxies in these groups/clusters can not be resolved separately. However, our primary SDSS sample also contains sources at low redshift there is a probability to have a small fraction of nearby objects with resolved X-ray cores (i.e. non-zero extension) which harbour a faint accreting SMBH. The rejection of such objects affects the completeness of our 3XMM AGN sample and may lead to an underestimation of the median BHAR. To evaluate this effect we expanded the analysis to extended sources as well. For this purpose, we use the 334 objects with non-zero extension parameter, which were rejected from our XMM-SDSS sample in Section 4.5. Following the same steps as for non-extended sources we rejected all objects with detection flag $\text{SUM_FLAG} \geq 3$ and for sources with multiple observations we selected only the one with the highest exposure time. As a result, we found 182 extended objects. Their distribution of extended sources on the $\text{SFR}-\mathcal{M}_*$ diagram (Figure 8.5) shows that nearly 85% of such objects are located in massive quiescent galaxies ($\geq 10^{11} \mathcal{M}_\odot$) and 45% of these sources have $L_{\text{X,int}} \geq 3 \cdot 10^{42} \text{ erg s}^{-1}$.

We also made the visual inspection of SDSS images and spectra for these objects and found that 50% of extended sources are represented by isolated elliptical galaxies, while other 45% are located relatively close to other galaxies (possibly a galaxy group or cluster) and probably are central dominant (cD) galaxies. Some galaxies also have a nearby galaxy or a point-like source (likely an AGN/quasar) which can contribute to the detected X-ray emission. The large

X-ray luminosity ($L_{X,\text{int}} \geq 3 \cdot 10^{42} \text{ erg s}^{-1}$) of some extended sources could suggest the presence of an AGN contributing to the total X-ray emission. However, according to the optical images half of these objects are located in galaxy clusters and could thus also be explained by emission from the hot intra-cluster medium. Only 8 sources in our extended sample are located in the star-forming galaxy region (Figure 8.5) they are all low-redshift ($z < 0.05$) spiral galaxies with large angular diameter.

To subtract the fraction of X-ray emission from host galaxy we applied the same X-ray luminosity correction described in Section 6.2 and found 159 objects with positive residual X-ray luminosity. We calculated the sBHAR for these objects using Equation 7.7 and combined them with our 3XMM AGN sample. The distribution of the median λ_{sBHAR} on the SFR- \mathcal{M}_* plane for the combined (extended and point-like) dataset (see Figure 8.6) shows that the inclusion of extended sources to our 3XMM AGN sample leads to an increase of λ_{sBHAR} for massive/quiescent galaxies compared to the result presented in Figure 7.4 (right panel). However the overall increase not significant, and varies from 1.2% for $\log[\mathcal{M}_*/\mathcal{M}_\odot] = 11.0$ to 2.1% at $\log[\mathcal{M}_*/\mathcal{M}_\odot] = 11.5$.

In conclusion, we decided to exclude extended objects from our main study to avoid overestimating the average accretion rate since for such objects the correction to the total X-ray luminosity due to the hot gas contribution (see Section 5.2) is likely underestimated.

8.4 AGN-dominated sources in the local Universe and their effect on the sBHAR distribution

In Section 7.1 it was mentioned that the λ_{sBHAR} distribution in Figure 7.2 and 7.3 shows a lack of objects at high BHAR ($\log \lambda_{\text{sBHAR}} > -2$). Since we work with low-redshift sources the presence of bright AGN and quasars is suppressed by the strong evolution of the AGN luminosity function with cosmic time. How-

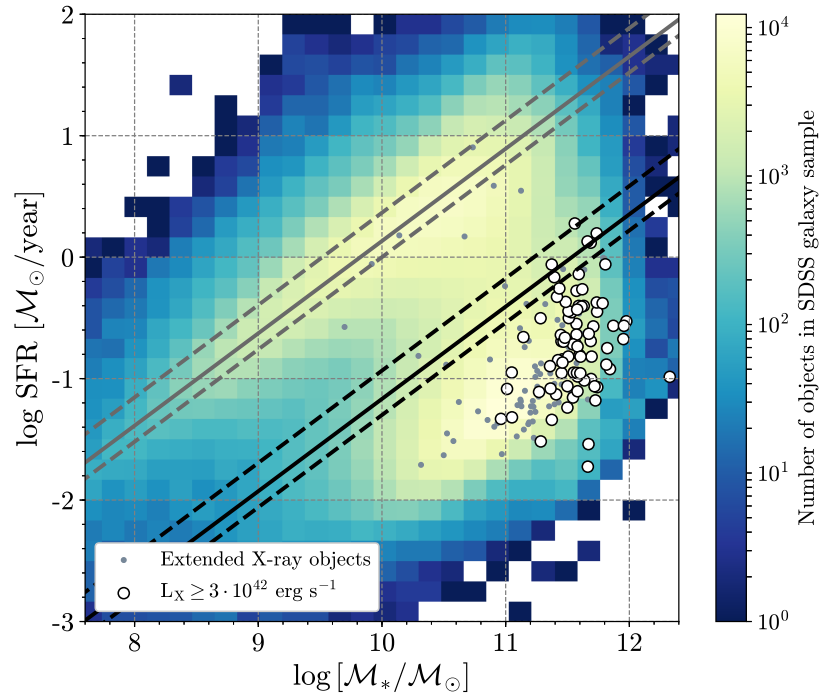


Figure 8.5: The distribution of star-formation rate vs. stellar mass for extended X-ray sources (grey circles). The blue to yellow colorscale reflects the 2D density distribution of galaxies in our optical SDSS sample. Black circles represent the AGN selected by the X-ray luminosity criterion $L_X \geq 3 \cdot 10^{42} \text{ erg s}^{-1}$. The black and grey lines are the same as in Figure 4.2.

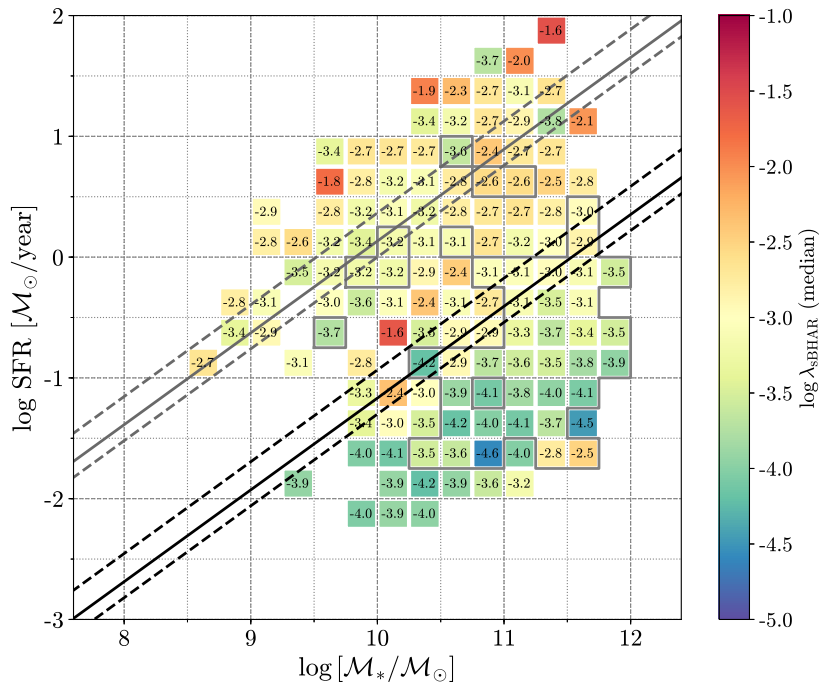


Figure 8.6: The distribution of the specific BH accretion rate (λ_{sBHAR}) for the combined sample of extended and non-extended X-ray sources. The SFR– M_* bins with some contribution from extended sources are encompassed by a grey solid line area. The black and grey lines are the same as in Figure 4.2.

ever, the fact that our primary sample was selected from optical galaxies with an estimate of the intrinsic SFR derived from the optical spectra, and thus, by definition, non-AGN dominated systems certainly introduces a bias toward low-luminosity systems.

To check this hypothesis we decided to compile a sample of type 1 AGN and quasars from SDSS DR8. Using the online service `CasJobs` SDSS Sky-Server we selected 12 789 objects within redshift range $z < 0.33$, which have reliable spectroscopic parameters (`RELIABLE != 0`) and redshift (`zWarning = 0`) and were classified as quasars. However, only 830 objects fall into the 3XMM footprint and were observed by *XMM-Newton*. This sample was cross-matched with 3XMM-DR8 following the same steps described in Section 4.5. As a result, we found 538 quasars with X-ray counterparts in the hard band (2.0–12 keV).

For each quasar we calculated the X-ray luminosity in the hard band (2.0–12 keV) in the same way described in Section 6.1. Since quasars are powerful type 1 AGN with bright nuclear emission which is dominated under the host galaxy emission, we do not need to apply the correction to their X-ray luminosity, i.e. the fraction of X-ray from star-formation is negligible comparing to X-ray from quasar. Since the determination of stellar mass for these objects is complicated due to strong contamination of the host galaxy by the emission of bright nuclei, we calculate the specific BHAR from Equation 7.7 assuming $\log[\mathcal{M}_*/\mathcal{M}_\odot] = 10.7$ for each quasar, which is corresponding the BH mass $\mathcal{M}_{\text{BH}} = 10^8 \mathcal{M}_\odot$ according the BH-to-stellar mass relation discussed in Section 8.2. The distribution of 538 quasars and our 570 classical and low-luminosity AGN with EPIC detection likelihood `DET_ML > 6` in the hard band (the description of this AGN sample is in Section 7.2) is shown in Figure 8.7.

We plotted the BHAR distribution for quasars in Figure 8.8 in combination with the BHAR distribution for our X-ray sample from Figure 7.2 and 7.3. In this case, it is not possible to separate the sample by stellar mass bins or galaxy

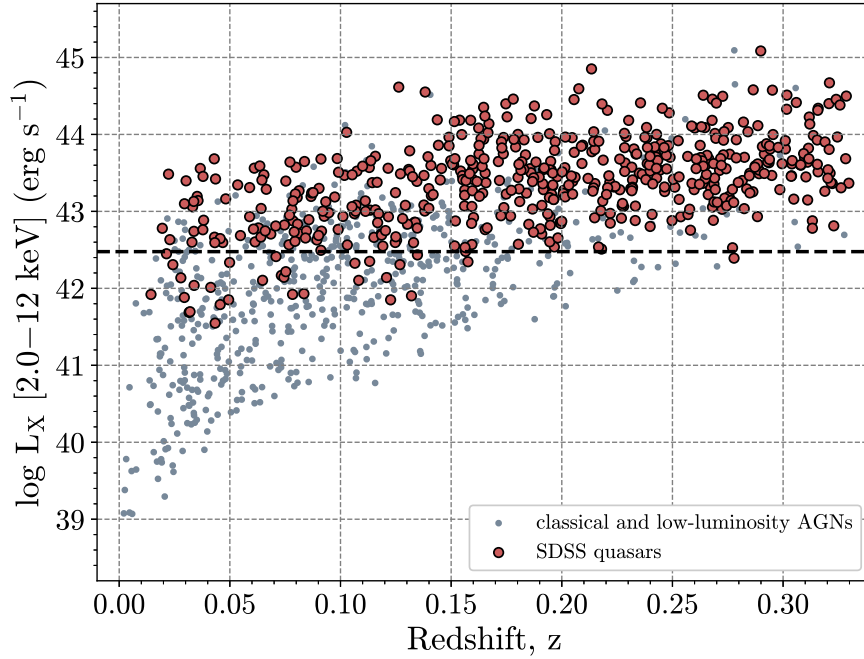


Figure 8.7: The X-ray luminosity vs. redshift for the quasars selected from SDSS quasar catalogue (red circles) and 570 AGN with from X-ray sample (grey circles). The horizontal dashed line indicates $L_{X,\text{int}} \geq 3 \cdot 10^{42} \text{ erg s}^{-1}$ criteria utilised to classify AGN in Section 5.2.

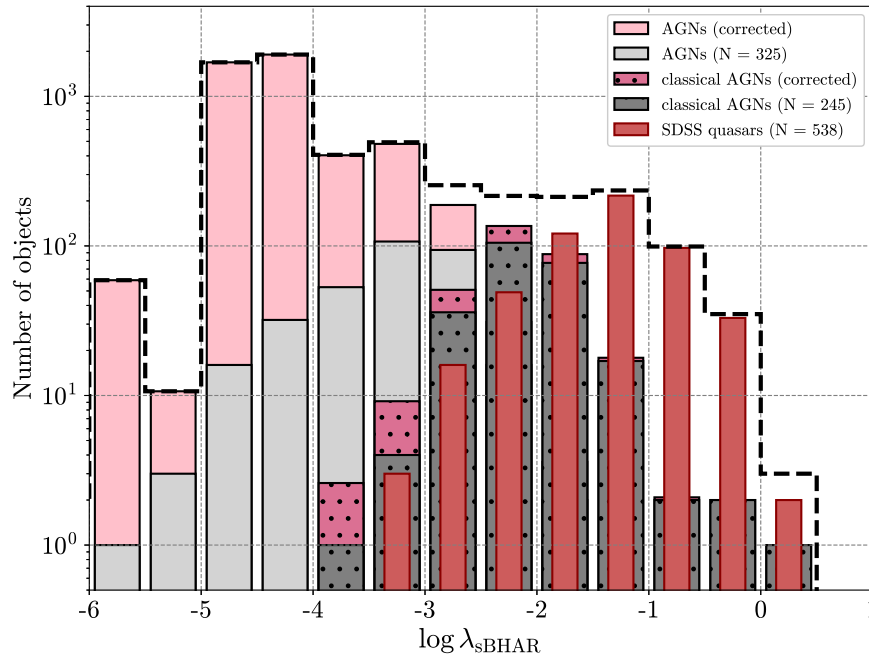


Figure 8.8: The distribution of sBHAR for all ‘classical’ and low-luminosity AGN described in Section 7.2 before and after correction for the 3XMM survey sensitivity (grey and pink colours). The sBHAR distribution for SDSS quasars is presented by dark red color and narrower bars. The sBHAR distribution for the combination of our sample and SDSS quasars is presented by the black dashed line.

type (star-forming or quiescent galaxies) as well as stellar mass and SFR are not available for these quasars. As it was expected the quasars show higher BH accretion rates with the peak at $\log \lambda_{\text{sBHAR}} \approx -1$ similar to ‘classical’ AGN studied in this work (Section 7.2). We did not apply the flux-upper limit correction as for AGN (described in Section 7.2) since the majority of the quasars are really bright and their X-ray flux is obviously higher than *XMM-Newton* sensitivity limit. Figure 8.8 shows that the resulting shape of the BHAR distribution does not change dramatically after quasar inclusion and remains the power-law with flatter at lower accretion rates. It is obvious that the obtained sBHAR distribution is biased by the assumption of a fixed stellar mass for each quasar, but this analysis is only meant to show which part of the sBHAR distribution is mostly affected by quasar activity. A complete analysis should take into account the actual quasar host galaxy mass function.

Discussion 9

In chapter 7 we described the relation between the specific BH accretion rate (sBHAR) and the SFR over a wide range of total stellar mass for two main populations of galaxies, star-forming and quiescent. In this section, we discuss and interpret the obtained results in the context of the current paradigm of AGN/host galaxy co-evolution.

9.1 sBHAR distribution in the local Universe

In Section 7.2 we showed that the distribution of the specific BH accretion rate (λ_{sBHAR}) for both types of galaxy population (see Figure 7.2 and 7.3) has an approximately power-law shape with flattening at low accretion rates between $-3 \lesssim \log \lambda_{\text{sBHAR}} \lesssim -2$ for all stellar mass ranges indicating the prevalence of low-efficiency accretion in the local Universe. This trend is consistent with the studies of the BHAR probability function which shows a power-law shape with an exponential cut-off at high BHAR and flattening toward low BHAR (Aird et al. 2012, Bongiorno et al. 2012, Georgakakis et al. 2014, Aird et al. 2018; also see Section 3.2). On the other hand, ‘classical’ AGN hosted by both star-forming and quiescent galaxies show moderate-to-high accretion rates ($\log \lambda_{\text{sBHAR}} \geq -3$). The same result was found in the studies of [Birchall](#)

et al. (2020) for a sample of dwarf galaxies and of Mendez et al. (2013) for a sample of AGN selected by IR and X-ray criteria. This result is in agreement with the fact that low-redshift galaxies are known to have lower nuclear activity than their high-redshift counterparts, based on evolutionary studies of AGN (Boyle & Terlevich 1998, Ueda et al. 2003, Hasinger et al. 2005, Ho 2008 and Section 2.2). On the other hand, to estimate SFR, we rely on an optical sample that by definition excludes bright AGN (Seyfert 1 and quasars), where the AGN continuum dominates the host galaxy emission. This explains in part the lack of sources with accretion rates $\log \lambda_{\text{sBHAR}} \geq -1$ which are found in higher redshift samples containing a larger fraction of quasars and Type 1 AGN. To confirm this we examined the SDSS DR8 quasar catalogue and found 587 objects at $z < 0.33$ with the X-ray detection in hard band in 3XMM-DR8 catalogue. Assuming the average BH mass $\sim 10^8 M_{\odot}$ we calculated the λ_{sBHAR} by Equation 7.7 and found that these objects are concentrated at higher accretion rates (a peak at $\log \lambda_{\text{sBHAR}} = -1$ in Figure 8.8) than the objects from our 3XMM-SDSS sample.

Moreover, the small fraction of objects with high accretion rate in our 3XMM-SDSS sample could be explained by the small gas supply in local galaxies as well as to the low merger rate, that could trigger AGN activity by feeding the central BH (Kauffmann & Haehnelt 2000, Hopkins et al. 2008, see details in Section 3.3). This result is consistent with Aird et al. (2018) which found a decline in the number of sources with $\log \lambda_{\text{sBHAR}} \approx 0.1$ in low redshift X-ray AGN ($z \leq 0.5$).

Furthermore, quiescent galaxies show a systematically lower sBHAR values for all stellar masses (see Figures 7.2 and 7.3). This would imply that AGN in quiescent galaxies are fuelled by a much lower gas fraction and can not sustain the same phase of SMBH accretion as AGN in star-forming galaxies with the same stellar mass (Rosario et al. 2013, Goulding et al. 2014). Several studies show that 22% of early-type galaxies in local Universe contain a significant

fraction of molecular gas (Young et al., 2011), 40% and 73% show the presence of neutral Hydrogen (Serra et al., 2012) and ionised gas (Davis et al., 2011) respectively and weak SF activity (Crocker et al., 2011). Also, Thom et al. (2012) found that the halo of early-type galaxies at $z < 1$ contains a significant fraction of cold gas which can possibly feed star-formation and AGN activity. Hence quiescent galaxies, usually-associated with elliptical galaxies, may contain a sufficient reservoir of cold gas to sustain low efficiency SMBH accretion and generate the low-luminosity AGN that we observe (see Section 3.3). Kauffmann & Heckman (2009) have also proposed an alternative scenario where the primary gas supply from stellar mass-loss in the galaxy can constantly provide gas with low angular momentum and feed a low-luminosity (i.e low-efficiently) AGN (see Section 3.3). However, such scenario predicts a decrease in BHAR at higher stellar masses as the mass-loss rate of the older stellar population in the most massive galaxies is lower, while our result in Figure 7.4 and 7.6 seem in contradiction with this prediction, revealing an increase of λ_{sBHAR} with stellar mass for star-forming galaxies, whereas quiescent ones have on the average the same λ_{sBHAR} for all range of stellar masses.

Additionally, the lower level of activity might be the signature of different accretion mode. Several theoretical models (Churazov et al. 2005, Best & Heckman 2012) claim that the radiatively inefficient SMBH accretion can be produced by so-called advection-dominated accretion flows, ADAF-mode (Narayan et al., 1997) or jet-dominated mode with mechanism of Bondi accretion of hot gas (Allen et al. 2006, Hardcastle et al. 2007 and Section 3.4).

9.2 The star-formation and Black Hole accretion connection

Several observational studies show that the SFR density and the AGN activity evolve in similar patterns with cosmic time, both peaking at redshift $z \sim 2 - 3$

and declining sharply as we move toward the present time (Madau & Dickinson, 2014) indicating that the evolution of galaxy growth and their central SMBH proceeds in a coherent way (see Section 3.1). However, the BHAR density (BHAD) has a slightly faster decay since $z \sim 2$ down to $z \sim 0$ compared to the SFR density (SFRD) since $\text{BHAD} \propto \text{SFRD}^{1.4 \pm 0.2}$ (Aird et al., 2010, Delvecchio et al., 2014, Ueda et al., 2014). In the present work, we used the median value of sBHAR to trace the average level of accretion in the local Universe (see Section 7.3) and to study the BHAR and SFR correlation. We found that star-forming galaxies possess a larger median specific accretion rate with respect to quiescent galaxies at fixed M_* . A similar difference of $\log \lambda_{\text{sBHAR}}$ for the two different galaxy populations was also presented in Delvecchio et al. (2015), Rodighiero et al. (2015), Aird et al. (2018) and can be explained, as discussed in the previous Section, by a scenario where both star-formation and AGN activity are triggered by fuelling from a common cold gas reservoir (Alexander & Hickox, 2012).

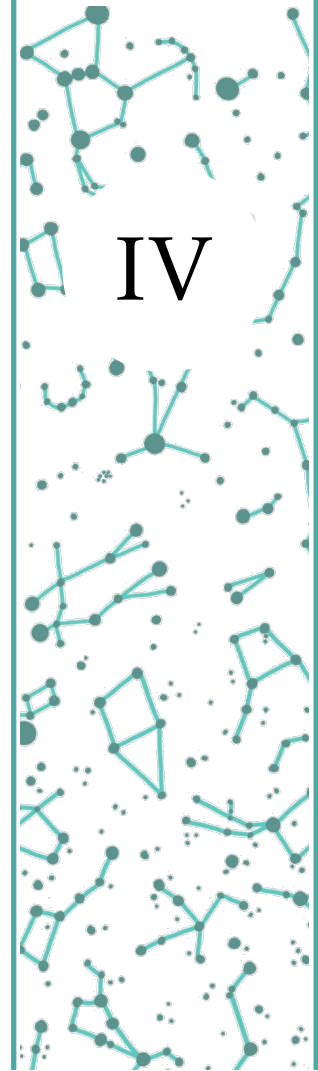
Additionally, we examined the correlation between median BHAR and SFR in more detail and found that quiescent galaxies have not only lower level of BHAR in comparison with SFGs, but in general there seems to be a continuous trend of increasing BHAR with SFR (see Figure 7.6) for all ranges of stellar mass. We found a significant correlation between the average SFR and the specific BH accretion rate for all stellar mass ranges. The linear regression analysis suggests a flatter relation (see the column with slope values in Table 7.1) for our local sample compared to other studies obtained over a wide range of both stellar mass and redshift (up to $z \sim 2.5$) (Chen et al. 2013, Delvecchio et al. 2015, Aird et al. 2019). A similarly flatter relation was observed by Delvecchio et al. (2015) for his low redshift subsample and can be likely explained by the fact that the local Universe has smaller fraction of high-luminosity AGN and powerful quasars. The existence of a correlation between SFR and sBHAR supports a scenario where both AGN activity and star-formation processes are fuelled by

a common gas supply (see Section 3.1).

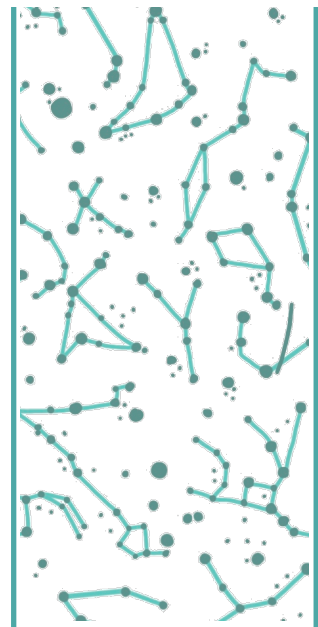
However, a number of studies also suggest an alternative scenario where AGN can enhance or quench the star-formation due to the feedback processes (Fabian 2012, Ishibashi & Fabian 2012, Heinis et al. 2016, Bluck et al. 2020). Masoura et al. (2018) compared the star-formation rate for galaxies of similar mass with/without AGN for wide redshift range and found that the AGN luminosity (i.e activity) depends on the location of the host galaxy relative to the main sequence (MS) of star-formation; they interpret this result as evidence that the AGN quenches star-formation when the galaxy is located above MS and enhances it when galaxy is below the MS. We followed the same approach and examined the connection between X-ray luminosity for star-forming galaxies and its location related to the MS of SFGs (see Section 7.3) and found a mild decrease of AGN X-ray luminosity with increasing SFR (normalised to SFR of MS), similar to the result by Masoura et al. (2018), but with a slight shift in $\log[\text{SFR}/\text{SFR}_{\text{MS}}]$.

However when splitting the sample according to the host-galaxy mass we found that the trend disappears (left panel of Figure 7.8), and is likely a systematic effect due to the lack of massive X-ray luminous galaxies with large SFR. We point out however that Masoura et al. (2018) sample larger X-ray luminosities than we do, as well as higher redshifts. In fact, Rovilos et al. (2012) found a correlation between X-ray luminosity and so-called starburstiness (i.e. the ratio of the specific SFR of the source over the main-sequence value at the given redshift) only for sources with redshift $z > 1$, while there is no correlation at lower redshift. This result is in agreement with the study of Shimizu et al. (2015) which demonstrated that X-ray luminosity of the local AGN with $z < 0.05$ (selected by the ultra-hard X-ray emission in *Swift*/BAT catalogue) does not show any relation with the increasing of distance from MS of star-forming galaxies (i.e. change of SFR). Such difference between the results in local Universe and at high redshift can indicate that AGN participated in quenching of

SFG strongly in the past where they were more powerful, while in the local Universe the average AGN output is not sufficient to affect directly star-formation processes. On the other hand, we cannot exclude either that the absence of L_X -SFR/SFR_{MS} relation can be due to the fact that both [Rovilos et al. \(2012\)](#) and [Shimizu et al. \(2015\)](#) used a sample of bright X-ray AGN, since our ‘classical’ AGN also reveal a lack of correlation (see diamond points on the left panel of Figure 7.8). A conclusive test would thus require to compare consistent samples over similar mass, SFR and redshift ranges.



**The AGN and host
galaxy co-evolution
in the local Universe
as probed by Chandra**



10

The X-ray galaxy properties from Chandra Source Catalogue

To confirm the results obtained from XMM data in Chapter 7 we perform the same analysis using the X-ray data from the *Chandra* X-ray Observatory. The *Chandra* telescope has the highest resolution among all X-ray telescopes available nowadays and allows to better discriminate the nuclear source from the host-galaxy contribution.

10.1 Chandra overview

The *Chandra X-ray Observatory*, previously known as the Advanced X-ray Astrophysics Facility (AXAF), is an X-ray space telescope launched by NASA in 1999. The mission concept is similar to the *XMM-Newton* spacecraft, but *Chandra* is more sensitive to fainter X-ray sources due to the high angular resolution of its mirrors.

As a typical X-ray telescope *Chandra* uses four nested mirrors with shape of cylindrical paraboloid and hyperboloid surface. The *Chandra* mirrors are composed by a 2cm-thick glass substrate and thin reflecting surfaces coated with iridium. The diameters of mirrors are 65 cm, 87 cm, 99 cm and 123 cm, re-

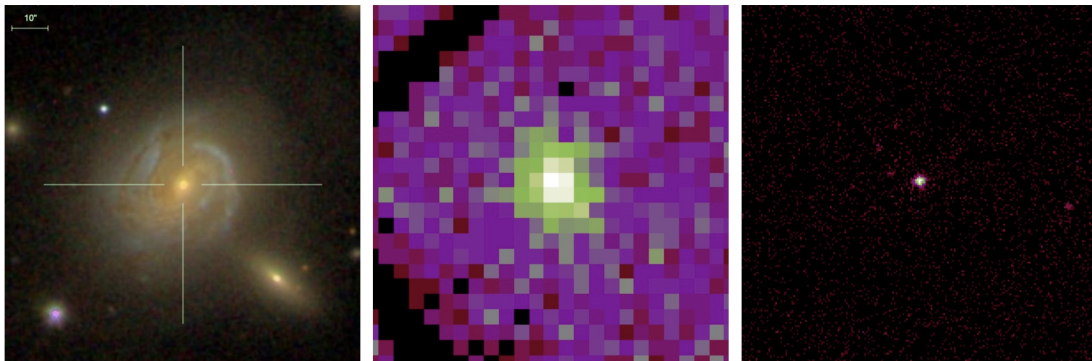


Figure 10.1: An example of spiral galaxy J130056.06+274727.0 (the sky coordinates $RA = 195.2336$, $DEC = 27.7909$ and redshift $z = 0.027$) from our SDSS galaxy sample (left) with its X-ray images obtained by XMM-Newton (centre) and Chandra (right) space telescopes. Credits: SDSS Skyserver, XMM-Newton Science Archive (XSA) and Chandra Data Archive (CDA).

spectively. Such thick glass substrate together with the careful polishing of the reflecting surface allows to focus 80-95% of the incoming X-ray energy into the circle with a diameter of $1''$ making the *Chandra* telescope resolution the highest among other X-ray telescopes; so the on-axis angular resolution of *Chandra* is $0.5''$, while the resolution of the *XMM-Newton* is close to $6''$ (see Section 4.4). However, the thickness of the *Chandra* mirrors limits the unobstructed aperture and leads to a lower collecting area compared to *XMM-Newton*. The difference in resolution between *XMM-Newton* and *Chandra* telescopes is shown in Figure 10.1 for one spiral galaxy from our SDSS galaxy sample.

Chandra has two focal plane instruments onboard: the Advanced CCD Imaging Spectrometer (ACIS) and the High Resolution Camera (HRC). The first, ACIS consists of 10 CCD chips with the energy sensitivity range from 0.2 to 10 keV. The instrument provides both imaging and spectral information of the observed object, and is able to measure both the energy and position of incoming X-rays. The second instrument is HRC, a micro-channel plate with 2 detectors optimised for different purposes: the HRC-I with a FOV of $30' \times 30'$ for imaging and the HRC-S for spectroscopy (FOV $6' \times 99'$). Comparing to ACIS instrument the HRC operates in an energy range, which is slightly extended at lower energies (0.08–10 keV) and with lower spectral resolution. At the same

time, HRC-S can work in very fast time mode (its time resolution is 16 microseconds).

Both ACIS and HRC instruments can be used (separately or in the combination) with one of the observatory's two transmission gratings for high resolution spectroscopy. The High Energy Transmission Grating Spectrometer (HETGS) operates in the energy range of 0.4–10 keV with a spectral resolution of 60–1000, while the Low Energy Transmission Grating Spectrometer (LETGS) has a range of 0.09–3 keV and a resolution of 40–2000.

All data for X-ray sources detected by the *Chandra* observatory are collected in the Chandra Source Catalog (CSC)¹. The second data release of CSC (CSC 2.0) includes the properties for 317,167 unique compact and extended X-ray sources. Derived properties are provided for 928,280 individual observation detections identified in 10,382 Chandra ACIS and HRC-I imaging observations released publicly up to the end of 2014. CSC 2.0 includes the information about each source across 5 bands: broad (0.5-7 keV), hard (2.0-7.0 keV), medium (1.2-2.0 keV), soft (0.5-1.2 keV) and ultra-soft (0.2-0.5 keV) for ACIS and 1 wide band (0.1-10 keV) for HRC (Evans et al., 2010).

10.2 The SDSS-CSC crossmatch

To compare our SDSS galaxy sample (presented in Section 4.2) and the *Chandra* footprint we used the *Chandra* Multi-Order Coverage map (MOC order 13 and no grating observations²). As a result we found that 36 220 objects from SDSS sample are falling in the area of the sky observed by the *Chandra* observatory. The distribution of both the optical galaxy sample and the *Chandra* footprint on the sky are shown in Figure 10.2.

The X-ray counterparts from the CSC 2.0 were found by using the CSCVIEW application, which allows us to find all available X-ray counterparts using the

¹<https://cxc.harvard.edu/csc/index.html>

²https://cxc.harvard.edu/cda/cda_moc.html

objects coordinates. Using an initial conservative radius of $20''$ (to include poorly resolved sources far from the optical axis) we found 3 390 sources detected by the ACIS camera. To properly take into account the variable spatial resolution of *Chandra* data and its dependence on the source flux, we then required a crossmatch probability (i.e the one-dimensional probability that the separation between the CSC source position and the SDSS galaxy position is greater than or equal to the radial separation between these positions³) to be > 0.05 .

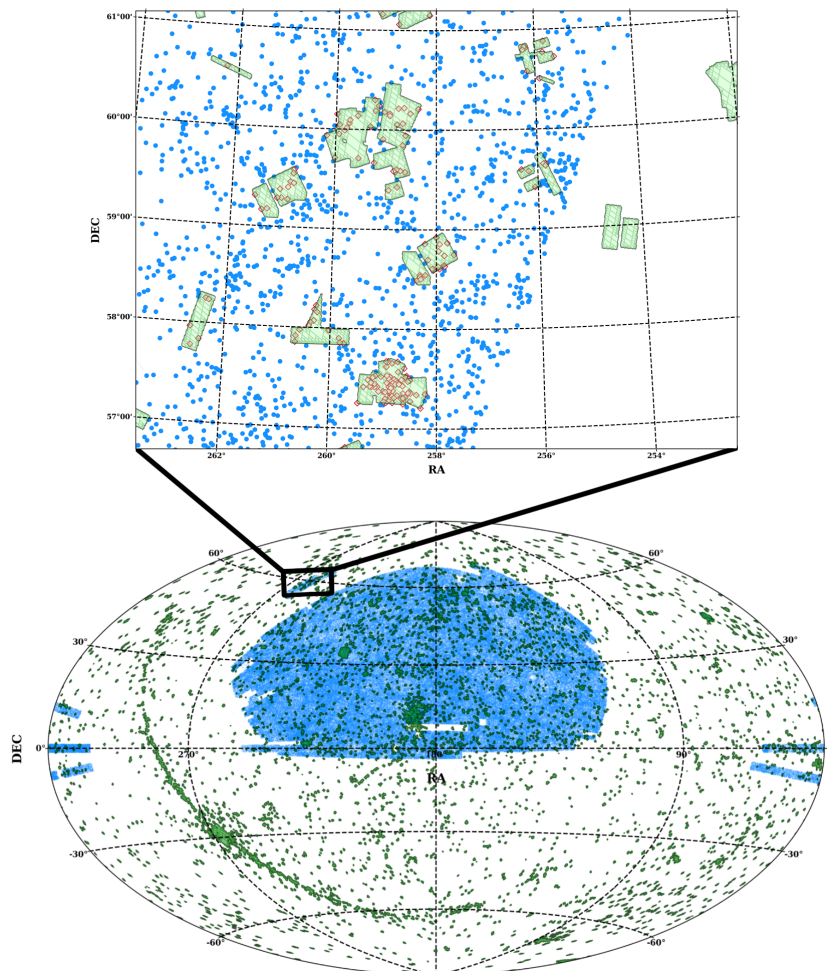


Figure 10.2: The sky distribution of all galaxies from our SDSS galaxy sample (blue color) and *Chandra* footprint area (green color). In the top panel the optical galaxies inside the area observed by *Chandra* are showed by red diamonds, while the objects outside the footprints are marked by blue circles.

³https://cxc.harvard.edu/csc/why/cscview_xmatch.html

Since several objects can appear in multiple observations we choose only the one with the highest exposure time. Also, in a similar way to 3XMM data in Section 4.5 we selected objects with zero extension parameter, to avoid including spatially extended objects (such as hot gas regions or galaxy clusters). After all these filters we obtained 1 217 sources in our X-ray *Chandra* sample.

Finally, we choose only the objects with reliable detection in the hard band (2.0–7.0 keV). As a result, our final CSC-SDSS sample contains 863 objects (428 star-forming and 425 quiescent galaxies); their distribution on SFR– \mathcal{M}_* plane is shown in Figure 10.3 by grey circles.

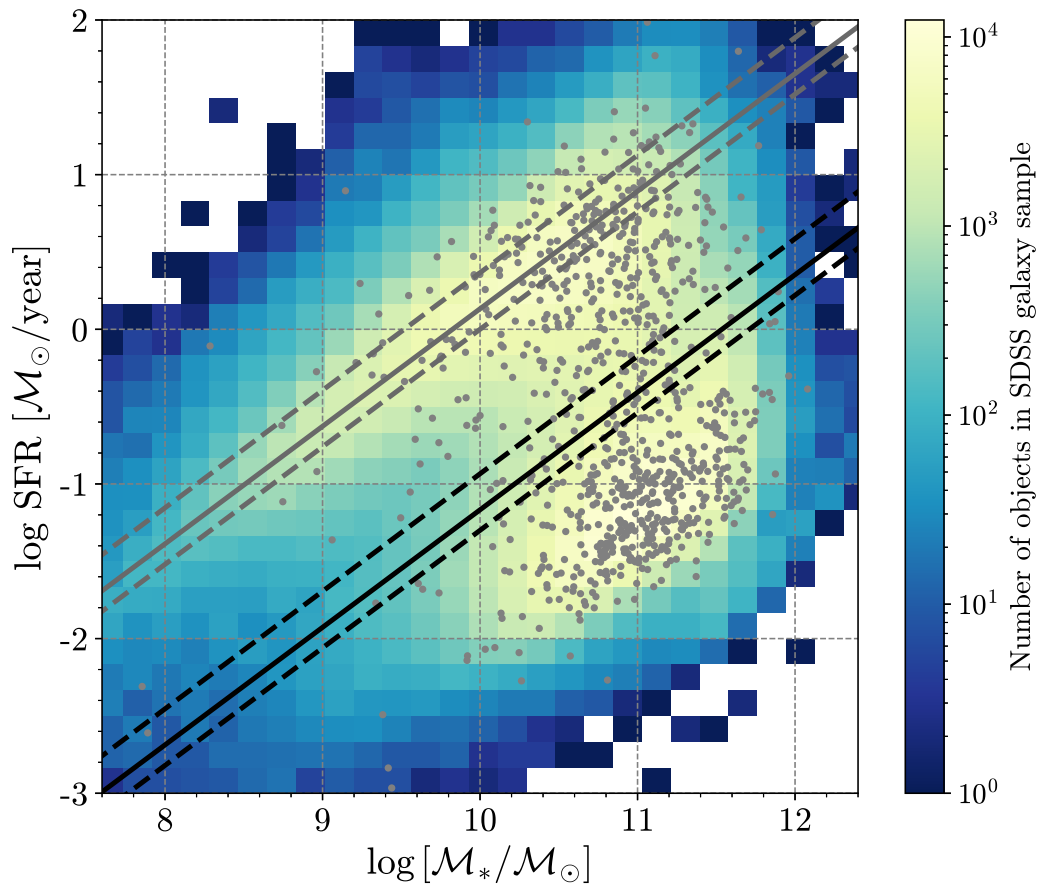


Figure 10.3: The distribution of star-formation rate vs. stellar mass for our SDSS galaxy sample. The distribution of our final X-ray sample extracted from the *Chandra* Source Catalogue is shown by grey circles.

10.3 The identification of ‘classical’ AGN

We classified an X-ray source as an AGN using the same X-ray criteria described in Section 5.2: (1) an intrinsic luminosity $L_{X,\text{int}} \geq 3 \cdot 10^{42} \text{ erg s}^{-1}$ in the hard band; (2) X-ray-to-optical flux ratio of $\log(f_X/f_{\text{opt}}) > -1$ or (3) X-ray-to-IR flux ratio of $\log(f_X/f_{\text{Ks}}) > -1.2$. The X-ray luminosity in the hard band (2.0–7.0 keV) was calculated from the energy flux using the Equation 5.2. In our study we used the best estimate background-subtracted flux in the modified source region, which calculated by counting X-ray events in the hard band and corrected by the appropriate PSF aperture fractions, livetime, and exposure, for the Bayesian Block with the largest exposure.

In total, we identified 156 ‘classical’ AGN (18.0% of our CSC-SDSS sample), 91 were selected by the X-ray luminosity threshold, 138 and 131 by X-ray-to-optical flux ratio in *r*- and *i*-bands and 97 by X-ray/IR flux ratio. Only 56 objects are classified as AGN by all criteria. The redshift distribution of AGN selected by the L_X criterion are shown in Figure 10.4, the X-ray/optical flux ratios in SDSS *r*- and *i*-band (top panel) and X-ray/IR flux ratio are presented in Figure 10.5 (bottom panel).

The distribution of our sample on the SFR vs stellar mass diagrams in the hard band is shown in Figure 10.6. AGN selected with the above X-ray criteria show a behaviour similar to the AGN classified from 3XMM-DR8 data: the ‘classical’ AGN selected from CSC-SDSS sample also seem to occupy predominantly the star-forming main-sequence (78.2% of all X-ray selected AGN) instead of quiescent galaxies (only 21.8%). At the same time, the percentage of star-forming and quiescent galaxies hosting an AGN in our CSC-SDSS sample are 14.1% and 3.9%, respectively. In Section 5.2 we found that ‘classical’ AGN selected from the 3XMM-DR8 are twice as likely to be hosted by star-forming galaxies than by quiescent ones. ‘Classical’ AGN classified from the CSC-SDSS sample also show similar trend, however the number of ‘classical’ AGN hosted

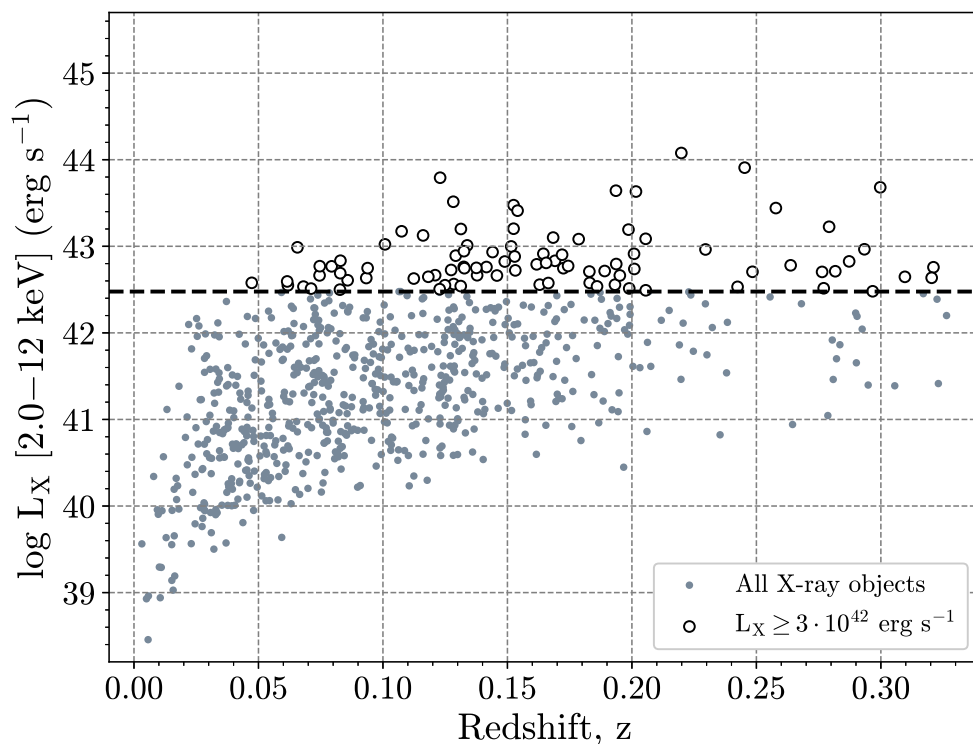


Figure 10.4: The X-ray luminosity vs. redshift for the objects in X-ray sample. The horizontal dashed line indicates $L_{X,\text{int}} \geq 3 \cdot 10^{42} \text{ erg s}^{-1}$ criteria utilized to classify AGN (black circles).

by star-forming galaxies is three times higher than by quiescent ones, while for the 3XMM this ratio was only two to one. This effect may be due to the higher resolution of the *Chandra* telescope compared to *XMM-Newton*, which makes *Chandra* able to resolve circumnuclear hot gas in quiescent galaxies. Such sources are usually classified as an extended and hence are not included in our CSC-SDSS sample.

In Section 9.1 we have already discussed that the empirical AGN selection criteria are able to identify only AGN-dominated objects and low luminosity AGN with radiatively inefficient accretion. In the case of the 3XMM data, we estimated the contribution of the host galaxy to the total X-ray luminosity before including these objects in our study. For this purpose, we derived the X-ray luminosity for different types of X-ray binaries and hot gas from scaling relations and subtracted it from the K-corrected X-ray luminosity (see Section 6.2). The *Chandra* telescope has higher resolution than *XMM-Newton* and is able to

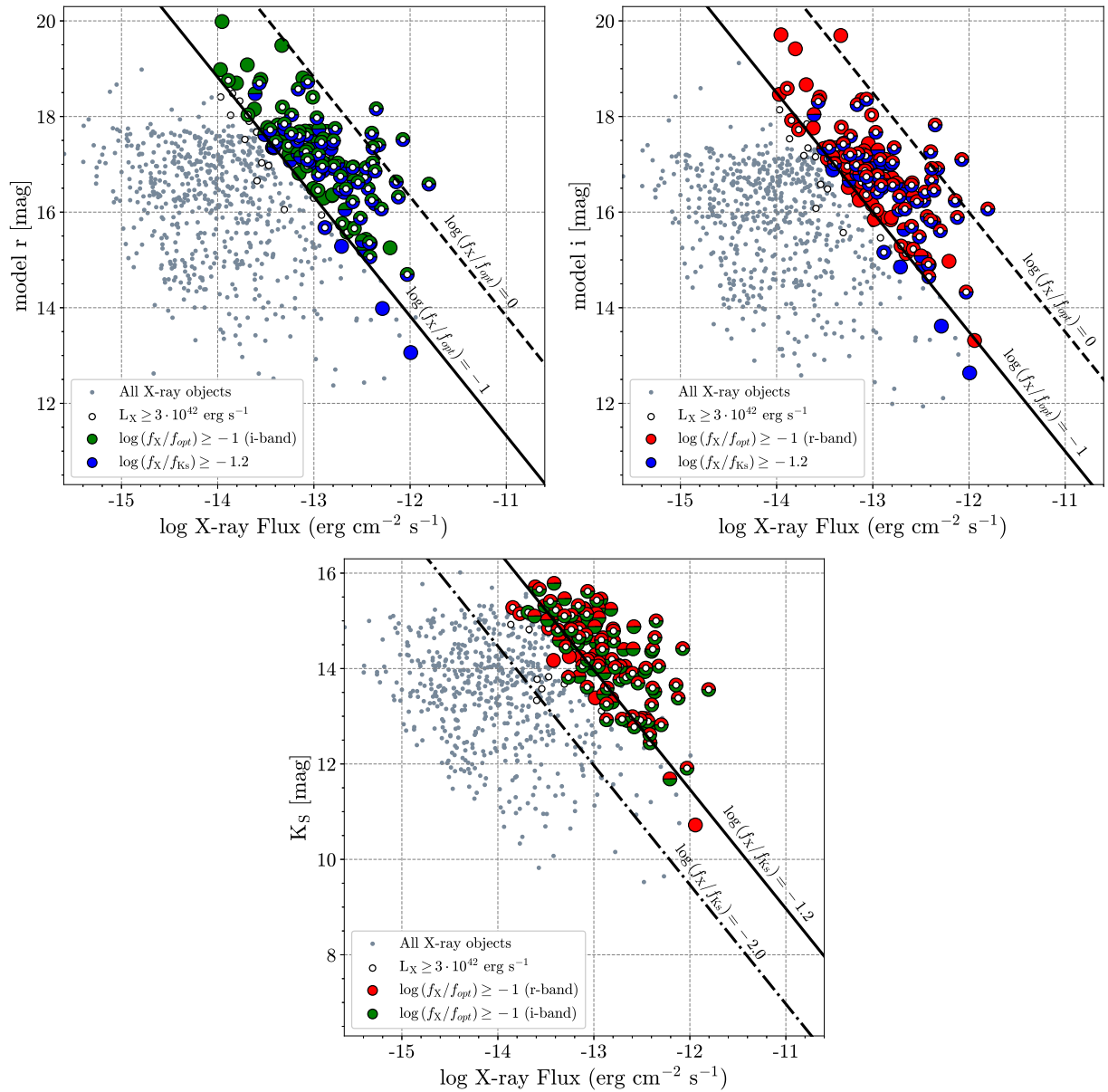


Figure 10.5: Top: The X-ray flux in hard band vs. optical SDSS r-band and i-band magnitude for sources in Chandra X-ray sample (grey circles). White circles indicate AGN having $L_{X,int} \geq 3 \cdot 10^{42}$ erg s⁻¹ in Figure 5.3. AGN selected by the X-ray/optical flux ratios in r- and i-band are represented by red and green circles, by X-ray/IR ratio by blue circles. Diagonal lines indicate constant flux ratios between the SDSS r- and i-band and X-ray hard band, the area under the line $\log(f_X/f_{opt}) > -1$ is used as one of the criteria to classify the location of AGN. Bottom: The X-ray flux in hard band vs. 2MASS infrared K_s-band magnitude. The colors of circles are the same as on top panel. Diagonal lines indicate constant flux ratios between the 2MASS K_s-band and X-ray hard band, the area under the line $\log(f_X/f_{Ks}) > -1.2$ is used as one of the criteria to classify the location of AGN.

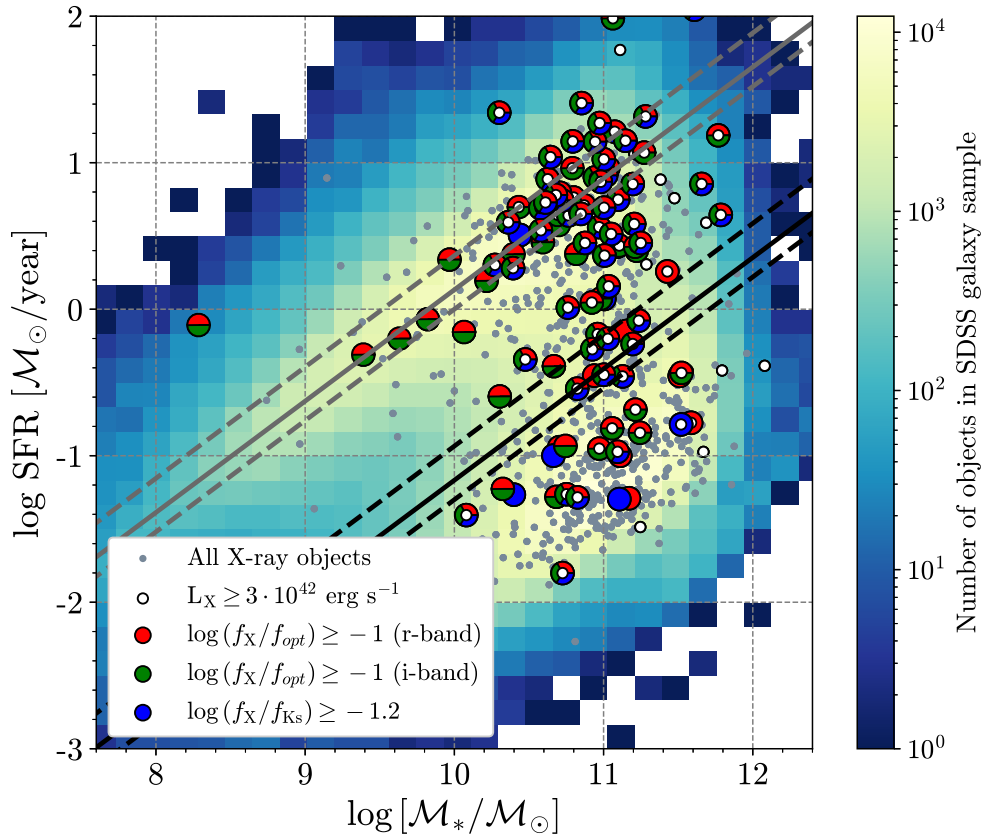


Figure 10.6: The distribution of star-formation rate vs. stellar mass for Chandra X-ray sample in hard band (grey circles). The gradient from blue to yellow shows the 2D histogram of the density distribution of galaxies in our optical SDSS sample. All symbols represent the AGN selected by the X-ray criteria described in Section 5.2.

more easily separate the nuclear emission from the host-galaxy contribution, the faintest objects or the galaxies at greater distances (i.e. smaller angular size of the object). In principle we should estimate the fractional contribution of the host galaxy within the region where the X-ray flux is measured, which is a challenging task for the entire CSC-SDSS sample. Instead we followed a simpler approach estimating an upper limit to the corrections assuming that the contribution is due to the entire galaxy, and we repeated the same analysis as for the 3XMM data (see Section 6.2).

As a result, 750 objects have positive residual X-ray luminosity after correction (86.9% from the CSC-SDSS sample before correction), 391 of which are SFGs and 359 are quiescent ETGs. TFigure 10.7 shows that the X-ray correction

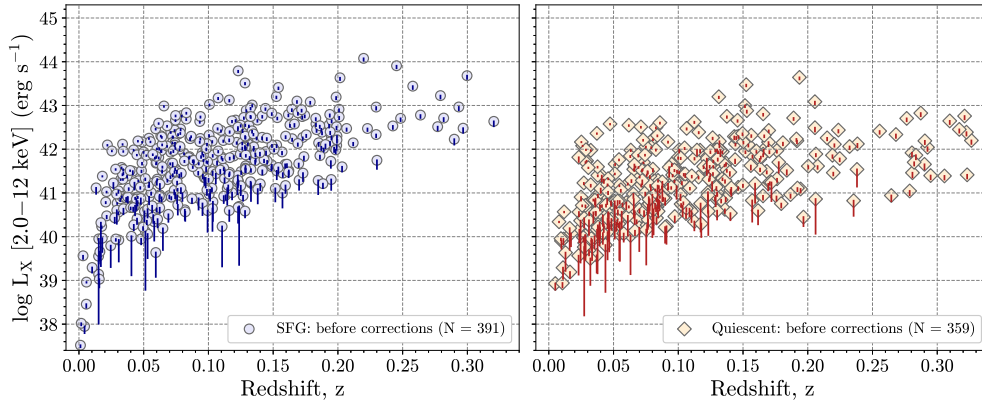


Figure 10.7: The X-ray luminosity vs redshift distribution of the 750 objects from our Chandra sample. The uncorrected L_X values for SFGs and passive galaxies are presented on left and right panels as solid circles and diamonds, respectively. The change in L_X after corrections for each object is shown by a solid line.

is small for the majority of the objects and hence we decided to make all subsequent calculations using the uncorrected X-ray luminosity. This will result in an overestimate of the AGN luminosity, so our results should be considered an upper limit, although the difference with the actual value is usually negligible.

11

The BHAR correlation with host galaxy properties

In this Chapter we repeated all the calculations and analysis described in Chapter 7 using the X-ray data from the Chandra Source Catalogue.

11.1 The BHAR distribution for *Chandra* data

The sBHAR distribution obtained from the *Chandra* data for star-forming and quiescent galaxies are shown in Figure 11.1. These histograms represent the original data without any correction for the *Chandra* survey sensitivity (this correction will be done in future work). In any case, the uncorrected sBHAR distribution shows properties similar to the sBHAR distribution obtained for the 3XMM-SDSS sample (see Section 7.2). ‘Classical’ AGNs have higher accretion rates ($\log \lambda_{\text{sBHAR}} \geq 3$) than the rest of low-luminosity AGN both for both star-forming and quiescent galaxies. At the same time, quiescent galaxies show a slightly lower values of the sBHAR than star-forming ones.

The shape of the sBHAR distribution is close to a power-law with flattening at low accretion between $-3 \lesssim \log \lambda_{\text{sBHAR}} \lesssim -2$ both for SFG and quiescent galaxies, however the final conclusion can be made only after the correction

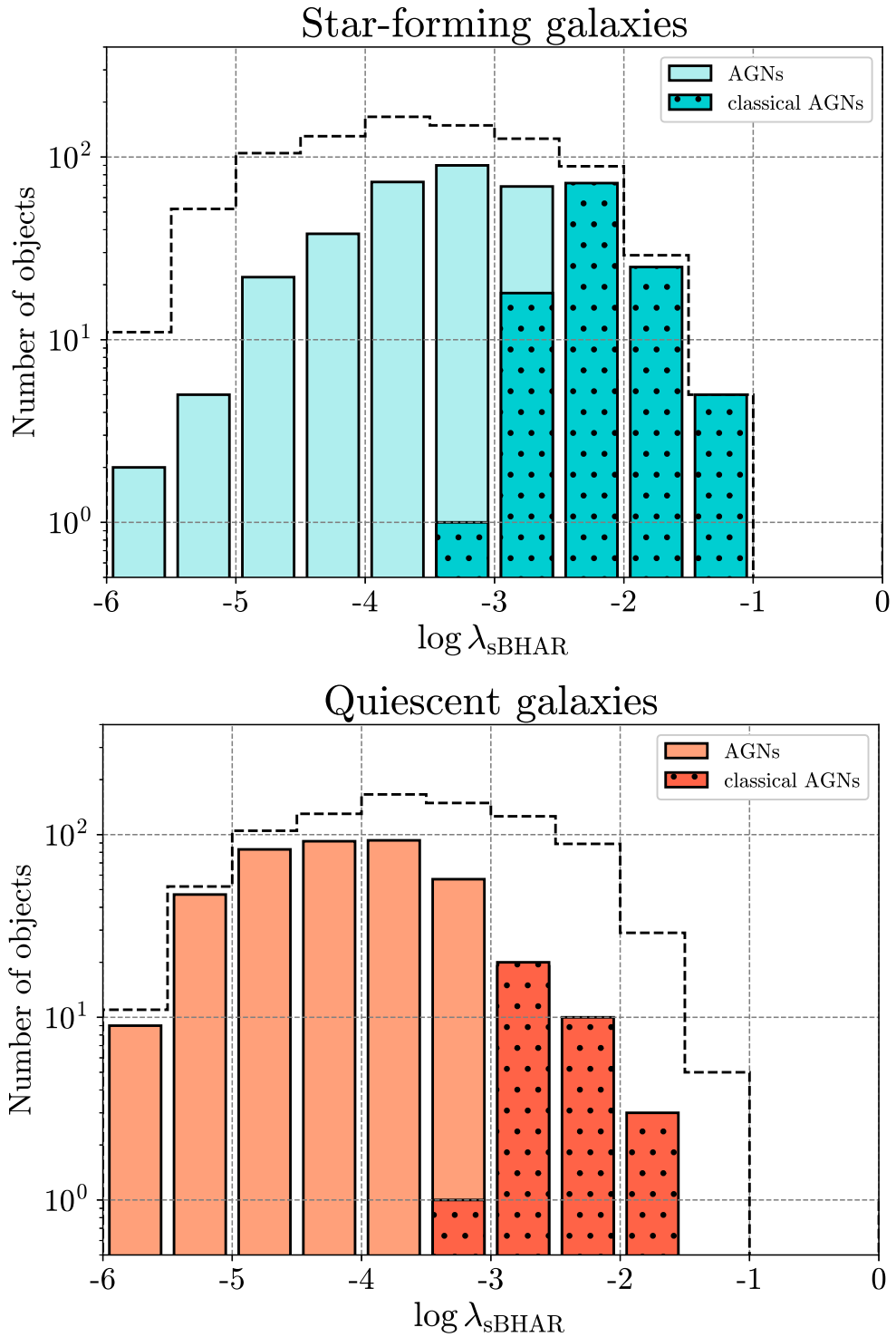


Figure 11.1: The distribution of the specific Black Hole accretion rate (sBHAR) for AGN in star-forming (top) and quiescent galaxies (bottom). ‘Classical’ AGN (Section 10.3) are shown by the dotted area and darker colour. All data are presented before correcting for the Chandra sensitivity. The black dashed line represents the total distribution of sources in the CSC-SDSS sample without SF/quiescent galaxy separation.

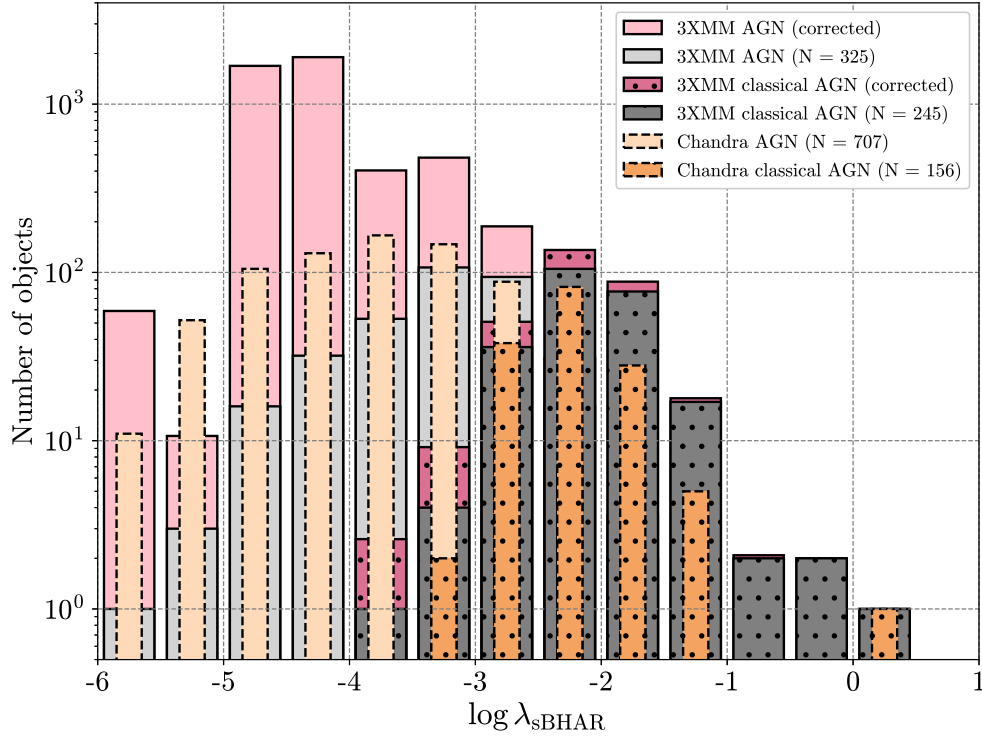


Figure 11.2: The distribution of $sBHAR$ for ‘classical’ and low-luminosity AGN from 3XMM-DR8 and CSC 2.0 samples. The distribution of $sBHAR$ for 3XMM AGN sample described in Section 7.2 before and after correction for the 3XMM survey sensitivity (grey and pink colours), while the data for CSC AGN sample (see Section 11.1) are presented only before correcting for the Chandra sensitivity (brown colors).

for the *Chandra* survey sensitivity. In addition, the $sBHAR$ distribution obtained for the CSC-SDSS sample is obviously consistent with the distribution for 3XMM-SDSS sample (see Figure 11.2).

11.2 The BHAR correlation with stellar mass and star-formation rate

Following the same steps described in Section 7.3 we divided our CSC-SDSS sample in bins of SFR and M_* and calculated the median λ_{sBHAR} and L_X in each bin. The distribution of λ_{sBHAR} (and L_X) on the SFR– M_* diagram is shown in Figure 11.3. To verify the statistical significance of the correlation between $sBHAR$ and the host galaxy properties (Figure 11.3) we applied the one-way ANOVA for $sBHAR$ and L_X values in six stellar mass bins for star-forming and

quiescent galaxies separately. The analysis reveals a significant statistical difference in both L_X and sBHAR between 6 stellar mass bins for star-forming galaxies (P value = 0.00 for L_X and P value = 0.001 for sBHAR). However, quiescent galaxies with different stellar masses have on average the same values of sBHAR (P value = 0.087) and significantly different L_X (P value = 0.029).

Furthermore, we calculated the mean $\langle \lambda_{\text{sBHAR}} \rangle$ in 10 bins of SFR in the range $3.0 < \log \text{SFR} < 2.0$, where the uncertainty of $\langle \lambda_{\text{sBHAR}} \rangle$ was computed using jackknife resampling. The $\langle \log \lambda_{\text{sBHAR}} \rangle - \log \text{SFR}$ correlation is presented in six stellar mass ranges in Figure 11.5. We applied the regression analysis and fitted the BHAR-SFR correlation using the linear approximation and least-squares regression model. The best-fit parameters are listed in Table 11.1.

The statistical analysis confirms that sBHAR correlates with SFR at $> 95\%$ confidence (P -value < 0.05) only for 3 stellar mass intervals (the intervals #3,4,5 on Table 11.1), instead of 5 stellar mass intervals as for 3XMM data (see Section 7.3). The existence of the sBHAR-SFR trend for the other two mass intervals cannot be verified due to the small number of star-forming galaxies in the mass interval #6 and of quiescent galaxies in the mass interval #1. The situation with the mass interval #2 is more complicated because the P -value confirms the existence of sBHAR-SFR correlation, however the higher value of the obtained slope in Figure 11.5 is clearly driven by the presence of 4 quiescent galaxies with significantly lower sBHAR comparing to other objects in this mass interval. Therefore the obtained result for the mass interval #2 cannot be perceived as a reliable.

Figure 11.6 shows the comparison of the sBHAR-SFR correlation obtained for the CSC-SDSS and the 3XMM-SDSS samples. The best-fitting slope obtained for the CSC-SDSS sample is close to the result obtained for the 3XMM-SDSS sample and shows the same linear $\langle \log \lambda_{\text{sBHAR}} \rangle - \log \text{SFR}$ relation with a flatter slope when compared to the high- z studies (see Section 7.3 and [Chen et al. 2013](#), [Delvecchio et al. 2015](#), [Aird et al. 2019](#)).

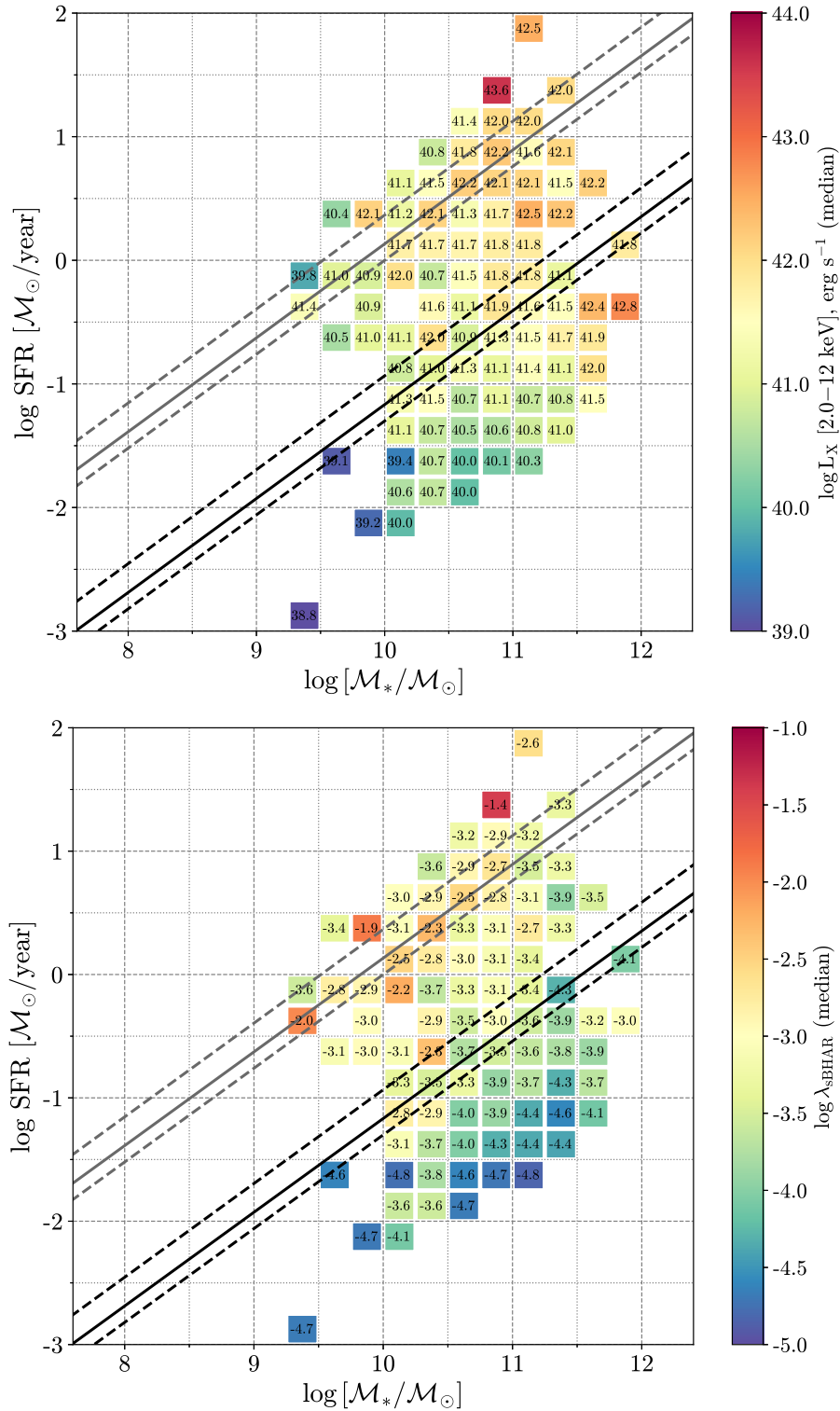


Figure 11.3: The distribution of X-ray luminosity (top) and the specific BH accretion rate λ_{sBHAR} (bottom) on SFR– \mathcal{M}_* plane for Chandra AGN sample. The actual median value of λ_{sBHAR} (X-ray luminosity) for each bin of SFR and \mathcal{M}_* is written inside the square. The black and grey lines are the same as in Figure 4.2. Number of points in both diagrams ranges from 41 in the central part to 2-3 in the edges (see Figure 11.4).

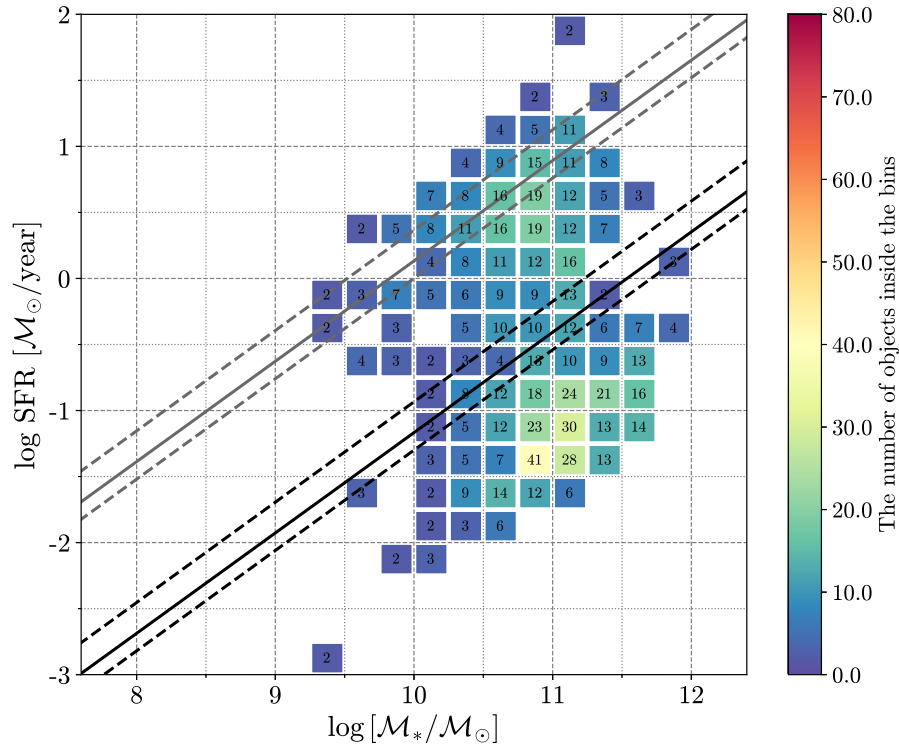


Figure 11.4: Number of points in each SFR and M_* bin for both diagram presented in Figure 7.4.

The crossmatch between the CSC-SDSS and the 3XMM-SDSS samples returned only 140 objects (8.6% of the 3XMM-SDSS sample and 18.7% from the CSC-SDSS sample). In the future we will combine these samples to improve the statistic significance of our results (the number of the studied objects may be increased by 37.5%) after including the corrections for host galaxy emission and flux sensitivity of the *Chandra* telescope.

Table 11.1: The best-fit parameters obtained from a linear relation between $\langle \log \lambda_{\text{SBHAR}} \rangle$ and $\log \text{SFR}$ for six stellar mass ranges for the CSC-SDSS sample (see Figure 7.6). The slope, intercept with their standard errors and all statistics parameters (F -statistic, P value and R^2) were found from the least-square linear regression. In this work, we consider the confident level as P -value < 0.05 . N is the number of points in each stellar mass bin.

#	Stellar mass range	slope	intercept	F -statistic	P value (F -stat)	R^2	N
1	$\log [M_*/M_\odot] < 9.5$	0.23 ± 0.21	-2.36 ± 0.53	1.16	0.3230	0.16	8
2	$9.5 < \log [M_*/M_\odot] < 10.0$	0.84 ± 0.04	-2.80 ± 0.09	384.5	0.0003	0.99	5
3	$10.0 < \log [M_*/M_\odot] < 10.5$	0.41 ± 0.09	-3.10 ± 0.09	20.94	0.0038	0.77	8
4	$10.5 < \log [M_*/M_\odot] < 11.0$	0.59 ± 0.05	-3.36 ± 0.05	138.6	$7.2 \cdot 10^{-6}$	0.95	9
5	$11.0 < \log [M_*/M_\odot] < 11.5$	0.54 ± 0.03	-3.56 ± 0.04	286.0	$6.2 \cdot 10^{-7}$	0.98	9
6	$\log [M_*/M_\odot] > 11.5$	0.56 ± 0.24	-3.49 ± 0.22	5.572	0.0099	0.65	5

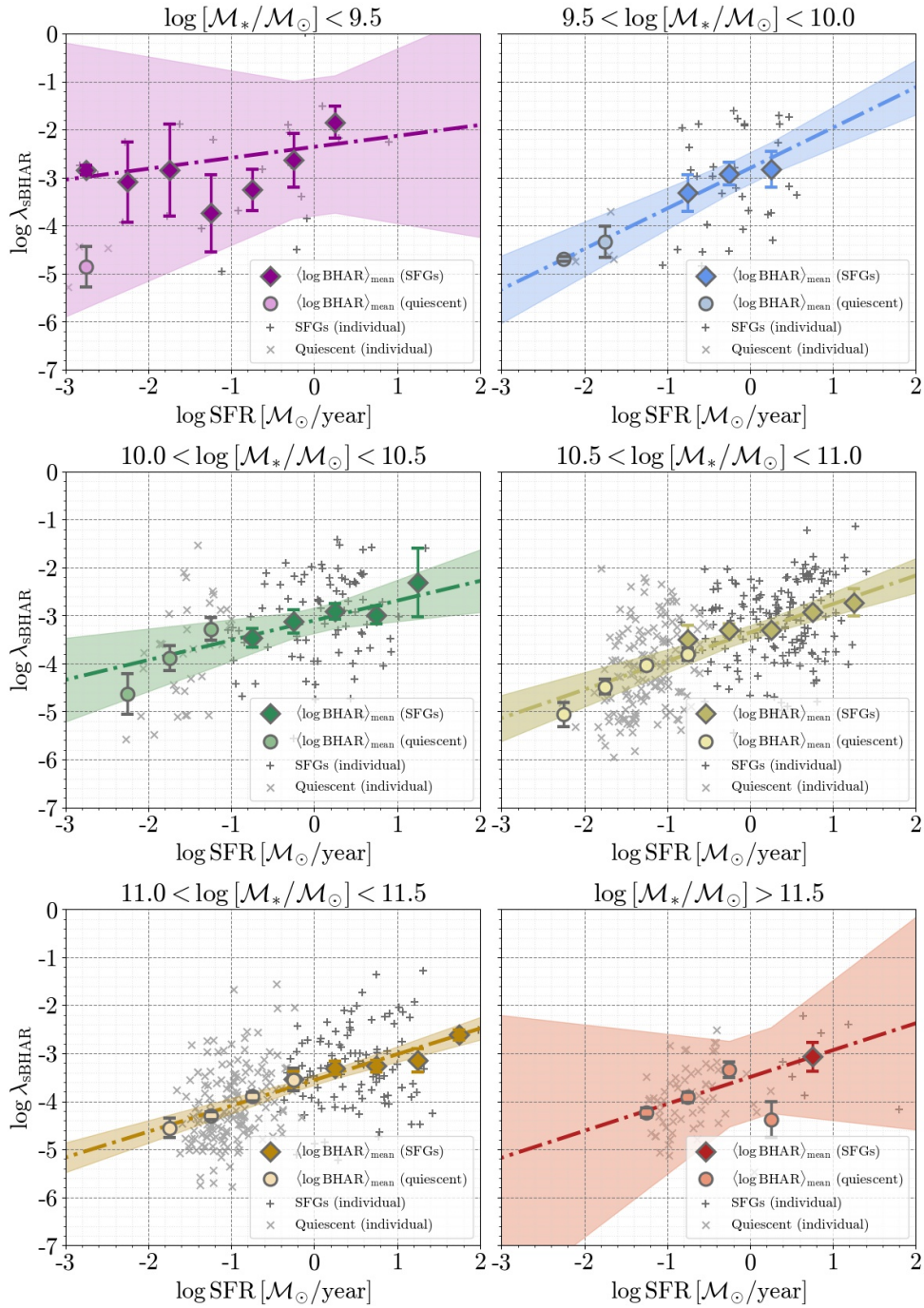


Figure 11.5: The jackknife mean value of sBHR vs SFR for star-forming (diamond) and quiescent galaxies (circles) for six stellar masses ranges. The individual objects from our CSC AGN sample represented by grey crosses (SFGs) and pluses (quiescent). The errorbars were calculated as a variance of the jackknife mean. The dashed line shows the least-square linear best-fit with 95% confidence interval. The best-fit and goodness-of-fit parameters are presented in Table 11.1.

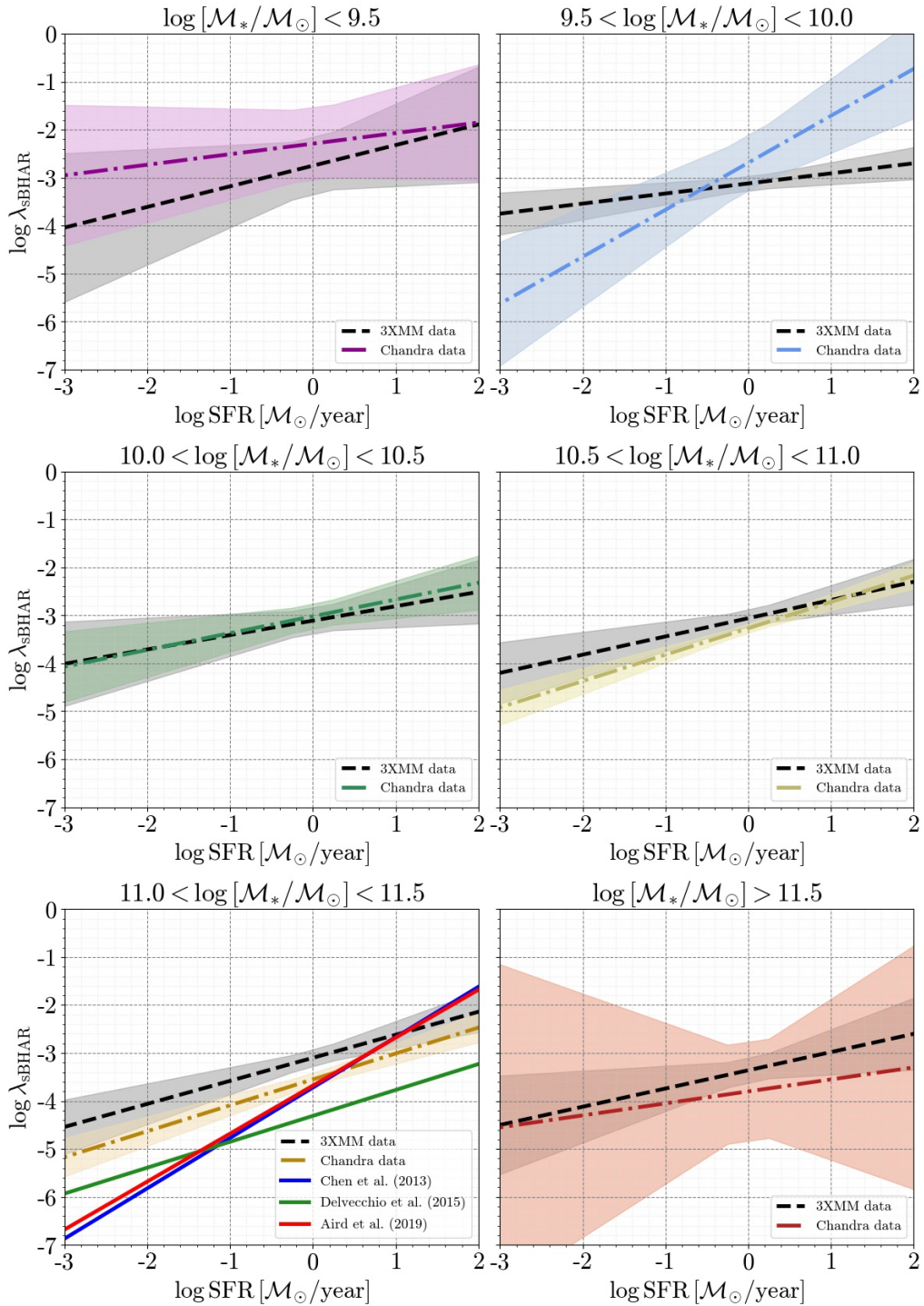


Figure 11.6: The least-square linear best-fit of sBHR vs SFR correlation with 95% confidence interval in six stellar masses ranges for 3XMM (dashdot line) and CSC (dashed line) samples. The best-fit and goodness-of-fit parameters for 3XMM and CSC samples are presented in Tables 7.1 and 11.1, respectively. The best-fits of sBHR-SFR correlation from works of [Chen et al. \(2013\)](#), [Delvecchio et al. \(2015\)](#) and [Aird et al. \(2019\)](#) are presented by solid blue, green and red lines, respectively.

Conclusions

In this paper we analysed the intrinsic distribution of SMBH accretion in the local Universe. The parent sample is extracted from the SDSS galaxy catalogue produced by the MPA–JHU group, containing spectroscopic SFR and \mathcal{M}_* estimates. Using X-ray detections from the 3XMM-DR8 and CSC 2.0 we measured the average sBHAR in these galaxies and investigated the relation between sBHAR and SFR for star-forming and quiescent galaxy over a wide range of stellar masses. Our main conclusions are the following:

- 1) ‘Classical’ AGN with moderate to high efficiency accretion ($\log \lambda_{\text{sBHAR}} > -3$) only represent 24% of our 3XMM detected sample (18% of our CSC sample) and only 1% (0.4%) of the whole galaxy population;
- 2) ‘Classical’ AGN are twice as likely to occupy galaxies with active star-forming processes (i.e. high SFR) than quiescent systems;
- 3) Overall 5% of our galaxy sample hosts an accreting SMBH. The majority of these objects accrete at very low rates, revealing a power-law sBHAR distribution with flattening at $\log \lambda_{\text{sBHAR}} \lesssim -2$ for star-forming galaxies; quiescent galaxies show a tendency to accrete at even lower $\log \lambda_{\text{sBHAR}} \lesssim -3$;
- 4) The median X-ray luminosity for both samples reveals a dependence on the host galaxy stellar mass for both star-forming and quiescent galaxies,

while median $\log \lambda_{\text{sBHAR}}$ shows a slight increase with stellar mass only for star-forming galaxies (only in case of 3XMM data). Additionally, star-forming galaxies accrete more at fixed stellar mass than quiescent galaxies;

- 5) We observe a significant correlation between $\log \lambda_{\text{sBHAR}}$ and $\log \text{SFR}$ in almost all stellar mass ranges, where quiescent galaxies have a systematically lower level of λ_{sBHAR} than star-forming systems.

Our results support a picture where the local AGN population is dominated by very low-to-moderate luminosity systems, i.e. inefficiently-accreting SMBH. Our findings show that AGN activity in star-forming galaxies is enhanced with respect to quiescent systems; this may be caused by the different amounts of accreting material present in these types of galaxies or may also indicate a possible difference of the physical mechanisms responsible for the triggering and fuelling of AGN described in the literature (e.g. the stochastic fuelling by cold gas in SFGs and the stellar mass loss or cooling flows in quiescent galaxies).

Bibliography

- Abramowicz M. A. and Fragile P. C. (2013). Foundations of Black Hole Accretion Disk Theory. *Living Reviews in Relativity*, **16**(1), 1.
- Aihara H., Allende Prieto C., An D., et al. (2011). The Eighth Data Release of the Sloan Digital Sky Survey: First Data from SDSS-III. *Astrophys. J. Suppl. Ser.*, **193**(2), 29.
- Aird J., Nandra K., Laird E. S., et al. (2010). The evolution of the hard X-ray luminosity function of AGN. *Mon. Notic. Roy. Astron. Soc.*, **401**(4), 2531–2551.
- Aird J., Coil A. L., Moustakas J., et al. (2012). PRIMUS: The Dependence of AGN Accretion on Host Stellar Mass and Color. *Astrophys. J.*, **746**(1), 90.
- Aird J., Coil A. L., Moustakas J., et al. (2013). PRIMUS: An Observationally Motivated Model to Connect the Evolution of the Active Galactic Nucleus and Galaxy Populations out to $z \sim 1$. *Astrophys. J.*, **775**(1), 41.
- Aird J., Coil A. L., Georgakakis A., et al. (2015). The evolution of the X-ray luminosity functions of unabsorbed and absorbed AGNs out to $z \sim 5$. *Mon. Notic. Roy. Astron. Soc.*, **451**(2), 1892–1927.
- Aird J., Coil A. L., and Georgakakis A. (2017). X-rays across the galaxy population - I. Tracing the main sequence of star formation. *Mon. Notic. Roy. Astron. Soc.*, **465**(3), 3390–3415.

- Aird J., Coil A. L., and Georgakakis A. (2018). X-rays across the galaxy population - II. The distribution of AGN accretion rates as a function of stellar mass and redshift. *Mon. Notic. Roy. Astron. Soc.*, **474**, 1225–1249.
- Aird J., Coil A. L., and Georgakakis A. (2019). X-rays across the galaxy population - III. The incidence of AGN as a function of star formation rate. *Mon. Notic. Roy. Astron. Soc.*, **484**(3), 4360–4378.
- Alexander D. M. and Hickox R. C. (2012). What drives the growth of black holes? *New Astron. Rev.*, **56**(4), 93–121.
- Alexander D. M., Hough J. H., Young S., et al. (1999). Searching for the hidden broad-line region in Centaurus A. *Mon. Notic. Roy. Astron. Soc.*, **303**(2), L17–L22.
- Allen S. W., Dunn R. J. H., Fabian A. C., Taylor G. B., and Reynolds C. S. (2006). The relation between accretion rate and jet power in X-ray luminous elliptical galaxies. *Mon. Notic. Roy. Astron. Soc.*, **372**(1), 21–30.
- Ananna T. T., Salvato M., LaMassa S., et al. (2017). AGN Populations in Large-volume X-Ray Surveys: Photometric Redshifts and Population Types Found in the Stripe 82X Survey. *Astrophys. J.*, **850**(1), 66.
- Antonucci R. R. J. and Miller J. S. (1985). Spectropolarimetry and the nature of NGC 1068. *Astrophys. J.*, **297**, 621–632.
- Antonucci R. (1993). Unified models for active galactic nuclei and quasars. *Annual Rev. Astron. & Astrophys.*, **31**, 473–521.
- Azadi M., Aird J., Coil A. L., et al. (2015). PRIMUS: The Relationship between Star Formation and AGN Accretion. *Astrophys. J.*, **806**(2), 187.
- Baldi R. D., Capetti A., and Giovannini G. (2016). The new class of FR 0 radio galaxies. *Astronomische Nachrichten*, **337**(1-2), 114.

- Baldry I. K., Glazebrook K., Brinkmann J., et al. (2004). Quantifying the Bimodal Color-Magnitude Distribution of Galaxies. *Astrophys. J.*, **600**(2), 681–694.
- Baldwin J. A., Phillips M. M., and Terlevich R. (1981). Classification parameters for the emission-line spectra of extragalactic objects. *PASP*, **93**, 5–19.
- Baugh C. M., Cole S., and Frenk C. S. (1996). Evolution of the Hubble sequence in hierarchical models for galaxy formation. *Mon. Notic. Roy. Astron. Soc.*, **283**(4), 1361–1378.
- Best P. N. and Heckman T. M. (2012). On the fundamental dichotomy in the local radio-AGN population: accretion, evolution and host galaxy properties. *Mon. Notic. Roy. Astron. Soc.*, **421**(2), 1569–1582.
- Bianchi S., Piconcelli E., Chiaberge M., et al. (2009). How Complex is the Obscuration in Active Galactic Nuclei? New Clues from the Suzaku Monitoring of the X-Ray Absorbers in NGC 7582. *Astrophys. J.*, **695**(1), 781–787.
- Birchall K. L., Watson M. G., and Aird J. (2020). X-ray detected AGN in SDSS dwarf galaxies. *Mon. Notic. Roy. Astron. Soc.*, **492**(2), 2268–2284.
- Blandford R., Meier D., and Readhead A. (2019). Relativistic Jets from Active Galactic Nuclei. *Annual Rev. Astron. & Astrophys.*, **57**, 467–509.
- Blanton M. R. and Moustakas J. (2009). Physical Properties and Environments of Nearby Galaxies. *Annual Rev. Astron. & Astrophys.*, **47**(1), 159–210.
- Bluck A. F. L., Maiolino R., Piotrowska J. M., et al. (2020). How do central and satellite galaxies quench? - Insights from spatially resolved spectroscopy in the MaNGA survey. *Mon. Notic. Roy. Astron. Soc.*, **499**(1), 230–268.
- Bongiorno A., Zamorani G., Gavignaud I., et al. (2007). The VVDS type-1 AGN sample: the faint end of the luminosity function. *Astron. & Astrophys.*, **472**(2), 443–454.

- Bongiorno A., Merloni A., Brusa M., et al. (2012). Accreting supermassive black holes in the COSMOS field and the connection to their host galaxies. *Mon. Notic. Roy. Astron. Soc.*, **427**(4), 3103–3133.
- Bongiorno A., Schulze A., Merloni A., et al. (2016). AGN host galaxy mass function in COSMOS. Is AGN feedback responsible for the mass-quenching of galaxies? *Astron. & Astrophys.*, **588**, A78.
- Boroson B., Kim D.-W., and Fabbiano G. (2011). Revisiting with Chandra the Scaling Relations of the X-ray Emission Components (Binaries, Nuclei, and Hot Gas) of Early-type Galaxies. *Astrophys. J.*, **729**(1), 12.
- Boyle B. J. and Terlevich R. J. (1998). The cosmological evolution of the QSO luminosity density and of the star formation rate. *Mon. Notic. Roy. Astron. Soc.*, **293**(2), L49–L51.
- Brandt W. and Hasinger G. (2005). Deep Extragalactic X-Ray Surveys. *Annual Review of Astronomy and Astrophysics*, **43**(1), 827–859.
- Bregman M. and Alexander T. (2009). Accretion Disk Warping by Resonant Relaxation: The Case of Maser Disk NGC 4258. *Astrophys. J.*, **700**(2), L192–L195.
- Brinchmann J., Charlot S., White S. D. M., et al. (2004). The physical properties of star-forming galaxies in the low-redshift Universe. *Mon. Notic. Roy. Astron. Soc.*, **351**(4), 1151–1179.
- Cameron E. and Driver S. P. (2009). Galaxy evolution by color-log(n) type since redshift unity in the Hubble Ultra Deep Field. *Astron. & Astrophys.*, **493**(2), 489–500.
- Capetti A., Axon D. J., Macchetto F., Sparks W. B., and Boksenberg A. (1996). HST Imaging Polarimetry of the Seyfert 2 Galaxy NGC 5728. *Astrophys. J.*, **466**, 169.

- Carrera F. J., Ebrero J., Mateos S., et al. (2007). The XMM-Newton serendipitous survey. III. The AXIS X-ray source counts and angular clustering. *Astron. & Astrophys.*, **469**(1), 27–46.
- Cattaneo A., Dekel A., Devriendt J., Guiderdoni B., and Blaizot J. (2006). Modelling the galaxy bimodality: shutdown above a critical halo mass. *Mon. Notic. Roy. Astron. Soc.*, **370**(4), 1651–1665.
- Cattaneo A., Faber S. M., Binney J., et al. (2009). The role of black holes in galaxy formation and evolution. *Nature*, **460**(7252), 213–219.
- Chabrier G. (2003). Galactic Stellar and Substellar Initial Mass Function. *PASP*, **115**(809), 763–795.
- Charlot S., Kauffmann G., Longhetti M., et al. (2002). Star formation, metallicity and dust properties derived from the Stromlo-APM galaxy survey spectra. *Mon. Notic. Roy. Astron. Soc.*, **330**(4), 876–888.
- Chen C.-T. J., Hickox R. C., Alberts S., et al. (2013). A Correlation between Star Formation Rate and Average Black Hole Accretion in Star-forming Galaxies. *Astrophys. J.*, **773**(1), 3.
- Churazov E., Sazonov S., Sunyaev R., et al. (2005). Supermassive black holes in elliptical galaxies: switching from very bright to very dim. *Mon. Notic. Roy. Astron. Soc.*, **363**(1), L91–L95.
- Cid Fernandes R., Stasińska G., Mateus A., and Vale Asari N. (2011). A comprehensive classification of galaxies in the Sloan Digital Sky Survey: how to tell true from fake AGN? *Mon. Notic. Roy. Astron. Soc.*, **413**(3), 1687–1699.
- Civano F., Fabbiano G., Pellegrini S., et al. (2014). Early-type Galaxies in the Chandra COSMOS Survey. *Astrophys. J.*, **790**(1), 16.
- Combes F. (2017). AGN feedback and its quenching efficiency. *Frontiers in Astronomy and Space Sciences*, **4**, 10.

- Couto G. S., Storch-Bergmann T., Robinson A., et al. (2016). Integral field spectroscopy of the circum-nuclear region of the radio Galaxy Pictor A. *Mon. Notic. Roy. Astron. Soc.*, **458**(1), 855–867.
- Cowie L. L., Songaila A., Hu E. M., and Cohen J. G. (1996). New Insight on Galaxy Formation and Evolution From Keck Spectroscopy of the Hawaii Deep Fields. *Astron. J.*, **112**, 839.
- Cox T. J., Dutta S. N., Di Matteo T., et al. (2006). The Kinematic Structure of Merger Remnants. *Astrophys. J.*, **650**(2), 791–811.
- Crocker A. F., Bureau M., Young L. M., and Combes F. (2011). Molecular gas and star formation in early-type galaxies. *Mon. Notic. Roy. Astron. Soc.*, **410**(2), 1197–1222.
- Croton D. J., Springel V., White S. D. M., et al. (2006). The many lives of active galactic nuclei: cooling flows, black holes and the luminosities and colours of galaxies. *Mon. Notic. Roy. Astron. Soc.*, **365**(1), 11–28.
- Czerny B. (2019). Slim Accretion Disks: Theory and Observational Consequences. *Universe*, **5**(5), 131.
- David L. P., Lim J., Forman W., et al. (2014). Molecular Gas in the X-Ray Bright Group NGC 5044 as Revealed by ALMA. *Astrophys. J.*, **792**(2), 94.
- Davies R. I., Müller Sánchez F., Genzel R., et al. (2007). A Close Look at Star Formation around Active Galactic Nuclei. *Astrophys. J.*, **671**(2), 1388–1412.
- Davis T. A., Alatalo K., Sarzi M., et al. (2011). The ATLAS^{3D} project - X. On the origin of the molecular and ionized gas in early-type galaxies. *Mon. Notic. Roy. Astron. Soc.*, **417**(2), 882–899.
- Dekel A., Sari R., and Ceverino D. (2009). Formation of Massive Galaxies at High Redshift: Cold Streams, Clumpy Disks, and Compact Spheroids. *Astrophys. J.*, **703**(1), 785–801.

- Delvecchio I., Gruppioni C., Pozzi F., et al. (2014). Tracing the cosmic growth of supermassive black holes to $z \sim 3$ with Herschel. *Mon. Notic. Roy. Astron. Soc.*, **439**(3), 2736–2754.
- Delvecchio I., Lutz D., Berta S., et al. (2015). Mapping the average AGN accretion rate in the SFR- M_* plane for Herschel-selected galaxies at $0 < z \leq 2.5$. *Mon. Notic. Roy. Astron. Soc.*, **449**(1), 373–389.
- Dickinson M., Papovich C., Ferguson H. C., and Budavári T. (2003). The Evolution of the Global Stellar Mass Density at $0 < z < 3$. *Astrophys. J.*, **587**(1), 25–40.
- Diniz S. I. F., Pastoriza M. G., Hernandez-Jimenez J. A., et al. (2017). Integral field spectroscopy of the inner kpc of the elliptical galaxy NGC 5044. *Mon. Notic. Roy. Astron. Soc.*, **470**(2), 1703–1717.
- Dressler A. (1980). Galaxy morphology in rich clusters: implications for the formation and evolution of galaxies. *Astrophys. J.*, **236**, 351–365.
- Dumas G., Mundell C. G., Emsellem E., and Nagar N. M. (2007). Central kiloparsec of Seyfert and inactive host galaxies: a comparison of two-dimensional stellar and gaseous kinematics. *Mon. Notic. Roy. Astron. Soc.*, **379**(4), 1249–1278.
- Durré M. and Mould J. (2018). The AGN Ionization Cones of NGC 5728. I. Excitation and Nuclear Structure. *Astrophys. J.*, **867**(2), 149.
- Durré M. and Mould J. (2019). The AGN Ionization Cones of NGC 5728. II. Kinematics. *Astrophys. J.*, **870**(1), 37.
- Elbaz D., Dickinson M., Hwang H. S., et al. (2011). GOODS-Herschel: an infrared main sequence for star-forming galaxies. *Astron. & Astrophys.*, **533**, A119.
- Elitzur M. and Shlosman I. (2006). The AGN-obscuring Torus: The End of the “Doughnut” Paradigm? *Astrophys. J.*, **648**(2), L101–L104.

- Elvis M., Wilkes B. J., McDowell J. C., et al. (1994). Atlas of Quasar Energy Distributions. *Astrophys. J. Suppl. Ser.*, **95**, 1.
- Evans I. N., Primini F. A., Glotfelty K. J., et al. (2010). The Chandra Source Catalog. *Astrophys. J. Suppl. Ser.*, **189**(1), 37–82.
- Fabbiano G. (2006). Populations of X-Ray Sources in Galaxies. *Annual Rev. Astron. & Astrophys.*, **44**(1), 323–366.
- Faber S. M., Willmer C. N. A., Wolf C., et al. (2007). Galaxy Luminosity Functions to $z \sim 1$ from DEEP2 and COMBO-17: Implications for Red Galaxy Formation. *Astrophys. J.*, **665**(1), 265–294.
- Fabian A. C. (2012). Observational Evidence of Active Galactic Nuclei Feedback. *Annual Rev. Astron. & Astrophys.*, **50**, 455–489.
- Falcke H., Körding E., and Markoff S. (2004). A scheme to unify low-power accreting black holes. Jet-dominated accretion flows and the radio/X-ray correlation. *Astron. & Astrophys.*, **414**, 895–903.
- Fan L., Han Y., Fang G., et al. (2016). The Most Luminous Heavily Obscured Quasars Have a High Merger Fraction: Morphological Study of WISE-selected Hot Dust-obscured Galaxies. *Astrophys. J.*, **822**(2), L32.
- Fanaroff B. L. and Riley J. M. (1974). The morphology of extragalactic radio sources of high and low luminosity. *Mon. Notic. Roy. Astron. Soc.*, **167**, 31P–36P.
- Fathi K., Storchi-Bergmann T., Riffel R. A., et al. (2006). Streaming Motions toward the Supermassive Black Hole in NGC 1097. *Astrophys. J.*, **641**(1), L25–L28.
- Ferrarese L. and Merritt D. (2000). A Fundamental Relation between Supermassive Black Holes and Their Host Galaxies. *Astrophys. J.*, **539**(1), L9–L12.

- Fischer T. C., Crenshaw D. M., Kraemer S. B., et al. (2015). A Minor Merger Caught in the Act of Fueling the Active Galactic Nucleus in Mrk 509. *Astrophys. J.*, **799**(2), 234.
- Fragos T., Lehmer B., Tremmel M., et al. (2013). X-Ray Binary Evolution Across Cosmic Time. *Astrophys. J.*, **764**(1), 41.
- Frederick S., Gezari S., Graham M. J., et al. (2019). A New Class of Changing-look LINERs. *Astrophys. J.*, **883**(1), 31.
- García-Burillo S., Combes F., Ramos Almeida C., et al. (2016). ALMA Resolves the Torus of NGC 1068: Continuum and Molecular Line Emission. *Astrophys. J.*, **823**(1), L12.
- Gaspari M., Ruszkowski M., and Oh S. P. (2013). Chaotic cold accretion on to black holes. *Mon. Notic. Roy. Astron. Soc.*, **432**(4), 3401–3422.
- Gaspari M., Brighenti F., and Temi P. (2015). Chaotic cold accretion on to black holes in rotating atmospheres. *Astron. & Astrophys.*, **579**, A62.
- Gaspari M., McDonald M., Hamer S. L., et al. (2018). Shaken Snow Globes: Kinematic Tracers of the Multiphase Condensation Cascade in Massive Galaxies, Groups, and Clusters. *Astrophys. J.*, **854**(2), 167.
- Gebhardt K., Bender R., Bower G., et al. (2000). A Relationship between Nuclear Black Hole Mass and Galaxy Velocity Dispersion. *Astrophys. J.*, **539**(1), L13–L16.
- Genzel R., Burkert A., Bouché N., et al. (2008). From Rings to Bulges: Evidence for Rapid Secular Galaxy Evolution at $z \sim 2$ from Integral Field Spectroscopy in the SINS Survey. *Astrophys. J.*, **687**(1), 59–77.
- Georgakakis A., Pérez-González P. G., Fanidakis N., et al. (2014). Investigating evidence for different black hole accretion modes since redshift $z \sim 1$. *Mon. Notic. Roy. Astron. Soc.*, **440**(1), 339–352.

- Glikman E., Simmons B., Mailly M., et al. (2015). Major Mergers Host the Most-luminous Red Quasars at $z \sim 2$: A Hubble Space Telescope WFC3/IR Study. *Astrophys. J.*, **806**(2), 218.
- Goulding A. D., Forman W. R., Hickox R. C., et al. (2014). Tracing the Evolution of Active Galactic Nuclei Host Galaxies over the Last 9 Gyr of Cosmic Time. *Astrophys. J.*, **783**(1), 40.
- Gültekin K., Richstone D. O., Gebhardt K., et al. (2009). The M - σ and M - L Relations in Galactic Bulges, and Determinations of Their Intrinsic Scatter. *Astrophys. J.*, **698**(1), 198–221.
- Hardcastle M. J., Evans D. A., and Croston J. H. (2007). Hot and cold gas accretion and feedback in radio-loud active galaxies. *Mon. Notic. Roy. Astron. Soc.*, **376**(4), 1849–1856.
- Häring N. and Rix H.-W. (2004). On the Black Hole Mass-Bulge Mass Relation. *Astrophys. J.*, **604**(2), L89–L92.
- Hasinger G., Miyaji T., and Schmidt M. (2005). Luminosity-dependent evolution of soft X-ray selected AGN. New Chandra and XMM-Newton surveys. *Astron. & Astrophys.*, **441**(2), 417–434.
- Heckman T. M. and Best P. N. (2014). The Coevolution of Galaxies and Supermassive Black Holes: Insights from Surveys of the Contemporary Universe. *Annual Rev. Astron. & Astrophys.*, **52**, 589–660.
- Heinis S., Gezari S., Kumar S., et al. (2016). The Host Galaxy Properties of Variability Selected AGN in the Pan-STARRS1 Medium Deep Survey. *Astrophys. J.*, **826**(1), 62.
- Hickox R. C., Jones C., Forman W. R., et al. (2009). Host Galaxies, Clustering, Eddington Ratios, and Evolution of Radio, X-Ray, and Infrared-Selected AGNs. *Astrophys. J.*, **696**(1), 891–919.

- Hickox R. C., Mullaney J. R., Alexander D. M., et al. (2014). Black Hole Variability and the Star Formation-Active Galactic Nucleus Connection: Do All Star-forming Galaxies Host an Active Galactic Nucleus? *Astrophys. J.*, **782**(1), 9.
- Hirschmann M., Dolag K., Saro A., et al. (2014). Cosmological simulations of black hole growth: AGN luminosities and downsizing. *Mon. Notic. Roy. Astron. Soc.*, **442**(3), 2304–2324.
- Ho L. C. (2008). Nuclear activity in nearby galaxies. *Annual Rev. Astron. & Astrophys.*, **46**, 475–539.
- Hobbs A., Nayakshin S., Power C., and King A. (2011). Feeding supermassive black holes through supersonic turbulence and ballistic accretion. *Mon. Notic. Roy. Astron. Soc.*, **413**(4), 2633–2650.
- Hönig S. F. (2019). Redefining the Torus: A Unifying View of AGNs in the Infrared and Submillimeter. *Astrophys. J.*, **884**(2), 171.
- Hopkins P. F., Hernquist L., Cox T. J., and Kereš D. (2008). A Cosmological Framework for the Co-Evolution of Quasars, Supermassive Black Holes, and Elliptical Galaxies. I. Galaxy Mergers and Quasar Activity. *Astrophys. J. Suppl. Ser.*, **175**(2), 356–389.
- Hopkins P. F. and Quataert E. (2010). How do massive black holes get their gas? *Mon. Notic. Roy. Astron. Soc.*, **407**(3), 1529–1564.
- Hopkins P. F. (2012). Dynamical delays between starburst and AGN activity in galaxy nuclei. *Mon. Notic. Roy. Astron. Soc.*, **420**(1), L8–L12.
- Hopkins P. F., Torrey P., Faucher-Giguère C.-A., Quataert E., and Murray N. (2016). Stellar and quasar feedback in concert: effects on AGN accretion, obscuration, and outflows. *Mon. Notic. Roy. Astron. Soc.*, **458**(1), 816–831.
- Hubble E. P. (1926). Extragalactic nebulae. *Astrophys. J.*, **64**, 321–369.

- Impellizzeri C. M. V., Gallimore J. F., Baum S. A., et al. (2019). Counter-rotation and High-velocity Outflow in the Parsec-scale Molecular Torus of NGC 1068. *Astrophys. J.*, **884**(2), L28.
- Ishibashi W. and Fabian A. C. (2012). Active galactic nucleus feedback and triggering of star formation in galaxies. *Mon. Notic. Roy. Astron. Soc.*, **427**(4), 2998–3005.
- Jansen F., Lumb D., Altieri B., et al. (2001). XMM-Newton observatory. I. The spacecraft and operations. *Astron. & Astrophys.*, **365**, L1–L6.
- Kauffmann G. and Haehnelt M. (2000). A unified model for the evolution of galaxies and quasars. *Mon. Notic. Roy. Astron. Soc.*, **311**(3), 576–588.
- Kauffmann G., Heckman T. M., White S. D. M., et al. (2003). Stellar masses and star formation histories for 10^5 galaxies from the Sloan Digital Sky Survey. *Mon. Notic. Roy. Astron. Soc.*, **341**(1), 33–53.
- Kauffmann G., Heckman T. M., Tremonti C., et al. (2003). The host galaxies of active galactic nuclei. *Mon. Notic. Roy. Astron. Soc.*, **346**(4), 1055–1077.
- Kauffmann G. and Heckman T. M. (2009). Feast and Famine: regulation of black hole growth in low-redshift galaxies. *Mon. Notic. Roy. Astron. Soc.*, **397**(1), 135–147.
- Kewley L. J., Groves B., Kauffmann G., and Heckman T. (2006). The host galaxies and classification of active galactic nuclei. *Mon. Notic. Roy. Astron. Soc.*, **372**(3), 961–976.
- Kim D.-W. and Fabbiano G. (2013). X-Ray Scaling Relation in Early-type Galaxies: Dark Matter as a Primary Factor in Retaining Hot Gas. *Astrophys. J.*, **776**(2), 116.

- Kormendy J. and Bender R. (2012). A Revised Parallel-sequence Morphological Classification of Galaxies: Structure and Formation of S0 and Spheroidal Galaxies. *Astrophys. J. Suppl. Ser.*, **198**(1), 2.
- Kormendy J. and Ho L. C. (2013). Coevolution (Or Not) of Supermassive Black Holes and Host Galaxies. *Annual Rev. Astron. & Astrophys.*, **51**(1), 511–653.
- Kroupa P. (2001). On the variation of the initial mass function. *Mon. Notic. Roy. Astron. Soc.*, **322**(2), 231–246.
- Larson R. B. (1975). Models for the formation of elliptical galaxies. *Mon. Notic. Roy. Astron. Soc.*, **173**, 671–699.
- Lehmer B. D., Basu-Zych A. R., Mineo S., et al. (2016). The Evolution of Normal Galaxy X-Ray Emission through Cosmic History: Constraints from the 6 MS Chandra Deep Field-South. *Astrophys. J.*, **825**(1), 7.
- Liu T., Tozzi P., Wang J.-X., et al. (2017). X-Ray Spectral Analyses of AGNs from the 7Ms Chandra Deep Field-South Survey: The Distribution, Variability, and Evolutions of AGN Obscuration. *Astrophys. J. Suppl. Ser.*, **232**(1), 8.
- Luo B., Brandt W. N., Xue Y. Q., et al. (2017). The Chandra Deep Field-South Survey: 7 Ms Source Catalogs. *Astrophys. J. Suppl. Ser.*, **228**(1), 2.
- Lusso E., Comastri A., Simmons B. D., et al. (2012). Bolometric luminosities and Eddington ratios of X-ray selected active galactic nuclei in the XMM-COSMOS survey. *Mon. Notic. Roy. Astron. Soc.*, **425**(1), 623–640.
- Lutz D., Mainieri V., Rafferty D., et al. (2010). The LABOCA Survey of the Extended Chandra Deep Field South: Two Modes of Star Formation in Active Galactic Nucleus Hosts? *Astrophys. J.*, **712**(2), 1287–1301.
- Maccacaro T., Gioia I. M., Wolter A., Zamorani G., and Stocke J. T. (1988). The X-Ray Spectra of the Extragalactic Sources in the Einstein Extended Medium-Sensitivity Survey. *Astrophys. J.*, **326**, 680.

- Madau P. and Dickinson M. (2014). Cosmic Star-Formation History. *Annual Rev. Astron. & Astrophys.*, **52**, 415–486.
- Mainieri V., Bergeron J., Hasinger G., et al. (2002). XMM-Newton observation of the Lockman Hole. II. Spectral analysis. *Astron. & Astrophys.*, **393**, 425–438.
- Marchesini D., van Dokkum P. G., Förster Schreiber N. M., et al. (2009). The Evolution of the Stellar Mass Function of Galaxies from $z = 4.0$ and the First Comprehensive Analysis of its Uncertainties: Evidence for Mass-Dependent Evolution. *Astrophys. J.*, **701**(2), 1765–1796.
- Marconi A. and Hunt L. K. (2003). The Relation between Black Hole Mass, Bulge Mass, and Near-Infrared Luminosity. *Astrophys. J.*, **589**(1), L21–L24.
- Marconi A., Risaliti G., Gilli R., et al. (2004). Local supermassive black holes, relics of active galactic nuclei and the X-ray background. *Mon. Notic. Roy. Astron. Soc.*, **351**(1), 169–185.
- Marin F. and Schartmann M. (2017). Polarized radiative transfer modeling of warped and clumpy dusty tori. *Astron. & Astrophys.*, **607**, A37.
- Masoura V. A., Mountrichas G., Georgantopoulos I., et al. (2018). Disentangling the AGN and star formation connection using XMM-Newton. *Astron. & Astrophys.*, **618**, A31.
- McConnell N. J. and Ma C.-P. (2013). Revisiting the Scaling Relations of Black Hole Masses and Host Galaxy Properties. *Astrophys. J.*, **764**(2), 184.
- Menci N., Fontana A., Giallongo E., and Salimbeni S. (2005). Bimodal Color Distribution in Hierarchical Galaxy Formation. *Astrophys. J.*, **632**(1), 49–57.
- Menci N., Fontana A., Giallongo E., Grazian A., and Salimbeni S. (2006). The Abundance of Distant and Extremely Red Galaxies: The Role of AGN Feedback in Hierarchical Models. *Astrophys. J.*, **647**(2), 753–762.

- Mendel J. T., Simard L., Palmer M., Ellison S. L., and Patton D. R. (2014). A Catalog of Bulge, Disk, and Total Stellar Mass Estimates for the Sloan Digital Sky Survey. *Astrophys. J. Suppl. Ser.*, **210**(1), 3.
- Mendez A. J., Coil A. L., Aird J., et al. (2013). PRIMUS: Infrared and X-Ray AGN Selection Techniques at $0.2 \lesssim z \lesssim 1.2$. *Astrophys. J.*, **770**(1), 40.
- Merloni A., Bongiorno A., Bolzonella M., et al. (2010). On the Cosmic Evolution of the Scaling Relations Between Black Holes and Their Host Galaxies: Broad-Line Active Galactic Nuclei in the zCOSMOS Survey. *Astrophys. J.*, **708**(1), 137–157.
- Morganti R., Fogasy J., Paragi Z., Oosterloo T., and Orienti M. (2013). Radio Jets Clearing the Way Through a Galaxy: Watching Feedback in Action. *Science*, **341**(6150), 1082–1085.
- Mullaney J. R., Pannella M., Daddi E., et al. (2012). GOODS-Herschel: the far-infrared view of star formation in active galactic nucleus host galaxies since $z \approx 3$. *Mon. Notic. Roy. Astron. Soc.*, **419**(1), 95–115.
- Mullaney J. R., Daddi E., Béthermin M., et al. (2012). The Hidden “AGN Main Sequence”: Evidence for a Universal Black Hole Accretion to Star Formation Rate Ratio since $z \sim 2$ Producing an $M_{BH}-M_*$ Relation. *Astrophys. J.*, **753**(2), L30.
- Murray N. and Chiang J. (1997). Disk Winds and Disk Emission Lines. *Astrophys. J.*, **474**(1), 91–103.
- Naab T., Khochfar S., and Burkert A. (2006). Properties of Early-Type, Dry Galaxy Mergers and the Origin of Massive Elliptical Galaxies. *Astrophys. J.*, **636**(2), L81–L84.
- Nandra K., Georgakakis A., Willmer C. N. A., et al. (2007). AEGIS: The Color-Magnitude Relation for X-Ray-selected Active Galactic Nuclei. *Astrophys. J.*, **660**(1), L11–L14.

- Narayan R., Garcia M. R., and McClintock J. E. (1997). Advection-dominated Accretion and Black Hole Event Horizons. *Astrophys. J.*, **478**(2), L79–L82.
- Neistein E. and Netzer H. (2014). What triggers black hole growth? Insights from star formation rates. *Mon. Notic. Roy. Astron. Soc.*, **437**(4), 3373–3384.
- Netzer H. (2015). Revisiting the Unified Model of Active Galactic Nuclei. *Annual Rev. Astron. & Astrophys.*, **53**, 365–408.
- Nicastro F. (2000). Broad Emission Line Regions in Active Galactic Nuclei: The Link with the Accretion Power. *Astrophys. J.*, **530**(2), L65–L68.
- Noeske K. G., Weiner B. J., Faber S. M., et al. (2007). Star Formation in AEGIS Field Galaxies since $z=1.1$: The Dominance of Gradually Declining Star Formation, and the Main Sequence of Star-forming Galaxies. *Astrophys. J.*, **660**(1), L43–L46.
- Oemler, Augustus J., Abramson L. E., Gladders M. D., et al. (2017). The Star Formation Histories of Disk Galaxies: The Live, the Dead, and the Undead. *Astrophys. J.*, **844**(1), 45.
- Padovani P., Alexander D. M., Assef R. J., et al. (2017). Active galactic nuclei: what’s in a name? *A&A Rev.*, **25**(1), 2.
- Paolillo M., Papadakis I., Brandt W. N., et al. (2017). Tracing the accretion history of supermassive black holes through X-ray variability: results from the ChandraDeep Field-South. *Mon. Notic. Roy. Astron. Soc.*, **471**(4), 4398–4411.
- Peebles P. J. E. (1965). The Black-Body Radiation Content of the Universe and the Formation of Galaxies. *Astrophys. J.*, **142**, 1317.
- Popesso P., Concas A., Morselli L., et al. (2019). The main sequence of star-forming galaxies - I. The local relation and its bending. *Mon. Notic. Roy. Astron. Soc.*, **483**(3), 3213–3226.

- Quataert E. (2003). Radiatively Inefficient Accretion Flow Models of Sgr A*. *Astronomische Nachrichten Supplement*, **324**(1), 435–443.
- Ranalli P., Comastri A., and Setti G. (2003). The 2-10 keV luminosity as a Star Formation Rate indicator. *Astron. & Astrophys.*, **399**, 39–50.
- Reines A. E. and Volonteri M. (2015). Relations between Central Black Hole Mass and Total Galaxy Stellar Mass in the Local Universe. *Astrophys. J.*, **813**(2), 82.
- Richards G. T., Lacy M., Storrie-Lombardi L. J., et al. (2006). Spectral Energy Distributions and Multiwavelength Selection of Type 1 Quasars. *Astrophys. J. Suppl. Ser.*, **166**(2), 470–497.
- Risaliti G., Elvis M., Fabbiano G., Baldi A., and Zezas A. (2005). Rapid Compton-thick/Compton-thin Transitions in the Seyfert 2 Galaxy NGC 1365. *Astrophys. J.*, **623**(2), L93–L96.
- Robertson B., Bullock J. S., Cox T. J., et al. (2006). A Merger-driven Scenario for Cosmological Disk Galaxy Formation. *Astrophys. J.*, **645**(2), 986–1000.
- Rodighiero G., Brusa M., Daddi E., et al. (2015). Relationship between Star Formation Rate and Black Hole Accretion At $Z = 2$: the Different Contributions in Quiescent, Normal, and Starburst Galaxies. *Astrophys. J.*, **800**(1), L10.
- Romero-Gómez M., Athanassoula E., Masdemont J. J., and García-Gómez C. (2007). The formation of spiral arms and rings in barred galaxies. *Astron. & Astrophys.*, **472**(1), 63–75.
- Rosario D. J., Santini P., Lutz D., et al. (2013). Nuclear Activity is More Prevalent in Star-forming Galaxies. *Astrophys. J.*, **771**(1), 63.
- Rosen S. R., Webb N. A., Watson M. G., et al. (2016). The XMM-Newton serendipitous survey. VII. The third XMM-Newton serendipitous source catalogue. *Astron. & Astrophys.*, **590**, A1.

- Rovilos E., Comastri A., Gilli R., et al. (2012). GOODS-Herschel: ultra-deep XMM-Newton observations reveal AGN/star-formation connection. *Astron. & Astrophys.*, **546**, A58.
- Russell H. R., McNamara B. R., Fabian A. C., et al. (2016). ALMA observations of cold molecular gas filaments trailing rising radio bubbles in PKS 0745-191. *Mon. Notic. Roy. Astron. Soc.*, **458**(3), 3134–3149.
- Salim S., Rich R. M., Charlot S., et al. (2007). UV Star Formation Rates in the Local Universe. *Astrophys. J. Suppl. Ser.*, **173**(2), 267–292.
- Salim S., Lee J. C., Janowiecki S., et al. (2016). GALEX-SDSS-WISE Legacy Catalog (GSWLC): Star Formation Rates, Stellar Masses, and Dust Attenuations of 700,000 Low-redshift Galaxies. *Astrophys. J. Suppl. Ser.*, **227**(1), 2.
- Sanders R. H. and Huntley J. M. (1976). Gas response to oval distortions in disk galaxies. *Astrophys. J.*, **209**, 53–65.
- Savorgnan G. A. D., Graham A. W., Marconi A., and Sani E. (2016). Supermassive Black Holes and Their Host Spheroids. II. The Red and Blue Sequence in the M_{BH} - $M_{*,sph}$ Diagram. *Astrophys. J.*, **817**(1), 21.
- Schartmann M., Meisenheimer K., Klahr H., et al. (2009). The effect of stellar feedback on the formation and evolution of gas and dust tori in AGN. *Mon. Notic. Roy. Astron. Soc.*, **393**(3), 759–773.
- Schawinski K., Lintott C. J., Thomas D., et al. (2009). Destruction of Molecular Gas Reservoirs in Early-Type Galaxies by Active Galactic Nucleus Feedback. *Astrophys. J.*, **690**(2), 1672–1680.
- Serra P., Oosterloo T., Morganti R., et al. (2012). The ATLAS^{3D} project - XIII. Mass and morphology of H I in early-type galaxies as a function of environment. *Mon. Notic. Roy. Astron. Soc.*, **422**(3), 1835–1862.

- Shakura N. I. and Sunyaev R. A. (1973). Black holes in binary systems. Observational appearance. *Astron. & Astrophys.*, **24**, 337–355.
- Shankar F., Bernardi M., Sheth R. K., et al. (2016). Selection bias in dynamically measured supermassive black hole samples: its consequences and the quest for the most fundamental relation. *Mon. Notic. Roy. Astron. Soc.*, **460**(3), 3119–3142.
- Shankar F., Bernardi M., and Sheth R. K. (2017). Selection bias in dynamically measured supermassive black hole samples: dynamical masses and dependence on Sérsic index. *Mon. Notic. Roy. Astron. Soc.*, **466**(4), 4029–4039.
- Shankar F., Allevato V., Bernardi M., et al. (2020). Constraining black hole-galaxy scaling relations and radiative efficiency from galaxy clustering. *Nature Astronomy*, **4**, 282–291.
- Shen Y., Richards G. T., Strauss M. A., et al. (2011). A Catalog of Quasar Properties from Sloan Digital Sky Survey Data Release 7. *Astrophys. J. Suppl. Ser.*, **194**(2), 45.
- Shimizu T. T., Mushotzky R. F., Meléndez M., Koss M., and Rosario D. J. (2015). Decreased specific star formation rates in AGN host galaxies. *Mon. Notic. Roy. Astron. Soc.*, **452**(2), 1841–1860.
- Skrutskie M. F., Cutri R. M., Stiening R., et al. (2006). The Two Micron All Sky Survey (2MASS). *Astron. J.*, **131**(2), 1163–1183.
- Stemo A., Comerford J. M., Barrows R. S., et al. (2020). A Catalog of AGN Host Galaxies Observed with HST/ACS: Correlations between Star Formation and AGN Activity. *Astrophys. J.*, **888**(2), 78.
- Stoklasová I., Ferruit P., Emsellem E., et al. (2009). OASIS integral-field spectroscopy of the central kpc in 11 Seyfert 2 galaxies. *Astron. & Astrophys.*, **500**(3), 1287–1325.

- Storchi-Bergmann T., Dors, Oli L. J., Riffel R. A., et al. (2007). Nuclear Spirals as Feeding Channels to the Supermassive Black Hole: The Case of the Galaxy NGC 6951. *Astrophys. J.*, **670**(2), 959–967.
- Storchi-Bergmann T. and Schnorr-Müller A. (2019). Observational constraints on the feeding of supermassive black holes. *Nature Astronomy*, **3**, 48–61.
- Strateva I., Ivezić Ž., Knapp G. R., et al. (2001). Color Separation of Galaxy Types in the Sloan Digital Sky Survey Imaging Data. *Astron. J.*, **122**(4), 1861–1874.
- Symeonidis M., Georgakakis A., Page M. J., et al. (2014). Linking the X-ray and infrared properties of star-forming galaxies at $z < 1.5$. *Mon. Notic. Roy. Astron. Soc.*, **443**(4), 3728–3740.
- Tadhunter C. (2008). An introduction to active galactic nuclei: Classification and unification. *New Astron. Rev.*, **52**(6), 227–239.
- Thom C., Tumlinson J., Werk J. K., et al. (2012). Not Dead Yet: Cool Circumgalactic Gas in the Halos of Early-type Galaxies. *Astrophys. J.*, **758**(2), L41.
- Thomas D., Maraston C., Schawinski K., Sarzi M., and Silk J. (2010). Environment and self-regulation in galaxy formation. *Mon. Notic. Roy. Astron. Soc.*, **404**(4), 1775–1789.
- Tozzi P., Gilli R., Mainieri V., et al. (2006). X-ray spectral properties of active galactic nuclei in the Chandra Deep Field South. *Astron. & Astrophys.*, **451**(2), 457–474.
- Tran H. D. (2003). The Unified Model and Evolution of Active Galaxies: Implications from a Spectropolarimetric Study. *Astrophys. J.*, **583**(2), 632–648.
- Treister E., Schawinski K., Urry C. M., and Simmons B. D. (2012). Major Galaxy Mergers Only Trigger the Most Luminous Active Galactic Nuclei. *Astrophys. J.*, **758**(2), L39.

- Tremblay G. R., Oonk J. B. R., Combes F., et al. (2016). Cold, clumpy accretion onto an active supermassive black hole. *Nature*, **534**(7606), 218–221.
- Tremonti C. A., Heckman T. M., Kauffmann G., et al. (2004). The Origin of the Mass-Metallicity Relation: Insights from 53,000 Star-forming Galaxies in the Sloan Digital Sky Survey. *Astrophys. J.*, **613**(2), 898–913.
- Tristram K. R. W., Burtscher L., Jaffe W., et al. (2014). The dusty torus in the Circinus galaxy: a dense disk and the torus funnel. *Astron. & Astrophys.*, **563**, A82.
- Ueda Y., Akiyama M., Ohta K., and Miyaji T. (2003). Cosmological Evolution of the Hard X-Ray Active Galactic Nucleus Luminosity Function and the Origin of the Hard X-Ray Background. *Astrophys. J.*, **598**(2), 886–908.
- Ueda Y., Akiyama M., Hasinger G., Miyaji T., and Watson M. G. (2014). Toward the Standard Population Synthesis Model of the X-Ray Background: Evolution of X-Ray Luminosity and Absorption Functions of Active Galactic Nuclei Including Compton-thick Populations. *Astrophys. J.*, **786**(2), 104.
- Urry C. M. and Padovani P. (1995). Unified Schemes for Radio-Loud Active Galactic Nuclei. *PASP*, **107**, 803.
- Veilleux S. and Osterbrock D. E. (1987). Spectral Classification of Emission-Line Galaxies. *Astrophys. J. Suppl. Ser.*, **63**, 295.
- Vollmer B., Beckert T., and Davies R. I. (2008). Starbursts and torus evolution in AGN. *Astron. & Astrophys.*, **491**(2), 441–453.
- Webb N. A., Coriat M., Traulsen I., et al. (2020). The XMM-Newton serendipitous survey. IX. The fourth XMM-Newton serendipitous source catalogue. *Astron. & Astrophys.*, **641**, A136.
- Wild V., Heckman T., and Charlot S. (2010). Timing the starburst-AGN connection. *Mon. Notic. Roy. Astron. Soc.*, **405**(2), 933–947.

- Wilson A. S., Braatz J. A., Heckman T. M., Krolik J. H., and Miley G. K. (1993). The Ionization Cones in the Seyfert Galaxy NGC 5728. *Astrophys. J.*, **419**, L61.
- Xu Y. and Cao X.-W. (2007). Evidence of the Link between Broad Emission Line Regions and Accretion Disks in Active Galactic Nuclei. , **7**(1), 63–70.
- Xue Y. Q., Luo B., Brandt W. N., et al. (2011). The Chandra Deep Field-South Survey: 4 Ms Source Catalogs. *Astrophys. J. Suppl. Ser.*, **195**(1), 10.
- Yan R. and Blanton M. R. (2012). The Nature of LINER-like Emission in Red Galaxies. *Astrophys. J.*, **747**(1), 61.
- Yang G., Brandt W. N., Vito F., et al. (2018). Linking black hole growth with host galaxies: the accretion-stellar mass relation and its cosmic evolution. *Mon. Notic. Roy. Astron. Soc.*, **475**(2), 1887–1911.
- Young L. M., Bureau M., Davis T. A., et al. (2011). The ATLAS^{3D} project - IV. The molecular gas content of early-type galaxies. *Mon. Notic. Roy. Astron. Soc.*, **414**(2), 940–967.
- Yuan H. B., Liu X. W., and Xiang M. S. (2013). Empirical extinction coefficients for the GALEX, SDSS, 2MASS and WISE passbands. *Mon. Notic. Roy. Astron. Soc.*, **430**(3), 2188–2199.
- de Nicola S., Marconi A., and Longo G. (2019). The fundamental relation between supermassive black holes and their host galaxies. *Mon. Notic. Roy. Astron. Soc.*, **490**(1), 600–612.
- Frank J., King A., and Raine D. J. (2002). *Accretion Power in Astrophysics: Third Edition*. Cambridge University Press, Cambridge, UK.
- Beckmann V. and Shrader C. R. (2012). *Active Galactic Nuclei*. Wiley, Hoboken, USA.